City Research Online

City St George’s, University of London

Citation: Shamekhi Amiri, S. (2023). Transient analysis and optimisation of solar-powered micro gas turbine operation during start-up. (Unpublished Doctoral thesis, City, University of London)

Permanent repository link: https://openaccess.city.ac.uk/id/eprint/32238/

Transient analysis and optimisation of solar-powered micro gas turbine operation during start-up

Shahrbanoo Shamekhi Amiri

Submitted for the degree of Doctor of Philosophy
School of Science and Technology
City University of London.

Thesis
2023

I would like to dedicate this thesis to my loving husband, my loving parents and the brave women of Iran. . . .

Declaration

I hereby declare that this thesis has not been and will not be submitted in whole or in part to another University for the award of any other degree. I also grant powers of discretion to the University Librarian to allow the thesis to be copied in whole or in part without further reference to the author. This permission covers only single copies made for study purposes, subject to normal conditions of acknowledgement.
Signature:
Shahrbanoo Shamekhi Amiri.

Abstract

In recent years, there has been a growing interest in small-scale concentrated solar power (CSP) generation. Among the various thermal engines that can be combined with CSP dishes, Stirling engines have exhibited admirable levels of efficiency. However, they are hindered by their high costs and low reliability, mainly attributed to their technical complexity. Micro gas turbines (MGT) offer improved reliability and the potential for cost reduction. The combination of CSP dishes with MGTs (CSP-MGT systems) which exclusively depend on solar energy, results in multiple start-ups during operations due to intermittent thermal input power. Despite the criticality of this phase, there have been limited studies into the start-up in comparison to growing interest in the CSP-MGTs for small-scale applications. Therefore, this thesis focuses on designing an efficient and safe start-up schedule for CSP-MGTs.

A real-time transient model for CSP-MGT was developed and validated using existing experimental data. MGT components were modelled as lumped volumes or one-dimensional discretisation approach with solving conservation equations of mass, momentum, and energy along with components' characteristic maps. The electrical model was also developed to be combined with the thermo-mechanical model with a steady-state approach. The transient model effectively simulates the transient performance of a CSP-MGT during start-up by showing a good agreement with experimental measurements. After model validation was accomplished, a tailored start-up sequence for the CSP-MGT was introduced. Unlike conventional fuelled MGTs, CSP-MGTs necessitate a reference speed schedule for their control system during the start-up process. The speed schedule was designed and formulated by a number of parameters, each with an adopted range based on the system constraints. Furthermore, an innovative method was employed to classify the types of start-ups, based on the specific temperature value in the system at the initial moment, rather than the duration after the system's shutdown.

An optimisation framework for the start-up schedule of the CSP-MGT system has been developed. The objective was to find optimised start-up schedules for efficient and safe operation during this phase. It was revealed that the optimised solutions of the defined objectives showed a 60% reduction compared to the remaining potential solutions. The optimised speed schedules for the CSP-MGT system indicate that a minimum of three steps is necessary for the speed schedule. The determinative parameters of the optimal speed schedules with respect to the safety constraints of the system have been quantified.

The transient analysis of the CSP-MGT on an annual basis has also been done. Having developed a programme structure, the annual net produced energy throughout the year was found. The assessment showed that about 3.5% of the yearly produced energy is used for the motoring mode in the case of using optimal start-up schedules and 7% for the case of using the pre-existing speed schedule.

To conclude, this thesis presents detailed insights into the transient analysis of a CSP-MGT during the start-up phase. This has considered finding a tailored and optimal start-up schedule aimed at ensuring both safety and efficiency of a CSP-MGT along with an annual evaluation.

Acknowledgement

First, I would like to thank my supervisors, Professor Abdulnaser Sayma and Dr Jafar Al-Zaili whom I am very grateful for their support and invaluable advice throughout the progression of my research. Furthermore, I am deeply appreciative of the opportunity they provided me to pursue my PhD at the Thermo-Fluid Research Centre. Being a part of this centre allowed me to present my findings to fellow members and gain insights into ongoing research within the group. The collaborative environment fostered at the centre enriched my academic experience and significantly contributed to the success of my PhD endeavour.

Huge thanks go to my colleague and dear friend Dr Mohsen Ghavami who provided me with invaluable comments and pieces of knowledge. I would also like to acknowledge the wide experience and useful comments from Dr Mahmoud Khader. I am also thankful to my fellow PhD students and colleagues in the thermo-fluid research centre, especially Dr Hicham Chibli and Dr Salma Salah who provided me valuable comments on writing the thesis.

I would like to express my heartfelt gratitude to my colleagues, post-doctoral researchers, and fellow PhD students, namely Mohsen Ghavami, Hicham Chibli, Akanksha Dixit, Abdelrahman Abdeldayem, Omar Selim, Dr Omar Aqel, Ahmad Abuhaiba, Stephen Majebi, and Erika Rodriguez Aleman. Their unwavering support during challenging times and the engaging discussions and enjoyable moments we shared have been invaluable in reducing work stress. Their friendship and encouragement have created a positive and motivating atmosphere, making the journey towards completing my PhD much more fulfilling.

Finally, I would like to thank my dear husband, our wonderful and lovely parents for their patience, love and support throughout my work. Without the encouragement I received from them, doing this thesis would have not been a pleasant job.

Contents

List of Tables

List of Figures

Nomenclature

Greek Symbols

α	The power of an equation for finding fanning friction factor
β	Thermal expansion coefficient [1/K]
γ	Specific heat ratio
δ_w	Recuperator plate thickness
ε	Emissivity of the inner wall of the receiver's cavity
ζ	Damping ratio
η	Isentropic efficiency
μ_{oil}	Dynamic viscosity of the bearing oil [kg/m.s]
ν	Kinematic viscosity of air [m^2/s]
π	Pressure ratio
π_{op}	Pressure ratio of the operating point
π_s	Pressure ratio of an operating point on the surge line
ρ	Density [kg/m^3]
τ	Torque [N.m] and time constant [s]
τ_A	High speed alternator's torque [N.m]
ϕ	Tilt angle of the cavity receive [degree]
ϕ_{mg}	Flux linkage induced by the motor [Wb]
ω	Shaft speed [rad/s]

Roman Symbols

AR	Aperture size [m^2]
C_d	Discharge coefficient
c_p, C	Specific heat capacity [kJ/kg.K]
D	Pitch circle diameter of the shaft bearing [m]

D_h	Hydraulic diameter [m]
d	Nozzle diameter [m]
$E_{on,I}$	IGBT energy loss during switching on [J]
$E_{off,I}$	IGBT energy loss during switching off [J]
f	Fanning friction factor
G	Fluid mass velocity based on the minimum free area ($\dot{m}/A_0$) [m]
Gr	Grashof number
I_c	IGBT's collector electric current [Amps]
I_q	q-axis electric current [Amps]
I_d	d-axis electric current [Amps]
J	Rotational inertia of shaft [kg.m^2]
k	Thermal conductivity [W/m.K]
K_{HSA}	The multiplier for calculating iron losses of motor [V/krpm]
k_I	Integral coefficient of the controller
k_p	Proportional coefficient of the controller
L	The length of the equivalent volume of the one side of the recuperator [m]
L_q	q-axis inductance [H]
L_d	d-axis inductance [H]
L_s	Characteristic length of the cavity receiver [m]
$\dot{m}$	Mass flow rate [kg/s]
N	Shaft speed [rpm]
n	Nozzle number
Nu	Nusselt number
R	Gas constant [J/kg.K]
Re	Reynolds number

RN	Shaft speed increase rate [krpm/s]
p	Pressure [kPa]
Pr	Prandtl number
PW	Mechanical or electrical power [kW]
Q	Thermal power [kW]
Q_{abs}	Absorbed thermal power [kW]
Q_{in}	Initial received thermal power from sun [kW]
R_I	The resistance for collector-emitter current (on-state resistance) [Ω]
R_s	The resistance of motor stator [Ω]
T	Temperature [K]
t	Time [s]
tc	Time constant [s]
t_f	Solar parabolic dish focusing time [s]
U	Heat transfer coefficient [W/m^2.K]
$V_{0,I}$	The voltage of IGBT at zero current [V]
V_{ce}	Collector-emitter voltage [V]
V_c	Collector voltage [V]
V_q	q-axis electric voltage [V]
V_d	d-axis electric voltage [V]
V_{jet}	Jet velocity in the cavity receiver [m/s]
V_{plenum}	The volume of the plenum for considering volume dynamics [m^3]
Z_p	The poles of electric motor

Subscripts

$01-06$	Thermodynamic cycle stations
amb	Ambient
c	Compressor

cav	Cavity
$conv$	Convection heat transfer
$conv, loss$	Convection loss from receiver to ambient
D	Design condition
e	Electric
eff	Effective
f	Focus
g, gen	Generation
m	Mean
max	Maximum
min	Minimum
mf	Modified
mot	Motoring
opt	Optical
rad	Radiation heat transfer
$rad, loss$	Radiation loss
ref	Reference
$recu$	Recuperator
$recv$	Receiver
$recv, in$	Receiver inlet air
$recv, out$	Receiver outlet air
ss	steady-state
t	Turbine

Abbreviations

AC	Alternating current
CCGT	Combined cycle gas turbine

CCPP	Combined cycle power plant
CSP	Concentrated solar power
CFD	Computational fluid dynamics
DC	Direct Current
DLR	German aerospace centre
DNI	Direct normal irradiance
DOE	Department of Energy
EAs	Evolutionary algorithms
EC	European commission
EFMGT	Externally fired micro gas turbine
GT	Gas turbine
GTCCs	Gas turbine combined cycle
ICMF	iterative constant mass flow
ICV	Inter component volume
IEA	International energy agency
IGBT	Insulated-gate bipolar transistor
ISA	International standard atmosphere
ISO	International Organisation for Standardisation
LFR	Linear Fresnel reflector
MGT	Micro gas turbine
MPP	Maximum power production
OMSoP	Optimised microturbine solar power
PDC	Parabolic dish concentrator
PI	Proportional Integral controller
PID	Proportional Integral derivative controller
PTC	Parabolic trough concentrator

PMSM	Permanent magnet synchronous machine
PV	Photovoltaic
RES	Renewable energy source
RMS	Root mean square
SM	Surge margine
SS	Self-sustaining
ST	Solar tower system
TOT	Turbine outlet temperature
TIT	Turbine inlet temperature
VIGV	Variable inlet guide vane

Chapter 1

Introduction

The consumption of renewable energy has been increasing in recent years, as the world faces challenges related to climate change and population growth. The growing energy demand has led to a significant increase in greenhouse gas emissions, which has contributed to the problem of global warming. Figure 1.1 illustrates the global surface temperature compared to the 20th-century average each March from 1880 through 2022 [1]. As can be depicted in this figure, March temperatures have increased by 1.53 degrees Fahrenheit (0.85 degrees Celsius) per century. The last time Earth had a cooler-than-average March was 1976. This undesirable phenomenon has an impact on the environment, society, and economy including changes in precipitation patterns, sea level rise, changes in ecosystems, and increased costs from extreme weather events.

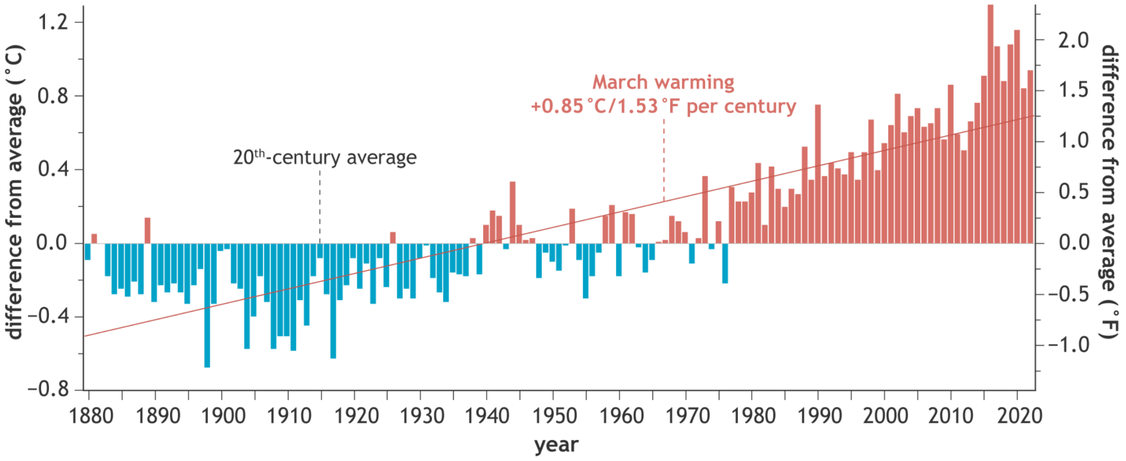

Figure 1.1: Global surface temperature compared to the 20th-century average each March from 1880 through 2022.[1]

In response to these challenges, many countries have set targets to achieve net zero greenhouse gas emissions by 2050[2]. This involves reducing greenhouse gas emissions as much as possible and then offsetting any remaining emissions through measures such as carbon capture and storage, afforestation, or investment in renewable energy sources (RES). Renewable energy plays a crucial role in achieving these targets, as it has the potential to provide clean, sustainable energy without the emissions associated with fossil fuel-based energy sources. Technologies related to renewable energy sources such as wind, solar, hydroelectric, geothermal, and bioenergy have been growing rapidly in recent years, and many countries have set ambitious targets for their deployment.

Apart from including more renewable energies in electricity generation to deal with climate change, there is another challenge that is highlighted in today's world. Despite the progress made in enhancing electricity access [3], a considerable number of individuals, estimated at around 759 million globally, still lack access to electricity according to the International Energy Agency's (IEA) 2020 report [4]. There are various reasons for this, including economic barriers, lack of infrastructure, and remote geography. One solution to this problem is the use of decentralised and off-grid renewable energy solutions such as solar panels, wind turbines, and small hydro-power systems. These technologies can provide reliable and sustainable energy to those who are currently without access, ultimately improving their quality of life and supporting economic development in these regions.

However, the transition to renewable energy for decentralised purposes is not without challenges. The intermittent nature of some renewable energy sources, such as solar and wind, means that energy storage and grid management solutions are required to ensure a reliable supply of electricity. Additionally, the cost of renewable energy technologies is often higher than that of fossil fuel-based energy sources, although the costs are declining as the technology advances and economies of scale are achieved [5].

1.1 Solar energy power generation

Solar energy has tremendous potential for power generation on Earth. The amount of solar energy that reaches the Earth's surface in just one hour is greater than the amount of energy consumed by the entire world in one year [6]. Figure 1.2 shows the remarkable potential of power generation by solar energy on the Earth. The IEA estimates that solar energy could provide up to 27% of the world's electricity by 2050, which would require an increase in solar capacity by a factor of 10 from current levels.

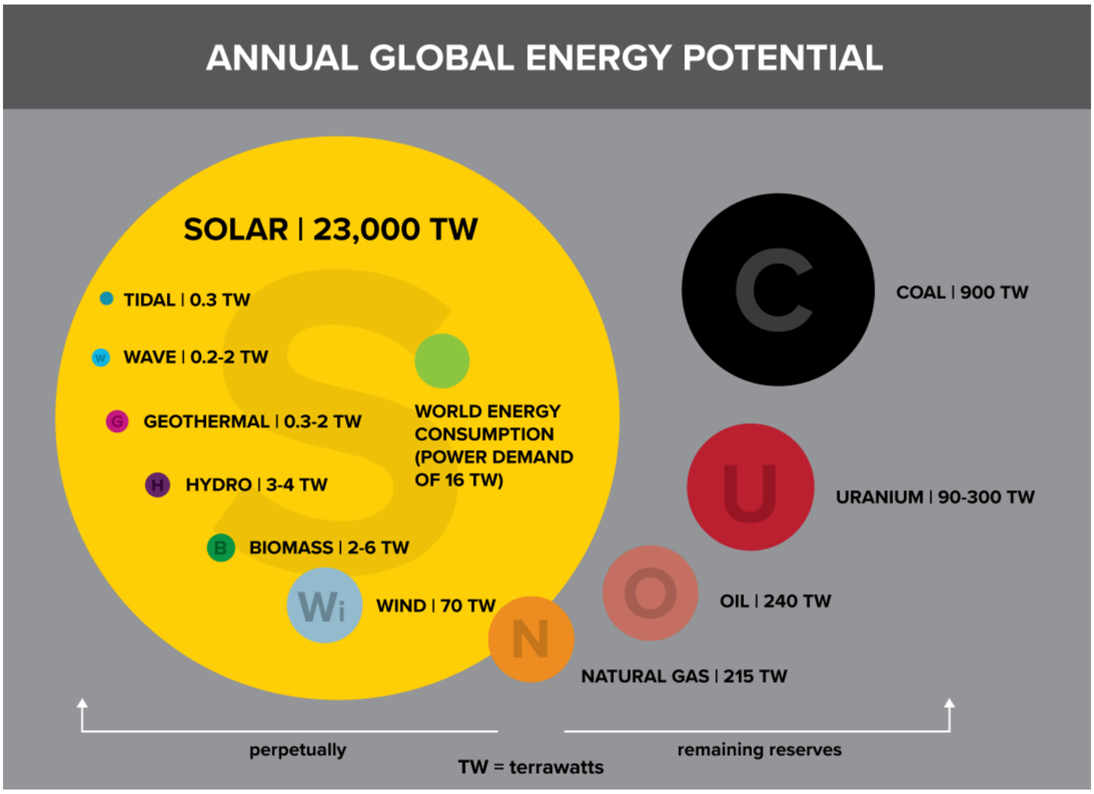

Figure 1.2: The potential power that could be generated by different energy sources on the Earth [6].

Solar power generation is typically used for electricity generation through two primary methods: concentrated solar power (CSP) and photovoltaic (PV) power. CSP technology also referred to as solar thermal power generation, functions in a manner similar to traditional thermal power generation by converting thermal energy into electricity. In contrast, photovoltaic solar panels are distinct from solar thermal systems as they do not utilise the sun's energy to produce thermal power. Rather, they harness sunlight through the photovoltaic effect [7]. CSP systems coupled with efficient thermodynamic cycle engines have been shown to have higher power density and efficiency compared to PV systems, making them a potential candidate for distributed power generation applications [8].

1.2 Concentrated solar thermal power system

There are several types of CSP systems that can be used for generating electricity. These systems use mirrors or lenses to concentrate sunlight onto a small area, heating a fluid which then drives a turbine to produce electricity [9]. The main CSP technologies are shown in Figure 1.3.

Parabolic trough concentrators (PTC) use long, curved mirrors to concentrate sunlight onto a tube running along the focal line. A fluid (usually oil or water) is heated as it flows through the tube and is used to generate electricity via a steam turbine. The temperature of the working fluid can range from around 250°C to over 500°C depending on the specific application [11]. Parabolic trough systems are the most widely used CSP technology and have been in use since the 1980s [12].

Solar tower (ST) systems are comprised of a field of mirrors or heliostats that reflect sunlight onto a central tower that contains a receiver at the top. The receiver absorbs the concentrated sunlight and heats a working fluid, which is then used to generate electricity. ST systems can operate at higher temperatures than parabolic trough systems, typically in the range of 500°C to 1000°C [13].

Linear Fresnel reflectors (LFR) use flat mirrors to concentrate sunlight onto a linear receiver that runs parallel to the mirrors. The heat transfer fluid in the receiver absorbs the concen-

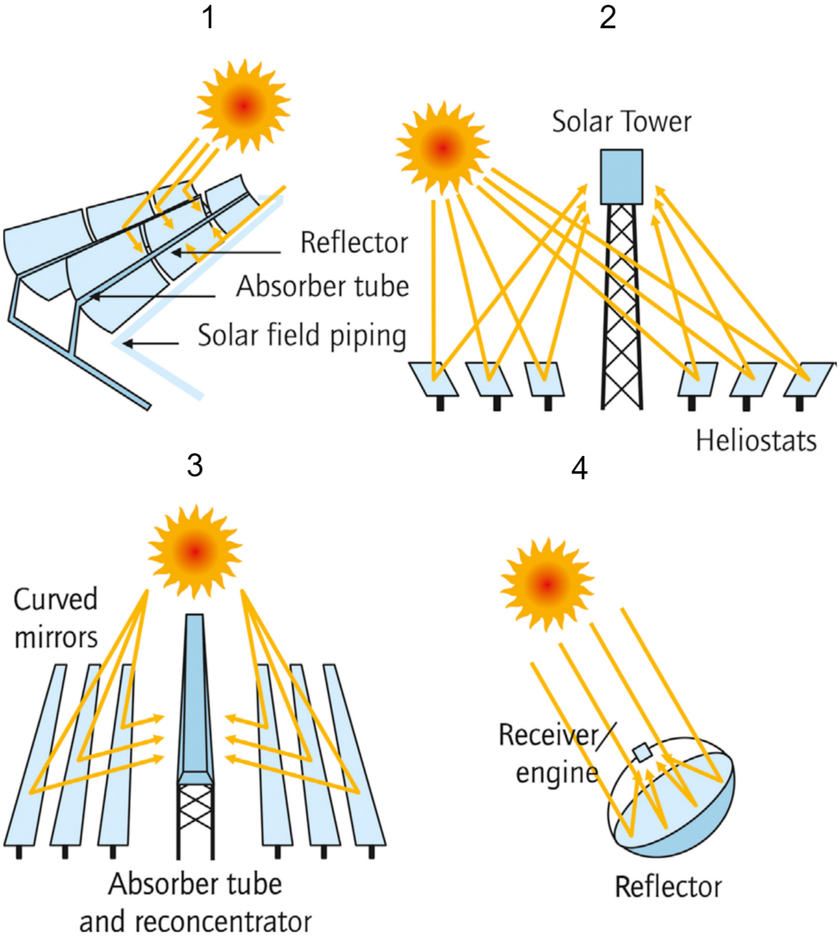

Figure 1.3: CSP systems: (1) parabolic troughs, (2) heliostat fields with central tower, (3) linear Fresnel reflectors and (4) parabolic dishes [10].

trated sunlight and transfers the thermal energy to a power cycle, which generates electricity. LFR systems typically operate at temperatures similar to parabolic trough systems, ranging from 250°C to 500°C [14].

A parabolic dish concentrator (PDC) or CSP dish uses a parabolic-shaped reflector to concentrate sunlight onto a receiver located at the focal point of the dish. The receiver typically contains a heat transfer fluid which is warmed up to high temperatures of up to 700-1000°C [15]. This thermal energy can be used directly for industrial processes, or it can be used to generate electricity through a heat engine such as a Stirling engine. Parabolic dish systems are relatively small in size and are often used in remote or off-grid locations to provide electrical or thermal power where it would otherwise be difficult or expensive to obtain.

Parabolic dishes are equipped with two-axis tracking that enables them to face the sun with their full aperture and avoid the so-called ‘cosine loss effect’ which is a common problem in other CSP technologies. These systems are modular and can be easily scaled up or down depending on the energy needs of the user. This makes them highly versatile and adaptable to a wide range of applications [16]. Parabolic dishes have the highest concentration ratio among all of the CSP technologies [17]. Concentration ratio which refers to the geometric concentration ratio is the ratio of the effective areas of the concentrator and receiver. This ratio defines the portion of the concentrated power in the receiver. Table 1.1 illustrates the major characteristics of the four types of CSP system technologies.

Parameter	**PTC**	**LFR**	**ST**	**PDC**
Capacity [MW]	10-200	10-200	10-150	0.01-0.03 [18]
Concentration ratio [ ]	25-100	70-80	300-1000	1000-3000
Operating temperature of solar field [K]	563-823	523-833	523-923	393-1773

Table 1.1: Selected significant attributes of various CSP technologies [19].

The most commonly used thermal engine that is combined with a parabolic dish in CSP systems is the Stirling engine. According to the US Department of Energy (DOE), as of 2021, over 95% of parabolic dish CSP installations worldwide use Stirling engines. Stirling engines are well-suited for use in CSP dish systems because they can operate at high temperatures (up to 1000 °C) and have high thermal efficiency (up to 30 %) [20]. Stirling engines can operate at high pressures as well, typically between 1 to 30 bar[21]. While Stirling engines can achieve high thermal efficiencies, they can also be more expensive to manufacture and maintain compared to other heat engines such as micro gas turbines. They can experience efficiency losses due to heat and high-pressure fluid leakage. Furthermore, these engines have a relatively low power density compared to other heat engines. While Stirling engines are typically designed to operate on solar-generated thermal energy, micro gas turbines or reciprocating engines as other types of heat engines can operate using a wide range of fuels [22].

Figure 1.4 shows the relationship between the geometric concentration ratio and the operating temperature according to the heat engine or the associated thermal cycle. It can be observed that as the concentration ratio increases, the operation temperature increases as well which has been also seen in table 1.1. Therefore, since the operating temperature of the gas turbine is above 900°C, it has a corresponding concentration ratio of about 1100. Consequently, the concentrated solar power technology that works with the gas turbine should have a concentration ratio above 1000 which makes the parabolic dish a suitable choice for the gas turbine [23].

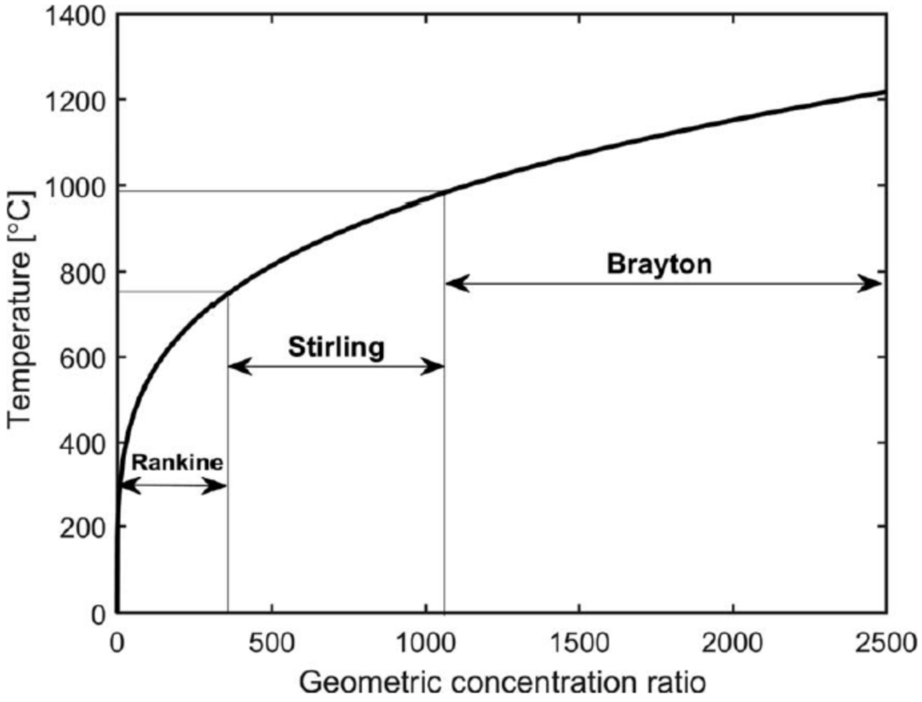

Figure 1.4: Optimum operation temperature changes with concentration ratio [23].

1.3 Solar-powered micro gas turbines

Micro gas turbines (MGTs) are a type of gas turbine that can generate power up to 500 kW [24]. However, it is more accurate to describe their power range as typically ranging from a few kilowatts to a few hundred kilowatts. The specific power range can differ based on factors such as the manufacturer, design, and intended application of the micro gas turbine [25]. A micro gas turbine is a small-scale power generation system that operates on the Brayton cycle. The cycle consists of four major components, namely, a compressor, a heat source such as a combustion chamber or solar receiver, a turbine, and a recuperator. The compressor compresses the air supplied to the heat source, where the thermal energy is added to produce high-temperature and high-pressure gases. The gas then flows through the turbine, where it expands and generates mechanical work. Finally, the gas is exhausted through the recuperator, where it transfers its waste heat to the incoming air from the compressor, thereby improving the thermal efficiency of the cycle. Figure 1.5 shows a schematic of a CSP-MGT system. An extra component, high-speed alternator (HSA) which has the duty of converting mechanical power to electrical power is also shown in this figure.

Operation of MGT with solar energy presents distinct challenges that are not encountered in conventional fuelled gas turbine systems. The primary issue is the intermittent nature of solar energy, which causes the MGT to operate differently from its intended design conditions due to the fluctuating input thermal power. To illustrate, figure 1.6 depicts the variation of solar direct normal irradiance (DNI) over three sample days in Cassacia, Italy, which include a sunny day, a cloudy day, and a day with no significant solar input. These plots are provided with ten minutes resolution.

During a cloudless day, the input thermal power from the sun exhibits a smooth dome-shaped pattern that begins in the morning and persists until the evening. By contrast, on a

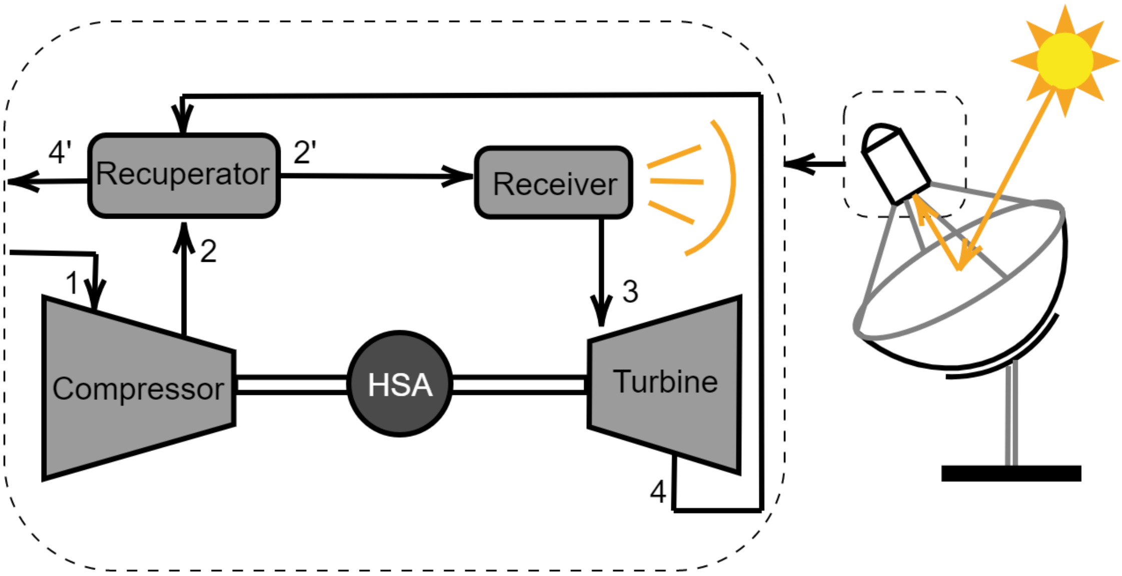

Figure 1.5: Schematic of a CSP-MGT system.

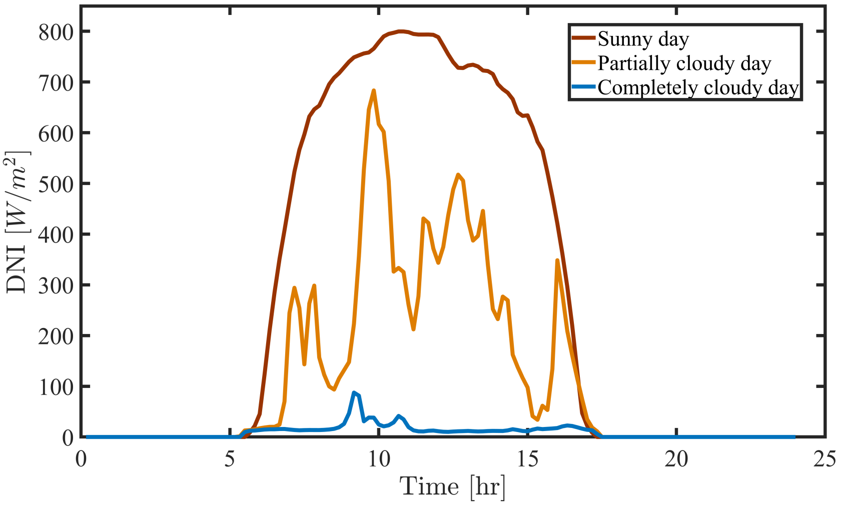

Figure 1.6: Hourly variation of the solar irradiance for Cassacia (Italy) for three sample days [26].

cloudy day, the DNI that reaches the surface is reduced due to sunlight scattering and absorption by clouds. The extent of DNI reduction during a cloudy day varies depending on cloud type, thickness, time of day, and season. This reduction can range from 50% to 90% compared to a clear sky day, depending on the severity of the cloud cover [26]. Furthermore, significant variations in DNI values occur throughout the day, which directly impact the operation of solar-powered MGTs. In both sunny and cloudy conditions, the input power to the MGT is not constant, resulting in transient operation throughout the day. During a sunny day, the MGT operates from early morning until the input thermal power is insufficient, usually in the evening. On the other hand, during a cloudy day, the MGT may shut down in the middle of the day and require multiple start-ups. Since solar thermal power is the primary source for solar-powered MGTs, evaluating their transient performance during start-up and operational stages afterwards is essential. Transient analysis of these performances is crucial since it makes a basis for the development of engine controllers and the optimisation of operating schedules while it provides a benchmark for model-based diagnosis and prognosis solutions. Among all transient conditions, the start-up phase is the most challenging phase, particularly for solar-powered systems which will be explained in detail in the following section.

1.4 Start-up procedure of micro gas turbine

In gas turbine systems powered by fuel, the amount of fuel being supplied to the system through a combustor is the primary controlling parameter for achieving a desired operational strategy. The start-up procedure, for these systems particularly for heavy-duty gas turbines, is depicted in Figure 1.7, where each stage is shown along with its respective name. Start-up phase in heavy-duty fuelled gas turbines is generally divided into five processes according to the sequence indicated in the literature: Cranking, purge, ignition, warm-up and acceleration [27]. The figure demonstrates that during the initial stage known as cranking, the system's speed is increased using starter power, without introducing any fuel into the combustor. The target speed at this stage is usually around 20% of the rated speed. At the purge stage, the shaft speed is fixed at this speed without a fuel supply to discharge the unburned fuel captured inside the gas turbine. Afterwards, fuel is supplied to the combustor and the igniter is energised which forms the ignition stage. The ignition inside the combustor warms up the gas turbine at the fourth stage which prevents the metal from developing fatigue when it is abruptly exposed to high-temperature gas. In the final stage, acceleration occurs, where the fuel flow rate is steadily increased, and the turbine is accelerated to full speed. At this stage, the fuel mass flow rate becomes the only parameter required to bring the system to the desired operating condition. During this phase, the assistance of the starter still continues and as the speed increases, it is dwarfed by the turbine assistance. When the speed reaches 60% of the rated speed, the starter is declutched from the shaft [28].

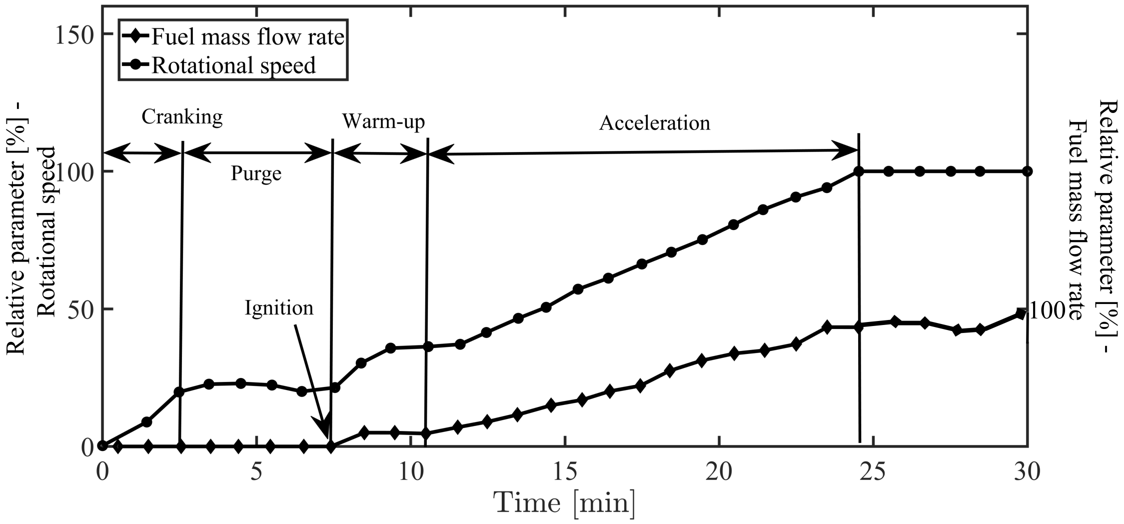

Figure 1.7: Start-up procedure for a heavy-duty gas turbine: Speed and fuel mass flow rate vs time [27].

MGTs which are fuelled also go through a comparable startup process, sharing the same stages. However, they possess a notable distinction from heavy-duty gas turbines as they are equipped with power electronics. This feature allows them to operate at different speeds and there is no declutching in their operation. Instead, they could operate in both motoring and generation modes with the help of a permanent magnet synchronous machine (PMSM) [29]. Solar-powered MGTs in case of operating in hybrid mode along with a combustor could have a start-up phase similar to the fuelled ones [30]. However, MGTs that operate solely with solar energy do not possess controllable input thermal power similar to a controllable fuel mass flow rate, which presents a challenge during their operation. While CSP dishes have the capacity to rotate in two axes, they are not typically used as a controlling parameter due to practical considerations and the large inertia of the dish. To overcome this issue, MGTs use their power conditioning systems that allow for variable speed operation and direct control of the shaft speed. During the start-up phase of a CSP-MGT, the power conditioning system controls the shaft speed to reach the targeted speed based on the input thermal power. In CSP-MGTs due to the fact that the input thermal power is impractical to control as mentioned previously, the adjustment of air mass flow rate in the system is in charge of avoiding critical incidents during the start-up phase. These incidents could include overheating of the solar receiver, which can occur due to prolonged exposure to the sun, as well as a sudden increase in the DNI value.

The start-up phase of the CSP-MGTs has two main highlighted features which are required to be studied in detail: safety and efficiency. The safety of the CSP-MGT is related to several terms attributed to physical parameters and physical phenomena in the system. The first important parameter is associated with the temperature limits of the critical component of the CSP-MGT system which is the solar receiver. Since this component is the first component that is exposed to solar irradiance, it is important to make sure that it operates safely in terms of material temperature. Overheating of the receiver metal can easily occur in case of insufficient air mass flow rate during the absorption of solar radiation. Another safety concern during the start-up phase of CSP-MGT which is not specific to this configuration, is the probability of compressor surge. This phenomenon can happen due to the narrower operation region on the compressor map at the lower speeds, as well as the presence of large components between the compressor and turbine causing a high-pressure drop. Furthermore, there are limitations with power electronics in providing electric current, which could pose a problem if the system requires more power than what the MGT can generate from the input thermal power to maintain the shaft at a specific speed. In such cases, the electric drive must supply the necessary power, which may require a larger electric current than the allowable value. Since the required power of the MGT during start-up is dominated by the compressor and is related to the speed to the power of three, higher speeds require significantly higher powers If the generated torque of the turbine is not sufficient, the torque should be provided by the drive that necessitates high electric current. Therefore, the limitation of electric current should be also taken into account in designing the speed schedule of the CSP-MGT during start-up.

In terms of the start-up efficiency of the CSP-MGTs, several cost factors are introduced. Since CSP-MGTs might undergo frequent start-ups during their operating time in a day, it is required for them to benefit from flexibility. This feature comes from a short start-up duration which helps the system to enter generation mode as shortly as it is feasible which leaves more time for the system to generate power. The second highlighted feature is the energy consumption during the start-up phase. It is important to mention here that the annual energy production of a CSP-MGT is strongly dependent on solar irradiation which is not controllable. Therefore, in order to produce the maximum energy it is required to make the system more efficient. For the generation mode, it is recommended to generate maximum permissible power for each DNI and for the motoring mode which occurs during the start-up phase, the minimum amount of energy has to be consumed for any DNI value to leave more produced energy at the end of the day. Another important parameter during the start-up is the maximum power that is required for this phase. In fuelled MGTs, a starter provides electric power to the system until shaft speed reaches self-sustaining speed which is normally less than the nominal speed. However, in CSP-MGTs the assistance of an external electric power exists until even the rated speed of the related DNI is reached. When these systems are grid-connected, they obtain their initial electric power from the grid. However, in standalone mode without grid access, the initial power is provided by an external source like a battery. In such cases, determining the capacity of the external power source becomes crucial, as it must meet the maximum power requirements during start-up. It is advisable to minimise the capacity of this power source to reduce initial investment costs.

In addition to safety and efficiency which must be taken into account during the start-up phase of CSP-MGTs, there has to be a characterised start-up procedure specifically for solar-only configuration of MGT. Since the start-up procedure of these systems, is completely different from the existing fuelled MGTs, introducing a schedule specifically for this configuration is required. Furthermore, the efficiency of the start-up was defined by three main factors. All three objectives are not achievable at the same time. To realise key design parameters of the start-up schedule of the CSP-MGT, a trade-off among the three cost factors should be provided. Additionally, all of the safety criteria should be met. In this regard, the main aims and objectives of this study are defined.

1.5 Aims and objectives

The main aim of this study is to study the transient performance of the start-up phase to find the optimal schedule. This schedule results in a start-up phase with a minimum required power, energy consumption and start-up period with consideration on the safe operation of the whole system with a focus on the solar receiver as the critical component. In order to achieve this aim, a transient model must be developed and the following specific objectives are defined for this research.

- To validate the developed transient model of CSP-MGT to ensure its accuracy.
- To design a schedule for characterising the start-up phase of CSP-MGT.
- To develop a framework to optimise the speed schedule, aiming to minimise the maximum required power, energy consumption, and start-up time during the start-up phase while ensuring a safe operation.
- To assess the annual transient performance of the CSP-MGT system, with a particular focus on developing a programme structure and determining the net produced energy.

Ultimately through the completion of this project, and through the delivery of the project objectives, it is hoped that a number of valuable contributions to the research community will be made regarding the design of the start-up phase for a CSP-MGT and the identification of crucial parameters for this process.

1.6 Contribution to knowledge

A pioneering endeavour involves developing and validating a real-time transient model for CSP-MGT systems considering both thermo-mechanical and electrical aspects of the system, focusing on start-up behaviour. This research addresses the crucial CSP-MGT start-up phase, recognising the challenges linked to intermittent solar energy-based thermal input.

Distinct from conventional fuelled gas turbines, CSP-MGTs require a custom reference speed schedule for start-up. Owing to the absence of controllable input thermal power and the consequent requirement for an alternative control strategy, the start-up protocol within CSP-MGTs deviates substantially. This has led to the design of a distinct start-up schedule exclusively tailored for CSP-MGT systems, signifying a novel addition to the solar-powered MGT community. Afterwards, an optimisation framework is devised to find an efficient and safe start-up schedule for CSP-MGT systems.

Moving beyond a single start-up analysis, the research extends its scope to encompass the yearly transient behaviour of CSP-MGT systems. Employing a structured methodology, the study evaluates the net energy output throughout a year, yielding insightful perspectives into the performance transients of CSP-MGT systems when employing optimised start-up schedules.

1.7 Thesis structure and scientific contribution

This thesis consists of seven chapters which represent the progression of this research project. Following the present introduction, a thorough literature review on the key concepts and previous research which are related to this work is presented in Chapter 2. In the beginning, the application of MGTs in power generation with the help of solar energy is explained. Different configurations of solar-powered gas turbine systems are explained, and the existing technical challenges in different configurations are demonstrated. Afterwards, the transient operation of the MGT during load-fluctuation procedures and start-up/shutdown are investigated to discover the main solutions that have been provided for controlling the operations and also avoiding any critical occurrence. The review highlighted the necessity of a transient model for solar-powered MGT. Different approaches for transient modelling were reviewed to find the most appropriate modelling technique for the CSP-MGT system. The last section of Chapter 2 is about the research on the optimisation of the start-up phase of gas turbine systems. The outcomes of Chapter 2 are the key conclusions that empower the project objectives and provide the required technical and scientific knowledge in the next chapters.

Chapter 3 focuses on developing a transient model for CSP-MGT, explaining the governing equations of each component in detail. To align with the thesis objectives, the model is designed for the start-up phase by considering thermal transients in all components and generating turbocomponent speed curves for low-speed values. To validate the model, it is compared to experimental data obtained from the OMSoP demonstration plant. It is noteworthy that validating a CSP-MGT through experimental measurement is an original study that has not been explored previously.

As CSP-MGT solely relies on solar energy, it undergoes frequent start-ups, emphasising the importance of the start-up phase. In Chapter 4, a schedule for the CSP-MGT start-up phase is established following the development of the transient model for the system. This novel endeavour has primarily been applied to heavy-duty gas turbines and fuelled MGTs in the past and an established start-up schedule for a CSP-MGT has not been found in the literature. Additionally, this chapter introduces two start-up types based on the initial conditions of the system. Furthermore, it explains a physical configuration modification made for further simulations.

The start-up phase of CSP-MGT must meet the requirements of minimum power requirement, minimum energy consumption, short duration, and system safety. Achieving these goals, which often conflict requires a multi-objective optimisation, which is the focus of Chapter 5. Using the model developed in Chapter 5, an optimisation framework is designed to optimise the start-up schedule. The framework first investigates the maximum required power and energy consumption with implementing safety constraints. The outcome is a criterion for defining the starter capacity, which is then used in further optimisations. The second set of objectives includes energy consumption, and start-up time along with the constraints for safety considerations, resulting in optimised speed schedules for different DNI values. These schedules are used for annual calculations in Chapter 6.

In Chapter 6, the optimised start-up schedules obtained for various DNI values are evaluated on a yearly time scale. The first section of the chapter deals with a sensitivity analysis to determine the highest DNI intervals that can be used for selecting speed schedules, as there cannot be one schedule for every measured DNI. Following this, another sensitivity analysis is carried out to investigate the impact of initial conditions on the speed schedules. Finally, the days of the year are categorised, and an annual analysis is conducted to determine the net produced energy, which is the difference between consumed and produced energy.

Final conclusions of this research are summarised in Chapter 7. The outcomes of each chapter are evaluated against the project objectives. Recommendations for further work in future research are provided afterwards.

1.8 Publications

Conference paper

Shamekhi Amiri, S, Al-Zaili, J, Sayma, AI. "Development of a Dynamic Model for Simulating the Transient Behaviour of a Solar-Powered Micro Gas Turbine." Proceedings of the ASME Turbo Expo 2022: Turbomachinery Technical Conference and Exposition. Volume 4: Cycle Innovations; Cycle Innovations: Energy Storage. Rotterdam, Netherlands. June 13–17, 2022. V004T06A001. ASME.

Chapter 2

Literature Review

2.1 Introduction

This chapter provides a comprehensive overview of the advancements in solar-powered gas turbine systems, focusing on their transient operations. Recent research activities in this field are discussed, with a specific emphasis on control strategies for dealing with different transient procedures. The start-up phase, as one of the important transient operations in MGTs, is the primary focus of this chapter. The challenges encountered during the start-up phase of CSP-MGTs are outlined based on the previous studies. The scope extends to examining different types of existing gas turbine systems, including a detailed review of start-up procedures, cost considerations, and safety challenges. Furthermore, various methodologies for transient modelling of gas turbine systems with different configurations are reviewed to establish a foundation for analysing the transient behaviour of CSP-MGT. Another aspect explored in this chapter is the importance of optimising the start-up phase for CSP-MGT, where a thorough review of start-up optimisation techniques for heavy-duty gas turbine systems is addressed to enhance system flexibility and safety. At the end of the literature review, a summary is presented to highlight the main research gaps.

2.2 Solar-powered gas turbine systems

Gas turbine systems have been the scope of investigation by many researchers to investigate their applications for integrating with CSP technologies. This concept for electricity generation is not novel and was first introduced by NASA [31]. Afterwards, a purely solar-powered closed-cycle MGT with a capacity of 10 kW_e and a sensible thermal storage system based on melted salt was developed [32] by them. The system underwent endurance testing under constant solar radiation conditions, similar to a low Earth orbit, and achieved a continuous operation for 38,000 hours. As the system was designed to operate outside the Earth's atmosphere, input heat transients were not considered.

Unlike NASA's project, solar-powered energy systems on Earth face a significant challenge due to the fluctuations in DNI. Figure 2.1 provides an example of the hourly average frequencies of DNI in Rome between 2004 and 2005, demonstrating the high level of intermittency in solar irradiance throughout the day. The ideal DNI alteration is depicted by the blue curve, while the red curve represents the actual values deviating from the ideal due to cloud cover. These variations directly impact the input thermal power to the gas turbine through the components of the CSP system. The fluctuating input thermal power leads to the gas turbine operating under off-design and transient conditions, which adversely affects the overall system performance. As a result, many solar-powered gas turbine systems adopt a hybrid configuration that combines solar energy with an auxiliary combustion process. This hybrid approach ensures stable operating conditions for the gas turbine despite the DNI variations. A simple hybrid solar micro gas turbine power plant is shown in Figure 2.2.

In the field of solar-hybrid gas turbine systems, the European Commission (EC) previously funded three solar-hybrid gas turbine demonstration projects; solar hybrid Gas Turbine Electric (SOLGATE) power system, solar-Hybrid power and Cogeneration (SOLHYCO) plants and

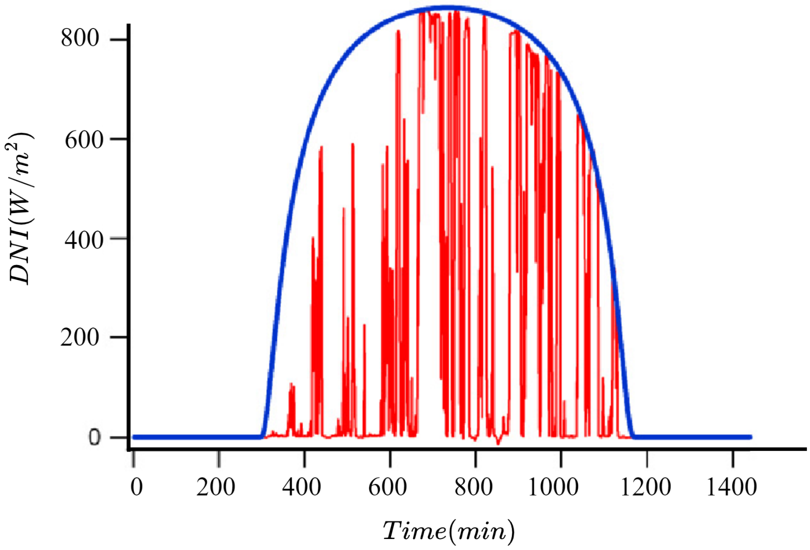

Figure 2.1: Example of a daily variation of DNI in Rome between 2004 and 2005[33].

solar Up-scale gas turbine system (SOLUGAS). The main goal of these projects was to demonstrate the technical feasibility and cost reduction potential of solar-hybrid gas turbine systems, with a focus on improvement of the solar receiver design and performance [35, 36]. The SOLHYCO project involved observing systems under solar-hybrid operation for several hours, with 2 hours dedicated to solar-only MGT operation. However, the testing phases were cut short due to various challenges. These challenges included problems with emergency shutdowns, difficulty controlling the heat from multiple sources, handling high combustion chamber inlet air temperatures, defects in the solar receiver cavity, and unsatisfactory combustion during MGT start-up,[37, 38, 39]. Another solar-hybrid gas turbine system was AORA Solar's Tulip co-generation system referenced in the literature [30]. The system had a rated electrical and thermal power output of 100 kW_e and 170 kW_t, respectively. The installation of this system was done in two research and development sites: Kibbutz Samar, in Israel and Plataforma Solar de Almeria, in Spain. The former was commissioned in 2009, while the latter was commissioned in 2012. Unfortunately, there is no published literature readily available on the performance of these two demonstration plants. More recently, EC funded a project named optimised micro gas turbine solar power (OMSoP). In this project, the MGT system was intended to be a modu-

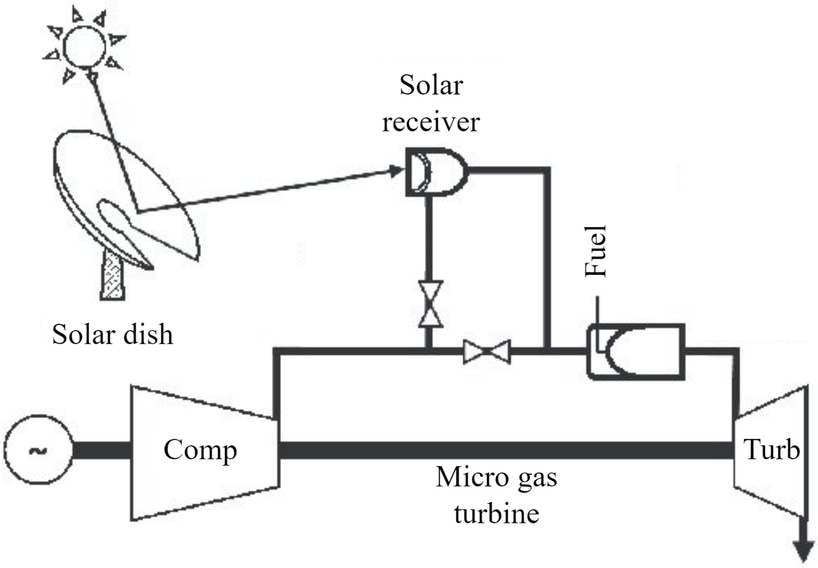

Figure 2.2: A simple hybrid-solar micro gas turbine system power plant [34]

lar design, with the capability of producing 3-10 kW_e of electricity. The solar-only system was based on parabolic dish concentrator technology and the conventional Stirling engine was replaced by an MGT system designed by City, University of London. Experimental tests showed overheating of the MGT system bearings, limited the TIT to a maximum of 270 °C which was well below the design point value of 800 °C. Consequently, the experimental tests yielded a useful work output of only 0.9 kW_e [40], with most of the measurements taken during the motoring mode at the start-up or shutdown phases of operation. During the start-up phase, another challenge arose as a result of manually controlling the shaft speed and the lack of optimal speed schedules based on the DNI values. This situation sometimes led to the solar receiver being at risk of overheating.

Solar-powered gas turbines encounter different transient operations, regardless of their classification as heavy-duty or low power, configuration as hybrid or solar-only, and whether they operate independently or are connected to the grid. Failure to anticipate these transient operations during experimental testing can result in previously mentioned issues in some test plants. Therefore, it is imperative to evaluate the transient performance of gas turbine systems to ensure their safe and reliable operation. This evaluation necessitates the development of a mathematical model, which serves multiple purposes such as designing control systems, analysing control strategy performance, and guaranteeing the safe and reliable operation of gas turbines under transient conditions such as start-up. On the other hand, MGTs differ from heavy-duty gas turbines in their typical applications. They are commonly employed in scenarios that demand rapid response to fluctuations in power demand or load. Additionally, they present a favourable option when the power input originates from intermittent renewable energy sources. During transient events, MGT systems undergo sudden changes in operating conditions, which can lead to adverse effects like thermal stresses and mechanical vibrations. Hence, evaluating the transient performance of MGTs is essential to assess their capability to adapt to these changes and maintain stable operations. Through an analysis of the system's transient behaviour, potential issues can be identified, and appropriate control strategies can be devised to mitigate them [41].

2.3 Transient operations of gas turbine systems

The occurrence of transient operations in gas turbine systems stems from a range of factors, encompassing load fluctuations, and variations in ambient conditions especially in RES-integrated systems, start-ups and shutdowns. Furthermore, hybridisation scenarios may also induce transient operations as a consequence of transitioning between different configurations. In both hybrid configurations and fully RES-driven systems, the fluctuating nature of RES may lead to the need for frequent load ramping during periods of intermittency. The intermittency of the energy source affects the performance in a way similar to the load variation in standalone systems. Such frequent load ramps could increase the risk of failures including efficiency loss and safety risks. Therefore, a transient performance study of gas turbines is of paramount importance to comprehend various factors associated with sharp transients. The current literature review focuses on two primary categories: transient events caused by load fluctuations resulting from RES integration and transient events arising from start-up and shutdown procedures. The subsequent sections delve into an in-depth analysis of these two key categories along with the modelling approaches, presenting an overview of pertinent research findings and highlighting their significance in the context of the transient operation of gas turbine systems with a focus on MGTs.

2.3.1 Load fluctuation procedures

Load changes have been accounted by a few studies in the literature. In reference to fuelled MGTs in standalone mode, Bracco et al. [42] assessed the part-load and transient performance of a 65 kW_e MGT during load variations. The study found that shaft speed varied with the load due to controlling turbine outlet temperature (TOT) to be constant. This has been done to meet the electrical power demand set by the user. It is worth noting that, the shaft speed was not controlled and only a maximum threshold limit value for the rotational speed was assumed. The effect of the two operating modes of variable and constant shaft speed operating modes on the transient behaviour of MGT has been also studied by several authors. In this regard, Duan et al. [43] compared the transient performance of simple and recuperated MGT cycles at constant and variable speed modes. The study found that the recuperated MGT at variable speed mode was the most efficient cycle mode among the investigated modes in their study, although it may experience surging and increased turbine inlet temperature (TIT) at low speeds during low loads. In another study, Wang et.al. [44] also confirmed this result by showing that the operation with variable speed for MGTs is better compared with a constant speed, which is shown in Figure 2.3.

Apart from fuelled MGTs, solar-hybrid gas turbine configurations, also face several extra dynamic operations that have been studied in the literature. For instance, during solar-rich

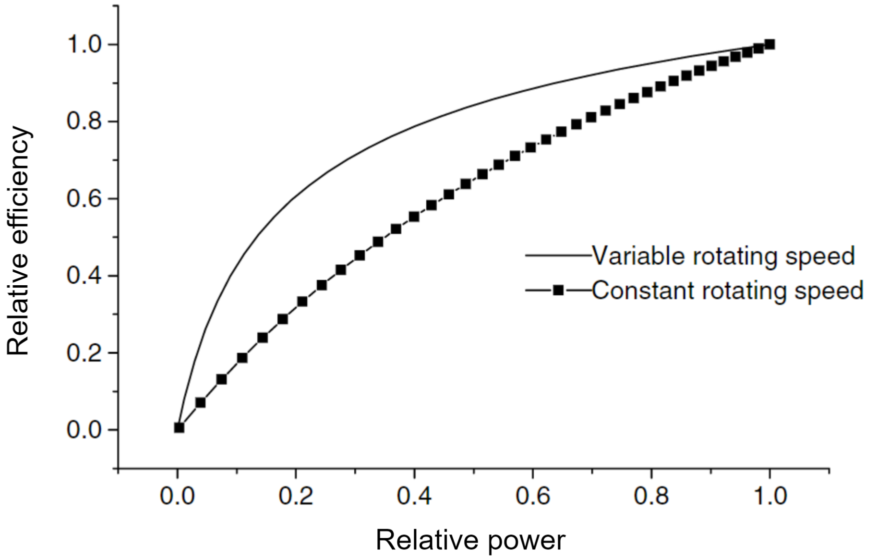

Figure 2.3: Relative efficiency and relative power of MGT under constant and variable speed operation [44].

hours, the gas turbine operates on solar-based energy with less combustor fuel flow and a sudden reduction in DNI urges the gas turbine to activate the higher fuel flow. Similarly, when the solar irradiance is restored the fuel flow is reduced. This fuel variation leads to the flame-out phenomenon and dynamic instabilities in the combustor, thus increasing the complexity of the system. In this regard, Tsoutsanis et al. [45] found the maximum and minimum fuel flow rates corresponding to flame-out in the combustion chamber by using a transient simulator. Furthermore, sudden generator load rejection in solar-hybrid gas turbine systems operating in a standalone mode leads to over-speeding of the shaft due to the higher volumetric and thermal capacity of these systems. It was suggested to either install an additional relief system (such as a blow-off valve) or increase the rotor inertia to achieve the safety of the system [46]. The shaft inertia could be changed by integrating additional rotating mass or by using a proper electric generator. Another research also highlighted the same over-speeding issue in a megawatt-scale gas turbine [47].

The pertinent literature exists in the domain of transient performance study of solar-powered gas turbines for megawatt-scale power generation through the solar-hybrid units as reported by Traverso et al.[48]. Regarding solar-hybrid MGTs, Chen et al.[49] studied the transient performance of solar hybrid 100 kW_e MGT integrated with thermal energy storage (TES) during load and DNI changes for a standalone mode. They found that solar integration to a fuelled MGT reduces fuel consumption but affects stability. In order to avoid instability, the heliostats have to be adjusted during load decrease, and the load has to be decreased gradually to avoid compressor surge during load increase. In another study, Yang et al.[50] also investigated the part-load operation of a 10 kW_e solar-powered MGT in a hybrid configuration along with thermal storage under real-world DNI variations. In order to overcome instabilities and set point tracking, real-time control strategies were proposed and implemented in transient simulations. The researchers demonstrated that simultaneous control of shaft speed and TOT was effective in ensuring high and stable system performance during favourable weather conditions. The control system ensured an anti-surge operation of turbomachinery components as well.

Apart from solar-hybrid MGTs, studies on the transient performance and control studies of solar-only MGTs are found to be scarce. Amelio et al. [51] proposed an airflow control method for a solar-only MGT operating with a heliostat field. By adding an auxiliary compressor and a bleed valve at the compressor entrance and the turbine exit, respectively, the air mass flow rate could be regulated to maintain constant TIT/system efficiency. The air mass flow rate in the cycle has been modelled in order to vary as a function of the incident heat flux on the solar receiver. Additionally, the heliostat regulation has been also implemented to control the average incident flux on the solar receiver. In terms of solar-only MGT systems operating with CSP dishes, Ghavami et al.,[8] proposed maximum permissible power (MPP) as the first choice for these systems when the generated power is fed to a large grid. However, when the system is required to be load-oriented, recuperation control can be considered for power generation.

2.3.2 Start-up/shutdown procedures

In addition to the transient operations due to load fluctuations, start-up and shutdown phases have been the scope of many studies. The startup process of a fuelled MGT system from static to generation includes motor startup, ignition, speed acceleration, motor switching to generator and power acceleration [52]. The first stage is motor startup from zero to ignition speed when PMSM supplies power to counteract the consumption power of the compressor and bearing to drive the MGT to operate. At the ignition speed, fuel is ignited and burned with air in the combustor. This causes the TIT to rise sharply, and the turbine begins to generate power to assist the motor. Speed acceleration continues from ignition speed until the self-sustaining speed is reached. Afterwards, speed is accelerated and the generated net power is increased from the self-sustaining operating point to the design point. In terms of self-sustaining operating point, Guan et al.[52] have done a study to evaluate self-sustaining performance during the start-up of a 30 kW_e MGT, which determined the self-sustaining transition boundary for the shaft speed, and the fuel consumption range. The study revealed that the self-sustaining operating point is closely tied to the shaft speed regardless of the maximum level of fuel flow adjustment. Therefore, forecasting fuel consumption range is crucial for stable MGT operation during start-up.

One of the primary issues frequently observed during the start-up phase involves compressor surge, which occurs as a consequence of elevated pressure losses in the downstream section of the compressor. This could happen due to implementing a hybrid configuration for solar-powered MGTs. Ssebabi et al. [53] focused on the prediction of an MGT performance under a solar-hybrid operation. They discovered that the addition of a solar receiver to the system alongside the combustion chamber induces pressure losses in the system and, to compensate for them, the equilibrium running point(a steady state operating condition) shifts to a higher-pressure ratio region of the compressor and approaches the surge margin. For the solar-hybrid operation, a surge margin of 21% was determined, which is notably lower than the 50% surge margin calculated for standard MGT system operation. However, they did not evaluate the surge margin during the start-up phase. Zanger et.al [54] have studied the stability of solid oxide fuel cell/micro gas turbine (SOFC/MGT). They found that in order to operate under safe conditions, surge margin has to be increased during the start-up phase. They have suggested that the two major possibilities to enlarge the surge margin are extraction of bleed-air and reduction of the target TOT. In another study, JeongMin Seo [55] explored the viability of start-up and self-sustaining capability for a fuelled MGT. They methodically controlled the rotational speed during the start-up sequence and observed that the MGT's operating point remained safely distant from the surge line throughout the entire start-up and self-sustaining operation. This means that compressor surge prevention methods during the start-up phase depend on the system configurations and control strategies.

Another important issue that is likely to happen in MGTs during start-up, especially for solar-powered MGTs, is the overheating of the main components in the system. Partners from the OMSoP project [29] have reported that the full reliance on solar energy makes the MGT susceptible to solar receiver overheating due to sudden variations in DNI, particularly during the start-up phase. In some researches where heliostat fields were utilised, it was suggested to defocus them to control input thermal power and protect the solar receiver from overheating. However, CSP-MGTs lack the quick response necessary to prevent solar receiver overheating [29]. In light of this, Ghavami et al. [56] proposed an alternative control strategy involving the adjustment of air mass flow rate within the solar receiver. Nevertheless, the performance of this strategy has been assessed only for the generation mode of CSP-MGT, and it hasn't been evaluated for the start-up phase. Wang et al. [57] evaluated the start-up of a CSP-MGT experimentally with a focus on the solar receiver component. In this study which belonged to the OMSOP project [29], Wang et al. [57] conducted an experimental study on one kind of solar receiver which is an impinging cavity receiver, evaluating the transient performance of a prototype in a Fresnel lens-based solar simulator and externally fired MGT. It was seen that the temperature uniformity of the absorber is acceptable. However, there has been no research conducted to identify a start-up sequence that avoids any overheating issues in the solar receiver.

Apart from safety challenges during start-up, there are other aspects that are required to be analysed according to the system configuration and application. These aspects including start-up time and start-up power requirement are considered to be the cost factors of a start-up phase which have been tried to be minimised in the literature. There are limited studies with detailed discussions of the full start-up time of an MGT. A very early study by Cantoni [58] showed that the time required for motor starting was inversely proportional to TIT. Recently, Haiqing et al. [59] aimed at reducing the start-up time and start-up power consumption of a fuelled MGT. In their study, they evaluated the effect of high thermal inertia (as a result of the recuperator) and operating variables on start-up time and power consumption. They have shown that adjusting the sequence of acceleration and fuel injection could help overcome the thermal inertia of the recuperator, which was critical for a fast start-up. However, minimising the cost factors of start-up comes with challenges of system safety.

In this regard, other studies have been done which were mostly on large gas turbines that are used in combined cycles [60, 61]. In these systems, the start-up procedure includes thermal transients of several extra components associated with the secondary thermodynamic cycle like steam turbines including high-pressure drums, steam turbine rotors and superheaters [62]. Rossi et al.[63] analysed the transient performance of a gas turbine combined cycle, focusing on the start-up procedure and associated mechanical stresses on the steam turbine rotor resulting from temperature gradients. It was shown that the required time for start-up is crucial from an economic point of view, even though this time is limited by thermal stresses imposed on the components by temperature gradients. Therefore, rotor stress control is done by altering the gas turbine load ramp (as a controlling variable in the gas turbine) and changing the duration of the start-up operation. While the start-up process of combined cycle gas turbines involves thermal safety considerations not present in regular gas turbines, the challenge of thermal safety also exists in solar-powered MGTs. However, in solar-powered MGTs, this challenge is attributed to the MGT system itself rather than the components in the bottoming cycle which use the waste heat of the gas turbine [64].

2.3.3 Transient modelling approaches of gas turbine

Gas turbine transient behaviour has been the subject of analytical and experimental research since the early 1950s, particularly after the introduction of the twin-spool engine [41]. The development of digital computer technology led to the creation of transient mathematical models for gas turbines. Researchers, such as Fawke and Saravanamuttoo, developed transient mathematical models for gas turbines in 1971 [65]. Zero-dimensional transient simulation codes, such as DYNGEN, were developed by NASA for the performance study of aircraft gas turbines [66]. However, the transient performance simulations of smaller engines with radial-type turbomachinery components, such as MGTs, did not begin until 1993 [41], when a transient model was developed for solar-powered regenerative MGT. This simulation model utilised mass, momentum, and energy conservation equations to predict the low-frequency transients caused by the control system of the engine. In 2000, Kim et al. [67] initiated the development of a transient simulation model for natural gas-fuelled recuperated MGT using unsteady one-dimensional conservation equations implemented on constituent components assumed as finite control volumes. While this model considered the thermal inertia of the recuperator, it did not account for heat soakage in turbomachinery components and volume dynamics which will be explained in the following paragraphs. In order to consider these two phenomena, a code named TRANSEO was created by Traverso to address the shortcomings of the existing code with lumped volume approach. This code was developed specifically for the dynamic performance analysis of energy systems [68]. Attainable results were shown to demonstrate both the accuracy of results and the adopted approach.

Volume dynamic is associated with the response delay of the MGT during external perturbations. This means that in case of a perturbation, the incoming fluid mass flow of a certain constituent component is not equal to the outgoing mass flow. In fact, some of the fluid mass is accumulated in the gas path components leading to a mismatch of conservation of mass equation. This phenomenon is known as volume dynamics [41]. In this respect, two different approaches have been established in the literature: iterative constant mass flow (ICMF) and inter-component (ICV) volume methodologies. The ICMF method assumes that the incoming fluid mass flow in any control volume is equal to the outgoing mass flow [69], whereas the ICV method allows for pressure rises inside constituent components' control volumes during real transient operations [70]. Therefore, to account for this effect during transient operation which is coming from mass accumulation, artificial volumes are introduced between two consecutive components.

Although some researchers have utilised ICMF methodology, ICV method is favoured due to its ability to produce smoother operating line trajectories on turbomachinery performance maps during sharp transient perturbation. In this regard, Hashmi et al.[71] also compared two previously mentioned simulation methods: i.e. the ICMF method and the ICV method. It was concluded that as ICV method gave a better physical representation of a gas turbine due to the inclusion of work and mass flow mismatch and it has been widely applied in different transient models [72]. Another comparison has been performed in [73] and considered two disadvantages for ICMF method: firstly, the admissible initial guessed values of the model are calculated by multiple iterations that make this method unsuitable for real-time condition monitoring and dynamic performance prognostic. Secondly, with the help of a model established by the ICMF method, controllers designed by engineers can satisfy control performance only at steady-state points. It was said that ICV method could describe transient behaviour more precisely in comparison with ICMF method, therefore the designed controllers would predict transient-state control performance, more accurately. This method is also preferred over the full dynamic model which one-dimensional Euler equations are used in spite of the higher capabilities of the latter model[74]. This is due to the fact that their calculation time differs by about two orders of magnitude (lower for the lumped volume with ICV method) [74]. Therefore, in the case of considering the model for a real-time simulation, the lumped volume with ICV method is preferred rather than a dynamic model that takes into account fast dynamics.

Another important aspect in the transient modelling of the gas turbine systems especially during the start-up phase is thermal transients or heat soakage which is a phenomenon of heat accumulation inside the gas turbine. In contrast to steady-state operation, there is significant heat transfer between metal and the working fluid during transient operation especially during start-up. For heavy-duty gas turbines, it has been reported that up to 30% of the fuel energy is absorbed into the metal during the start-up operation [75]. Kim et al.[27] considered heat soakage in the transient model of the start-up procedure of a large gas turbine to see the effect of transient heat absorption in the metal (casing and shaft). They have shown that 8.3% of the fuel energy is absorbed by the metal because of heat soakage. While thermal effects typically have a limited impact on the performance of large gas turbines, they can significantly affect the performance of MGTs due to the compact design of the turbomachinery, resulting in increased temperature differences over short distances. Therefore, it is necessary to take this factor into account when studying the startup phase of an MGT.

In addition to the main features of the transient model, there is another important challenge in modelling the start-up phase of gas turbine systems. Most of the start-up analyses which have been done for gas turbines had the limitation that they only could simulate the latter part of the full start-up procedure (after ignition), especially for heavy-duty gas turbines. However, simulation of the early stage of the start-up procedure is required for two main reasons. Firstly, the compressor in the low-speed region before ignition is vulnerable to exposure to critical phenomena such as compressor surge. Secondly, an accurate estimation of the starter capacity that supplies power to the gas turbine at the early stage of its start-up requires an accurate modelling of early start-up. In order to study the transient performance of a gas turbine from a stationary state (zero speed), a characteristic map of compressor and turbine is required. But they are not usually available for low speeds before ignition. Furthermore, generating the maps at low speeds is not a straightforward task. Therefore, some extrapolation methods [75] are generally used to predict compressor and turbine characteristics by using available speed data which are mostly from 50% to 100% of the design speed [27]. However, the extrapolated data can be unreliable which lead to numerical convergence problem during the simulation of the entire system. In order to overcome this problem, studies have been conducted in the literature. The accuracy of the extrapolated performance characteristic curve was improved by introducing a virtual zero-speed line [76]. Consequently, several studies have been conducted to improve the accuracy of the zero-speed line through an experimental test with a locked rotor compressor [77] and computational fluid dynamics (CFD) when the geometry is known [78]. Additionally, a study aimed at matching with compressor performance map data, using a method to move and rotate an elliptical curve, which resembles the shape of the compressor performance map [79]. It was concluded that the zero-speed line significantly improved the accuracy of the performance curves generated in the low-speed region.

In the compressor map, when the rotational speed decreases, the operating point must approach a point where the pressure ratio is one and the mass flow rate is zero. However, if extrapolation is used to find the zero-speed line in the turbine, some generated zero-lines can cause a non-matching problem in the operating point between the compressor and the turbine during the low-speed region and the operating point of the turbine map moves to a location in which the pressure ratio is greater than one when the mass flow rate reduces to zero [80]. In order to resolve the non-matching problem between compressor and turbine that could occur at low rotational speed, a novel method was proposed. This was done by making the generated low-speed curves in the turbine map pass through a zero point regardless of the shape of existing high-speed curves[80]. A zero point is where the pressure ratio is one and the mass flow rate is zero. This strategy has been used for axial gas turbines which can also be extended for radial turbines and centrifugal compressors which are the main scope of this study.

2.4 Optimisation of start-up procedure

In the previous sections, it has been seen that in order to have the minimum cost factors of the start-up phase which could be start-up time and start-up power requirement, some safety challenges must be dealt with. Since these two main cost factors have a contradicting effect on each other, an optimisation has to be done. Most of the studies related to the optimisation of the start-up are associated with large gas turbines in combined cycle power plants due to their requirement to meet daytime peaks and undergo frequent start-ups and shut-downs, sometimes over 150 start-up times a year, resulting from energy deregulation [81, 82]. The challenge in these systems is to improve plant flexibility while maintaining the efficiency and lifespan of components [83]. The start-up problem is critical for reducing emissions, thermal stress and maintaining system efficiency. Several studies have aimed to reduce start-up time while controlling the lifetime consumption of critically stressed components and considering other important aspects of the problem, such as thermal stress and pollutant emissions [84, 85]. Most studies have optimised start-up time alone using a single-objective approach while treating other aspects as constraints. To minimise start-up time, a Response Surface Method (RSM) and Genetic algorithm (GA) approach were employed to optimise the maximum stress values in the initial start-up stage by considering both the steam-metal temperature difference and the temperature distribution in the element [86]. The optimisation resulted in new start-up schedules that reduced start-up duration to less than half the previous duration.

Yoshida et al. [87] developed a method to optimise gas turbine start-up by reducing fuel gas consumption in the gas turbine and maximum thermal stress in the steam turbine. The start-up schedule was optimised by iteratively searching for the optimal combination of the start-up parameter values and evaluating multiple-objective functions. The multi-objective evolutionary algorithm was used to solve the trade-off problem. Their results showed that the developed start-up schedule could optimise the start-up process for gas turbines by defining the optimal range for design variables.

For CSP-MGTs that operate solely with solar energy, the safety of the solar receiver and other connected components is of the most importance. On the other hand, the start-up sequence which defines the cost factors has not been studied in the literature for these systems. These factors which are in contradiction with the safety of the system, should be defined by an optimisation procedure similar to the ones explained in this section for large gas turbines working in combined cycles.

2.5 Summary of literature review

The literature review emphasises that MGTs are frequently employed in scenarios requiring rapid adaptation to power variations or loads, making them a favourable option when sourced from intermittent renewable energy sources. Consequently, solar concentrated dish systems utilising MGTs in small-scale concentrating solar power plants present a viable means of efficiently harnessing solar energy and providing electricity to remote locations. However, these systems, referred to as CSP-MGTs, encounter transient operations due to the intermittent nature of the thermal power source. Furthermore, as they solely rely on solar energy, multiple start-ups are highly probable during the day which makes this phase of the operation critical. Given the growing interest in employing CSP-MGTs for power generation, the previous review identifies four critical areas warranting attention concerning the transient analysis of CSP-MGTs during the start-up phase.

The transient operation of MGTs arises from two primary factors: load fluctuations and start-up/shutdown procedures. Load fluctuations can occur due to varying consumer power demand or the integration of intermittent solar energy sources. Existing literature predominantly focuses on solar-hybrid MGTs, where solar energy is backed up by an alternative source. However, investigations into transient performance and control strategies for solar-only MGTs are limited. In cases where heliostat fields are utilised, adjusting the received heat flux by moving mirrors and regulating air mass flow rate according to DNI have been explored. Conversely, when CSP dish technology is employed in solar-only MGTs, the optimal operating strategy is found to be Maximum Permissible Power (MPP) operation for each DNI by controlling the air mass flow rate, as the CSP dish lacks the capability to control the thermal power received at the solar receiver. The assessment of this control approach has so far only been conducted for the generation mode and within a steady-state operation. However, it is necessary to examine its performance within a transient framework and also under motoring mode conditions.

The start-up phase in CSP-MGTs is another crucial transient operation that may occur multiple times daily due to solar energy intermittency. This phase has predominantly been studied for fuelled or hybrid configurations, where fuel mass flow rate controls the system during start-up. Safety concerns in CSP-MGTs revolve around compressor surge and the thermal safety of the critical component, the solar receiver, which was also addressed in the OMSoP project. To ensure the MGT's safety during start-up, it becomes necessary to evaluate the system's transient behaviour. However, most studies on this matter pertain to large gas turbines and lack analyses specific to solar-only applications. Additionally, while start-up procedures are well-defined for fuelled MGTs, the start-up stages remain unspecified for CSP-MGT systems. Consequently, characterising the start-up procedure tailored to the CSP-MGT system is essential.

To conduct a comprehensive transient analysis of CSP-MGT start-ups, development of a transient model becomes imperative. The literature review highlights that an appropriate approach for developing such a model, suitable for real-time simulation, involves the use of a lumped volume approach. Additionally, to account for volume dynamics, the ICV methodology should be considered. Given the primary focus of this study on the start-up phase, it is essential to incorporate heat soakage into the transient model as well. Another critical aspect of simulating a full start-up is generating turbomachinery components' maps for the low-speed region, typically below 50% of the design speed. In this context, various novel methodologies which are introduced in the literature are applicable and they will be considered for implementation in this study.

The literature demonstrates that the start-up phase in MGTs significantly impacts costs, necessitating cost reduction measures. Within the literature, two key parameters targeted for minimisation are start-up time and start-up power requirements. However, optimising these parameters introduces a contradiction with MGTs' safety aspects concerning thermal safety and compressor surge, which requires careful consideration. Most studies in the literature focus on large gas turbines operating in combined cycles, where the entire system's thermal safety is linked to the components in the bottoming cycle. Consequently, an optimisation approach was adopted to identify the optimal start-up sequence in this context. Nonetheless, in the case of CSP-MGTs, the thermal safety of the solar receiver, a component within the MGT cycle, presents a challenge that conflicts with start-up time and related cost factors. Therefore, conducting an optimisation study to determine the optimal start-up schedule becomes necessary to strike a balance between cost efficiency and critical safety concerns specifically for CSP-

MGTs.

Chapter 3

Transient modelling of the CSP-MGT system

The review of existing research in the previous chapter emphasises the need to develop a transient model for a CSP-MGT as an energy system, in order to establish an efficient procedure for system start-up. This model should have the capability to analyse how the CSP-MGT system behaves dynamically during various transient operations, with a specific focus on the start-up process. Furthermore, it should be versatile enough to aid in the development and optimisation of control system performance, as well as in devising the sequence for the start-up phase. Thus, this chapter provides a comprehensive explanation of the detailed development of a transient model tailored specifically for a CSP-MGT system. The model's accuracy is validated through comparisons with available experimental data. While the developed model is capable of representing the transient behaviour of the CSP-MGT system across different operational modes, including generation and motoring modes, its primary aim is to investigate and enhance the start-up phase by optimising the system's input parameters during this crucial period.

3.1 General model description

The transient model of the CSP-MGT has been developed by using a lumped parameter approach to achieve high simulation speed for real-time applications for all components. Having a zero-dimensional volume for each component, the recuperator and solar receiver are exceptionally modelled by a one-dimensional approach which is discredited to segments that each segment is considered as a lumped volume. In order to take into account the mass imbalances in the cycle, a plenum is also added to the model after the compressor which is mainly attributed to the mass flow rate coming from the compressor and the mass flow rate going into the turbine. Since there is no such challenge after the turbine and the air is passed to the ambient after going through the recuperator, an extra plenum is not required or its effect is not significant. By using the lumped approach, the effects of the volumetric and thermal capacitance of the system components are considered. The conservation equations for mass, momentum and energy are solved fully or simplified for each component and are explained in detail later in this chapter. The transient model of CSP-MGT was developed in MATLAB/Simulink as a powerful tool for transient modelling and control systems. The developed model comprises three parts which are the thermodynamic model, the electrical system model and the control system model. These three parts are considered to be at the system level, shown in the layout of the model in Figure 3.1 in three colours of green, yellow and blue.

As it is observed in Figure 3.1, the first two parts are connected to each other with an interface that forms the mechanical model. The mechanical model belongs to the rotating shaft which deals with the mechanical and electrical torque as well as the torque resulting from mechanical losses and the rotational speed alteration. This interface is shown in the figure with green colour. The combination of the thermodynamic model and mechanical model is called the thermo-mechanical model and will be explained later in this chapter. Each model at the system level has one or more components at the sub-system (component) level which will be evaluated later as well.

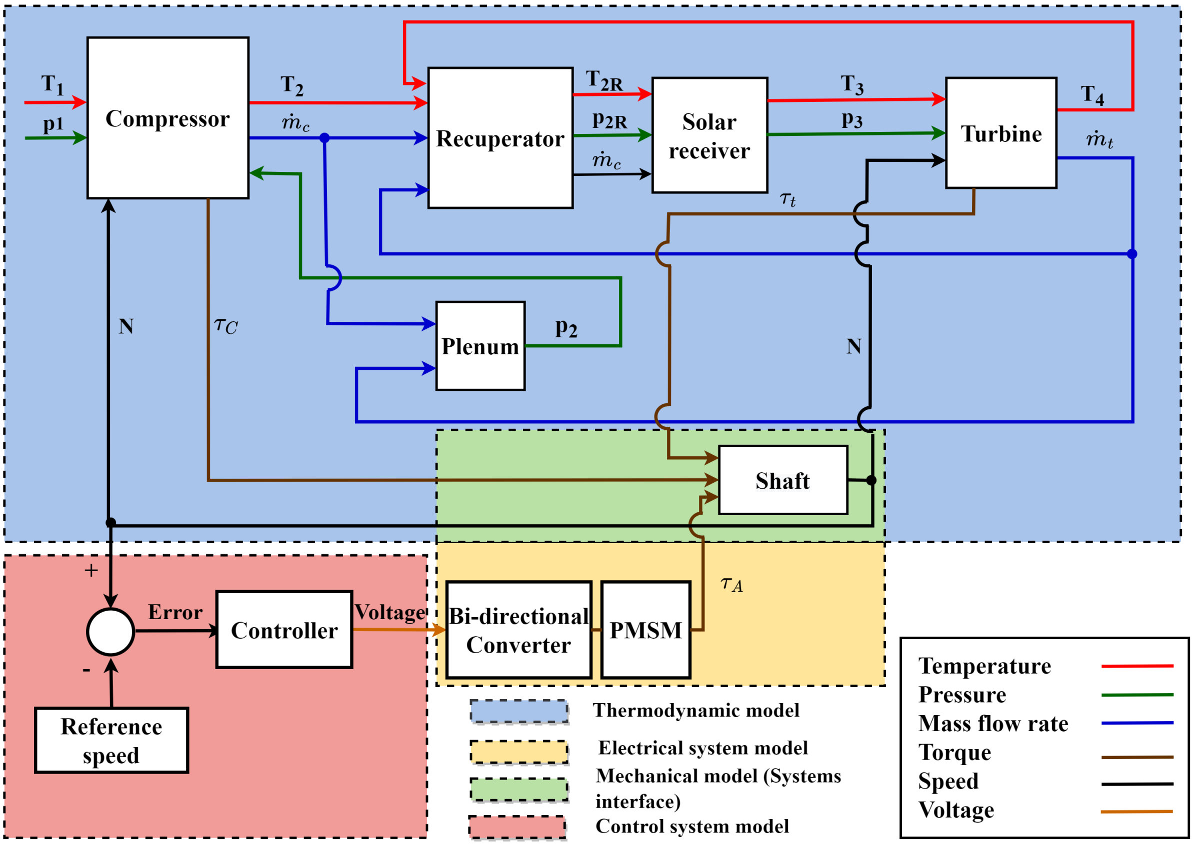

Figure 3.1: The layout of the developed model in MATLAB/Simulink.

3.2 Thermo-mechanical model

The main components of the thermo-mechanical model are a centrifugal compressor, radial turbine, recuperator, solar parabolic dish (which is not shown in the model layout in Figure 3.1), solar receiver, and shaft. Apart from these components, there is another added element that does not exist physically but is included in the model. This element which is called plenum is an artificial component that is attributed to the ICV method which has already been explained in Chapter 2. The addition of this component is for two reasons, firstly to consider the mass imbalances due to the existence of components with large volumes including the recuperator and solar receiver, and secondly to reduce additional computational costs related to compressor and turbine matching procedure through iterations in each time step. Furthermore, this component gives the ability to the system model to produce smoother operating line trajectories on turbomachinery performance maps during sharp transient behaviours. The operating condition of each component is determined either with a performance map or with appropriate conservation laws. In the cases where the effect of the transients on the component characteristics is negligible, steady-state performance maps are used. Otherwise, the corresponding differential equations are applied. For the current mathematical model, the performance maps are only used for turbomachinery components. However, differential equations are also included in the form of a series calculation placed after the performance map to take into account the heat soakage. The rest of the components' mathematical model includes relevant differential equations to consider the associated transient behaviours. The governing equations of each component are thoroughly explained in this section.

3.2.1 Turbomachinery components

The model of the compressor and turbine comprises two parts. The first part is a 0 dimensional volume where the operating point of the system in that component is found from predetermined characteristics. It is assumed that the influence of transients on the component characteristics can be neglected in this part; hence, steady-state maps are used[88] (Figure 3.2and 3.3). Additionally, since the fluid velocity inside these components is significantly higher than the shaft speed change rate, this control volume is assumed to be in thermodynamic equilibrium at every time step (quasi-steady-state mode). This calculation is followed by another part that considers thermal transients named heat soakage to include the effect of heat soakage on the compressor and turbine airflow temperatures with a lumped volume approach. This is because, when considering only steady-state simulation, the actual work of these components is calculated with no heat transfer between air and the component metal including casing and volute. Apart from that, it is difficult to define the efficiency of the compressor and turbine due to the heat soakage effect. Therefore, in order to use the isentropic efficiency and also consider the mentioned heat transfer, the model of the turbomachinery component is split into two segments to benefit from a serial calculation. Otherwise, it would have been difficult to calculate the compression and expansion efficiency with heat transfer in a single-segment model, [27].

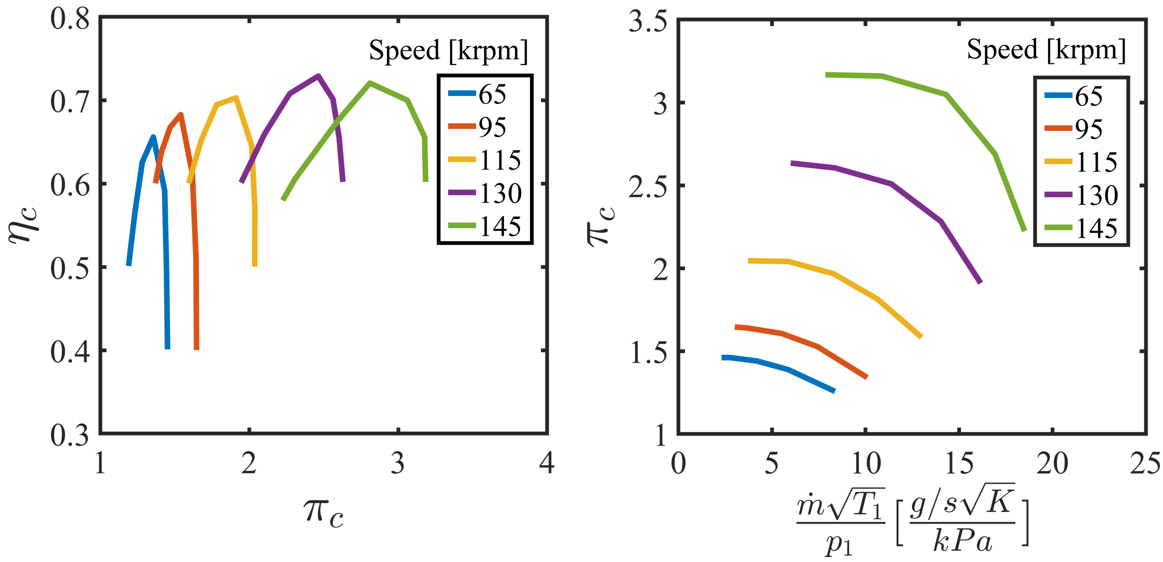

Figure 3.2: Compressor map of 6 [kW_e] MGT for speeds higher than 50% of the design speed [89].

Since the main focus of this study is on the start-up phase, it is required to have the performance map for low-speed values. Evaluation of the transients of the system performing from zero speed to higher values is difficult because the characteristic maps of a compressor and turbine are not usually available for speeds lower than 50 % of the rated speed. Thus, some extrapolation methods are generally used to predict compressor and turbine characteristics in low-speed regions. However, the possibility of generating physically invalid points in these methods is relatively high, as reported by [80]. Therefore, in this study, a method was used for map generation which includes interpolation instead of extrapolation. This was accomplished by introducing a zero speed point for the turbine and zero speed curve for compressor map [80] explained in detail in Appendix A. The resulting generated map was tuned with the existing

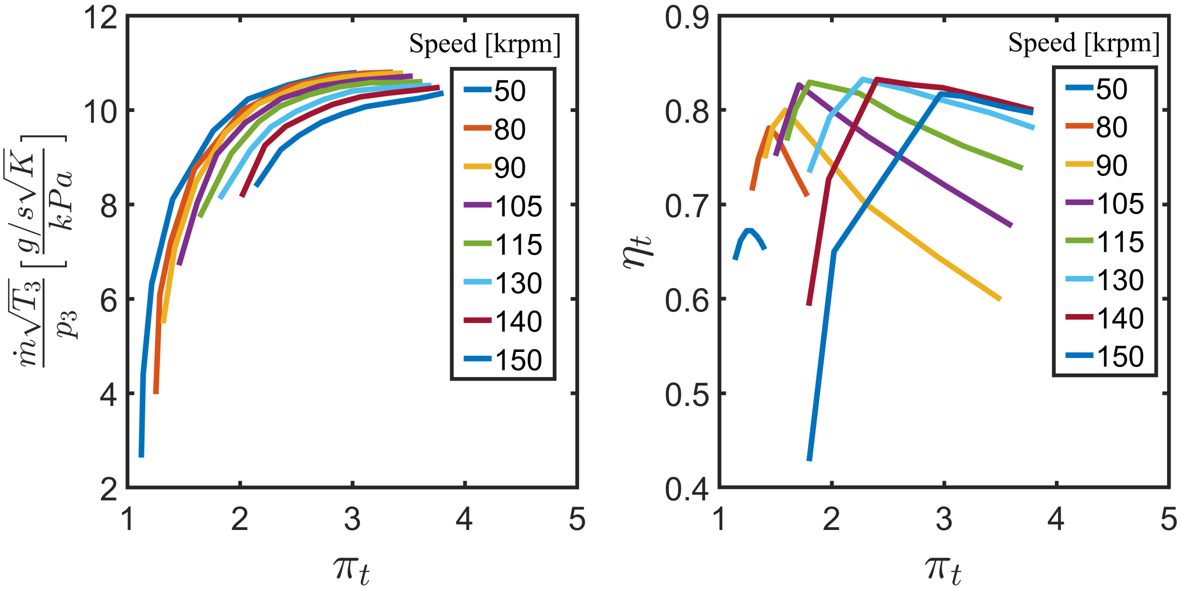

Figure 3.3: Turbine map of 6 [kW_e] MGT for speeds higher than 50% of the design speed [89].

experimental data associated with the tests of turbomachinery components conducted at City, University of London for 6 [kW_e] MGT [89].

Compressor

To determine the operating point of the MGT for the compressor, firstly, the characteristics of the inlet air are required. The operating fluid is assumed to be semi-ideal gas that follows ideal gas law rules. However, the physical characteristics of the gas are calculated with the help of polynomial functions of temperature [90]. The inlet air of the compressor is assumed to be in ambient conditions taken from the experimental measurements. Secondly, by using the shaft speed and compressor outlet pressure, modified speed and compressor pressure ratio are calculated and therefore, modified mass flow rate and isentropic efficiency of the compressor are found, Equation 3.1 to 3.4. Since the number of existing speed curves of the compressor map is limited, in case of having a rotational speed with a value other than the available ones, a new curve should be generated. The procedure of generating the new speed curve is based on linear interpolation [74]. The operating points on the new curve will also be defined according to the available points on the existing curves. Consequently, modified mass flow rate and isentropic efficiency associated with the given pressure ratio are found by interpolating between two operating points on the generated curve. The details of the interpolation procedure are explained in Appendix B.

$$\pi_c = \frac{p_2}{p_1} \tag{3.1}$$

$$N_{mf,c} = \frac{N}{\sqrt{T_1}} \tag{3.2}$$

$$\dot{m}_{mf,c} = f_1(N_{mf,c}, \pi_c) \tag{3.3}$$

$$\eta_c = f_2(N_{mf,c}, \pi_c) \tag{3.4}$$

where p, π, T, N, $\dot{m}$ and η are pressure, pressure ratio, temperature, shaft speed, air mass flow rate, and isentropic efficiency respectively. The subscripts of 1, 2, mf and c account for the compressor inlet, compressor outlet, a modified parameter and compressor. The functions of f_1 and f_2 are related to the compressor map curves. The modified mass flow rate is corrected again to find out the air mass flow rate.

$$\dot{m}_c = \frac{\dot{m}_{mf,c} p_1}{\sqrt{T_1}} \tag{3.5}$$

By using the isentropic efficiency, the steady-state outlet air temperature of the compressor is calculated.

$$T_{2,ss} = T_1 (1 + \frac{1}{\eta_c} [\pi_c^{\frac{\gamma - 1}{\gamma}} - 1]) \tag{3.6}$$

where $T_{2,ss}$ and γ are the steady-state compressor outlet air temperature and specific heat ratio which is the specific heat of the gas at a constant pressure to its specific heat at a constant volume. The power requirement of the compressor is calculated by the steady-state outlet air of the compressor.

$$PW_c = \dot{m}_c c_{p,c}(T_{2,ss} - T_1) \tag{3.7}$$

where PW_c and c_p are the required power by the compressor and specific heat.

During transient operations, especially start-up and shutdown, substantial heat transfer (both absorption and release) occurs between working fluid and metal due to the high-temperature differences, which has a significant impact on the performance of the MGT. Therefore, after the quasi-steady state calculations of the compressor, the outputs of the control volume are used for the heat soakage calculations, Figure 3.4.

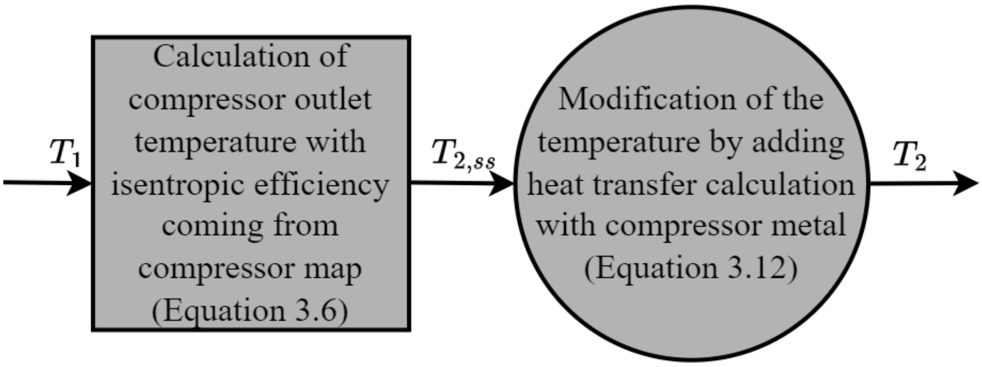

Figure 3.4: Modelling approach of the heat soakage in compressor (serial calculation).

To calculate the heat soakage, the shape information of the component, heat transfer area, mass of the metal, and heat transfer coefficient are required. Based on the lumped volume approach, the energy conservation equations related to the heat soakage in compressor metal are solved for an equivalent duct. Due to having access to the geometric information of the exerpimental setup from the OMSoP project, the heat transfer area and mass of the metal are found. In order to find the heat transfer coefficient, the Dittus-Boelter correlation for the Nusselt number is used [91]. Based on the lumped volume approach, it is assumed that the compressor metal has a uniform temperature distribution. The heat transfer between compressor metal and air as the working fluid is calculated as follows.

$$Q_{m,c} = U_c A_c (T_{a,c} - T_{m,c}) \tag{3.8}$$

$$Nu_c = 0.023 Re_c^{0.8} Pr_c^{0.33} \tag{3.9}$$

$$U_c = \frac{Nu_c k_{air}}{D_c} \tag{3.10}$$

where Q, U, A, Nu, Re, Pr, k_{air} and D_c are heat transfer rate, heat transfer coefficient, heat transfer area, Nusselt number, Reynolds number, Prantdl number, thermal conductivity of air and hydraulic diameter of the equivalent duct of the compressor and the subscripts of m,c and a,c refer to the mean-wall of the compressor and air as the compressor working fluid. The temperature of $T_{a,c}$ which is the inside air of the compressor is calculated by getting an average between the inlet and outlet temperature of the compressor ($T_1 + T_2/2$). This heat transfer rate leads to a change in compressor metal temperature that results in a different compressor outlet temperature than the steady-state outlet temperature. As it is shown in Equation 3.12, the heat transfer rate that is delivered to or taken from the compressor working fluid is the subtraction of the heat transfer rate from the required power of the compressor.

$$Q_{m,c} = M_c C_c \frac{dT_{m,c}}{dt} \tag{3.11}$$

$$T_2 = T_{2,ss} - \frac{PW_c - Q_{m,c}}{\dot{m}_c c_p} \tag{3.12}$$

where M_c and C_c are compressor metal mass and the specific heat capacity of compressor metal. It is worth mentioning that by implementing heat soakage, the power required for compression does not change due to the reason that the compressor metal consumes the thermal power that comes from the compressed air. This means that a portion of the required compression power is used for heat soakage. Therefore, as it was mentioned earlier, the power requirement of the compressor is calculated by the steady-state outlet air of the compressor.

Turbine

The modelling procedure of the turbine is similar to the compressor with a two-segment strategy, (Figure 3.5). For the first segment, by knowing TIT, rotational shaft speed, and turbine pressure ratio, the modified mass flow rate and the isentropic efficiency of the turbine are found as follow.

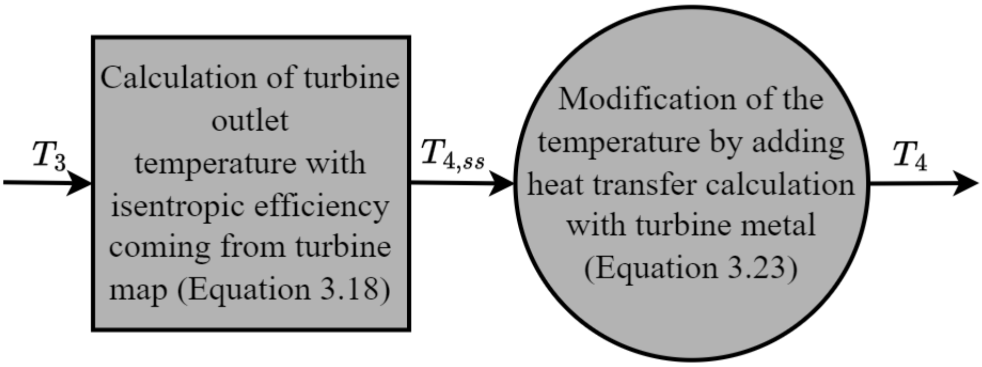

Figure 3.5: Modelling approach of heat soakage in the turbine (serial calculation).

$$\pi_t = \frac{p_3}{p_4} \tag{3.13}$$

$$N_{mf,t} = \frac{N}{\sqrt{T_3}} \tag{3.14}$$

$$\dot{m}_{mf,t} = g_1(N_{mf,t}, \pi_t) \tag{3.15}$$

$$\eta_t = g_2(N_{mf,t}, \pi_t) \tag{3.16}$$

where 3, 4, mf, and t subscripts account for the turbine, inlet air of the turbine, outlet air of the turbine and modified parameter of the turbine. The functions of g_1 and g_2 are related to the turbine map curves. The modified mass flow rate is then used to calculate the mass flow rate passing through the turbine.

$$\dot{m}_t = \frac{\dot{m}_{mf,t} p_3}{\sqrt{T_3}} \tag{3.17}$$

By using the isentropic efficiency of the turbine, the steady-state outlet temperature of the turbine is computed as follows.

$$T_{4,ss} = T_3(1 + \eta_t[(\frac{1}{\pi_t})^{\frac{\gamma-1}{\gamma}} - 1]) \tag{3.18}$$

where $T_{4,ss}$ is the steady-state turbine outlet air temperature. The outlet temperature of the turbine which was found out with Equation 3.18 is the temperature without considering thermal transient effects on the turbine metal. In order to take into account the heat soakage of the turbine, a series calculation like the compressor is implemented and the governing equations for the second segment of the turbine model are written below.

$$Q_{m,t} = U_t A_t (T_{a,t} - T_{m,t}) \tag{3.19}$$

$$Q_{m,t} = M_t C_t \frac{dT_{m,t}}{dt} \tag{3.20}$$

where $Q_{m,t}$ is the heat transfer rate between turbine metal and air and the subscripts of m,t and a,t refer to the mean-wall of the turbine and air as the turbine working fluid. The heat transfer coefficient (U_t) of the second segment (equivalent volume of the turbine associated with the lumped volume approach) is found with the same correlation that was used for the compressor. The temperature of $T_{a,t}$ which is the air inside the turbine is calculated by getting an average between the inlet and outlet temperature of the turbine ($T_3 + T_4/2$). The generated power of the turbine in case of not considering the heat soakage ($PW_{t,ss}$) is calculated as follows.

$$PW_{t,ss} = \dot{m}_t c_{p,t} (T_3 - T_{4,ss}) \tag{3.21}$$

Consequently, the final generated power that includes heat soakage is found with the help of the below equation.

$$PW_t = PW_{t,ss} - Q_{m,t} \tag{3.22}$$

This means that the generated power of the turbine considering the heat soakage is less than the case where no heat transfer is taken into account. The outlet temperature of the turbine is therefore calculated by using the actual generated power.

$$T_4 = T_3 - \frac{PW_t}{\dot{m}_t c_{p,t}} \tag{3.23}$$

where T_4 is the turbine outlet temperature by considering the heat soakage.

3.2.2 Recuperator

Recuperator thermal model

Many of the recuperators that function as heat exchangers have undisclosed geometry. This situation also exists in this study since the recuperator used in the experimental setup was exclusively designed for solar-powered micro gas turbines. Given that plate-fin and counter-flow compact heat exchangers are commonly utilised in micro gas turbines [67], it was decided to employ a heat exchanger with performance characteristics similar to the MGT of this study. Thus, a plate-fin heat exchanger employed in [92] was chosen for this purpose. However, for the modelling purpose, the recuperator was simplified into a counter-flow heat exchanger and divided into discrete unit volumes using a 1-D approach, employing a lumped volume approximation for each unit of the model. The 1-D finite difference approach, with the recuperator volume divided into multiple cells, is depicted in Figure 3.6. This approach offers an advantage over the 0-D approach since assuming a uniform wall temperature for the recuperator wall can lead to numerical issues and instabilities during transient operations. This concern is particularly evident in compact heat exchangers with steep temperature gradients [93].

Energy conservation is applied for each cell of the recuperator wall with Equation 3.24in

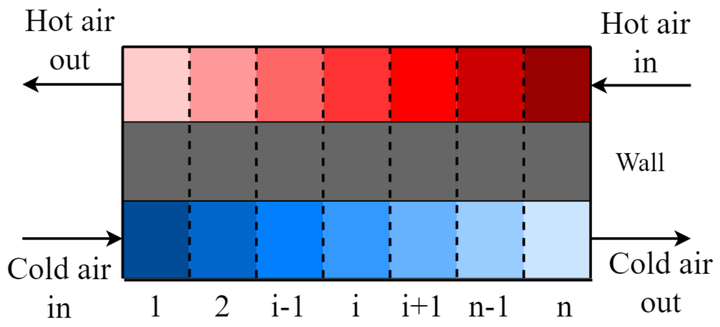

Figure 3.6: Thermal modelling approach of the recuperator.

transient form. However, the energy conservation for each fluid cell in both cold and hot sides is solved in steady-state mode due to the lower thermal inertia of the air in comparison with the recuperator metal which leads to faster transients in the airflow (Equation 3.25 and 3.26). This is a valid assumption, especially for recuperators with effectiveness higher than 75% [74]. This implies that the rate at which the airflow temperature changes, happens much faster compared to the rate at which the metal temperature of the recuperator changes. As depicted in Equation 3.24, the temperature fluctuations of the recuperator's metal within a single cell are impacted by the difference between the heat transferred from the hot fluid and the heat assimilated by the cold fluid.

$$\frac{M_{recu}C_{recu}}{n}\frac{dT_i^{m,recu}}{dt} = \dot{m}_{hot}c_{p,hot}(T_i^{hot} - T_{i+1}{}^{hot}) - \dot{m}_{cold}c_{p,cold}(T_{i+1}{}^{cold} - T_i^{cold}) \tag{3.24}$$

where M_{recu}, C_{recu}, $\dot{m}_{hot}$, $\dot{m}_{cold}$, $c_{p,hot}$ and $c_{p,cold}$ are recuperator wall mass, recuperator wall specific heat capacity, hot and cold side air mass flow rates, and hot and cold side air specific heat capacity. The temperatures of $T_i^{m,recu}$, T_i^{hot} and T_i^{cold} are mean wall temperature of the recuperator metal, hot side and cold side air temperature for cell number of i. The parameter of n refers to the number of cells and the subscript of i accounts for the particular cell number.

Furthermore, since there is not a differential equation provided for the airflow within the recuperator, the heat responsible for changing the temperature of the air from the inlet to the outlet is the same as the heat exchanged between the recuperator wall and the flowing air as mentioned earlier, which can be expressed using Equations 3.25 and 3.26.

$$\dot{m}_{hot}c_{p,hot}(T_i^{hot} - T_{i+1}{}^{hot}) = \frac{U_{hot}A_{hot}}{n}(\frac{T_i^{hot} + T_{i+1}{}^{hot}}{2} - T_i^{m,recu}) \tag{3.25}$$

$$\dot{m}_{cold}c_{p,cold}(T_{i+1}{}^{cold} - T_i^{cold}) = \frac{U_{cold}A_{cold}}{n}(T_i^{m,recu} - \frac{T_i^{cold} + T_{i+1}{}^{cold}}{2}) \tag{3.26}$$

where U_{hot} and U_{cold}, A_{hot} and A_{cold} represent the heat transfer coefficient and heat transfer area for the hot and cold side, respectively. This computation includes the disparity between the average wall temperature of the recuperator at cell index i and the average temperature of the incoming and outgoing airflow, denoted by subscripts i and $i+1$. The heat transfer areas and coefficients of the hot and cold sides are determined using the geometric details of the heat exchanger, as described in the subsequent paragraphs.

In this research, the employed plate-fin heat exchanger is an offset strip fin heat exchanger, recognised as among the most commonly adopted improved fin configurations. This configuration is illustrated in Figure 3.7.

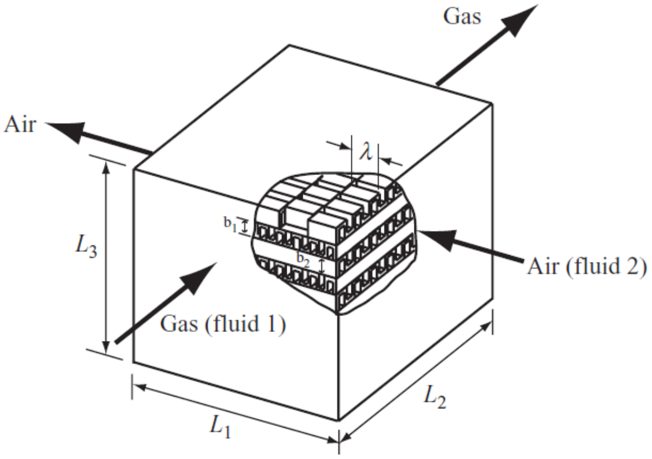

Figure 3.7: Plate-fin heat exchanger, employing offset strip fin [94].

The idealised fin geometry is also shown in Figure 3.8. Based on this figure, the total heat transfer area for each fluid side consists of the primary area and the fin area. The primary area consists of the plate area except for the fin base area, multi-passage side walls, and multi-passage front and back walls. Usually, the number of passages for the hot fluid side and the cold fluid side are N_p and N_p+1. The number of passages is obtained by using below equation. The parameters of this equation are shown in Figure 3.8.

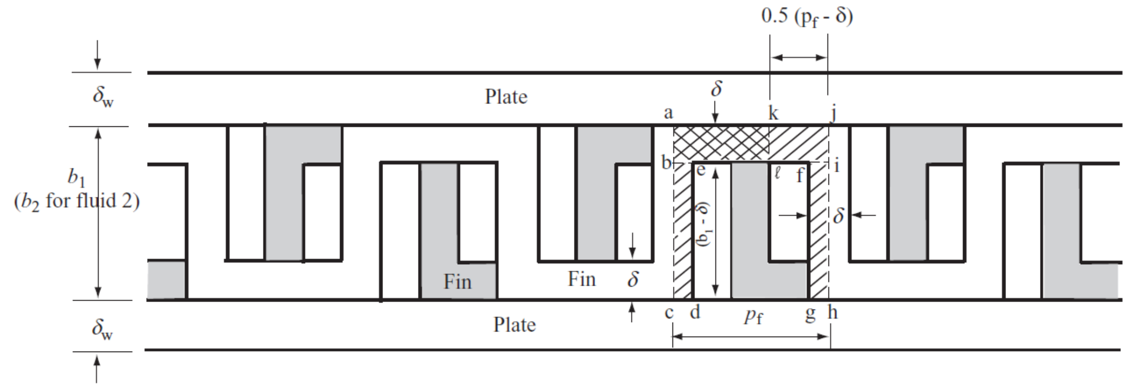

Figure 3.8: Schematic of offset strip fin geometry [94].

$$N_p = \frac{L_3 - b_2 - 2\delta_w}{b_1 + b_2 + 2\delta_w} \tag{3.27}$$

The number of the passages refers to the number based on one flow passage between the two plates, not all the individual channels between the plates. The total number of fins for fluid 1 (hot) and fluid 2 (cold) is calculated as follows.

$$n_{f1} = \frac{L_1}{p_{f1}} N_p \tag{3.28}$$

$$n_{f2} = \frac{L_2}{p_{f2}} (N_p + 1) \tag{3.29}$$

where p_f is the fin pitch. The total number of fins n_{f1} is shown in Figure 3.8 (the hatched area of a-c-d-e-f-g-h-j-a) counting as a unit fin. Since total primary area is equal to ’total plate areas’ – ’fin base areas’ + ’passage side wall areas’ + ’passage front and back wall areas’, the primary area for fluid 1 is found as follows with the terms written in the same order.

$$A_{p1} = 2L_1L_2N_p - 2\delta L_2 n_{f1} + 2b_1L_2N_p + 2(b_2 + 2\delta_w)L_1(N_p + 1) \tag{3.30}$$

The number of offset strip fins per the number of fins is calculated as below.

$$n_{off1} = \frac{L_1}{\lambda_2} \tag{3.31}$$

$$n_{off2} = \frac{L_2}{\lambda_1} \tag{3.32}$$

where λ_1 and λ_2 are the offset strip fin length for fluids 1 and 2. The total fin area A_{f1} consists of the fin area and offset-strip edge areas.

$$A_{f1} = 2(b_1 - \delta)L_2 n_{f1} + 2(b_1 - \delta)\delta n_{off1} n_{f1} + (p_{f1} - \delta)\delta(n_{off1} - 1)n_{f1} + 2p_{f1}\delta n_{f1} \tag{3.33}$$

By having the primary and fin area, the total heat transfer area, A_{t1} is calculated which is the sum of the two values. The total area for fluid 2 is also calculated with similar equations.

$$A_{t1} = A_{p1} + A_{f1} \tag{3.34}$$

The heat transfer coefficient is found by the below equation which is shown for fluid 1 developed by Manglik and Bergles [95].

$$U_1 = \frac{j_1 G_1 cp_1}{Pr_1^{2/3}} \tag{3.35}$$

where j and G are Colburn number and fluid mass velocity based on the minimum free-flow area ($\dot{m}/A_c$) where A_c for fluid 1 is found as follows.

$$A_{c1} = (b_1 - \delta)(p_{f1} - \delta)n_{f1} \tag{3.36}$$

And Colburn factor is calculated by the most comprehensive correlations applicable for laminar, transition, and turbulent flows [95].

$$\begin{aligned} j = 0.6522Re^{-0.5403}(\frac{p_f-\delta}{b-\delta})^{-0.1541}(\frac{\delta}{\lambda})^{0.1499}(\frac{\delta}{p_f-\delta})^{-0.0678} \\ \times (1+5.269\times 10^{-5}Re^{1.34}(\frac{p_f-\delta}{b-\delta})^{0.504}(\frac{\delta}{\lambda})^{0.456}(\frac{\delta}{p_f-\delta})^{-1.055})^{0.1} \end{aligned} \tag{3.37}$$

in which Re is Reynolds number and it is calculated for fluid 1 as follows.

$$Re_1 = \frac{G_1 D_{h1}}{\mu} \tag{3.38}$$

where D_{h1} is the hydraulic diameter of fluid 1 and it is found by using free-flow area (cross-section area) and total heat transfer area.

$$D_{h1} = \frac{4A_{c1}L_2}{A_{t1}} \tag{3.39}$$

Recuperator pressure drop model

The structural and geometrical parameters of the component are also necessary to calculate the air outlet pressure of the recuperator on both hot and cold sides. By having the geometry from [92], the pressure drop for a plate-fin heat exchanger on both sides is found with Equation 3.40.

$$\Delta p_{recu} = \frac{4fLG^2}{2D_h}\frac{1}{\rho_m} \tag{3.40}$$

where f, L, D_h and ρ_m are the fanning friction factor, airflow length on one side of the heat exchanger, hydraulic diameter, and the average of inlet and outlet fluid density, respectively. The term of $(1/\rho)_m$ is calculated by $(1/\rho_{in} + 1/\rho_{out})$ where ρ_{in} and ρ_{out} refer to the inlet and outlet air of one side of the recuperator. The friction factor can be found by the below correlation.

$$
\begin{aligned}
f = 9.6243 Re^{-0.7422} (\frac{p_f - \delta}{b - \delta})^{-0.1856} (\frac{\delta}{\lambda})^{0.3053} (\frac{\delta}{p_f - \delta})^{-0.2659} \\
\times (1 + 7.669 \times 10^{-8} Re^{4.429} (\frac{p_f - \delta}{b - \delta})^{0.92} (\frac{\delta}{\lambda})^{3.767} (\frac{\delta}{p_f - \delta})^{0.236})^{0.1}
\end{aligned}
\tag{3.41}
$$

3.2.3 Concentrated solar power dish and solar receiver

Solar parabolic dish

The solar parabolic dish is made up of two concentric mirror crowns that focus sunlight onto the solar receiver at the focal point of the paraboloid. Based on the role of the solar parabolic dish, the power entering the solar receiver determines how efficiently the dish is concentrating the sun rays to a focal point. Therefore, the optical efficiency (η_{opt}) is defined as the ratio between the thermal power entering the receiver window and the power intercepted on the mirror surface. This efficiency will be used in finding the received thermal power in the solar receiver.

Solar receiver thermal model

The solar receiver is also considered to be a heat exchanger similar to the recuperator. The only difference is that the geometry of the solar receiver is mostly known. The solar receiver that was used in this study was taken from the demonstration plant of OMSoP and it was an impinging cavity receiver, Figure 3.9. Impinging cavity receivers have a different performance strategy compared with common cavity receivers. In this type of receiver, a jet impingement technology is introduced to the typical cavity receiver for efficiently taking the heat from the absorber and managing the heat flux peak on the absorber surface [96]. The conventional cavity receivers were mainly designed based on the forced convection heat transfer which led to having significant temperature peak in the receiver designs [97].

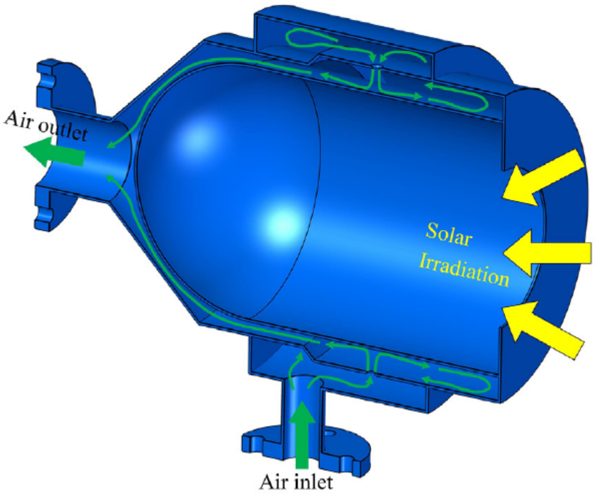

Figure 3.9: Geometry of the impinging cavity receiver [98]

Due to the existence of an impinging jet which results in an efficient heat transfer from the receiver wall to the fluid, the distribution of the heat transfer coefficient as well as temperature on the wall could not be assumed to be uniform [99] and it is preferred to model the receiver with a one-dimensional approach rather than a zero-dimensional approach. This means that the temperature of each cell is uniform on the perimeter of the cavity receiver which supports the one-dimensional approach. The schematic of the receiver along with the one-dimensional approach of the receiver is shown in Figure 3.10.

As it can be observed from Figure 3.10, the fluid path shown with green arrows and the receiver/absorber wall shown with red line in the lower schematic of the figure, are divided into n number of cells. The first cell that is shown with a blue square in the lower schematic, is the cell that includes the stagnation point resulting from the impinging jet. The stagnation point in the impinging jet is where high-velocity fluid impacts a surface, creating zero velocity and an increased pressure zone. The rest of the cells (from cell number 2 to n) are arranged based on the flow path towards the air outlet. Consequently, following the initial cell, the discretised

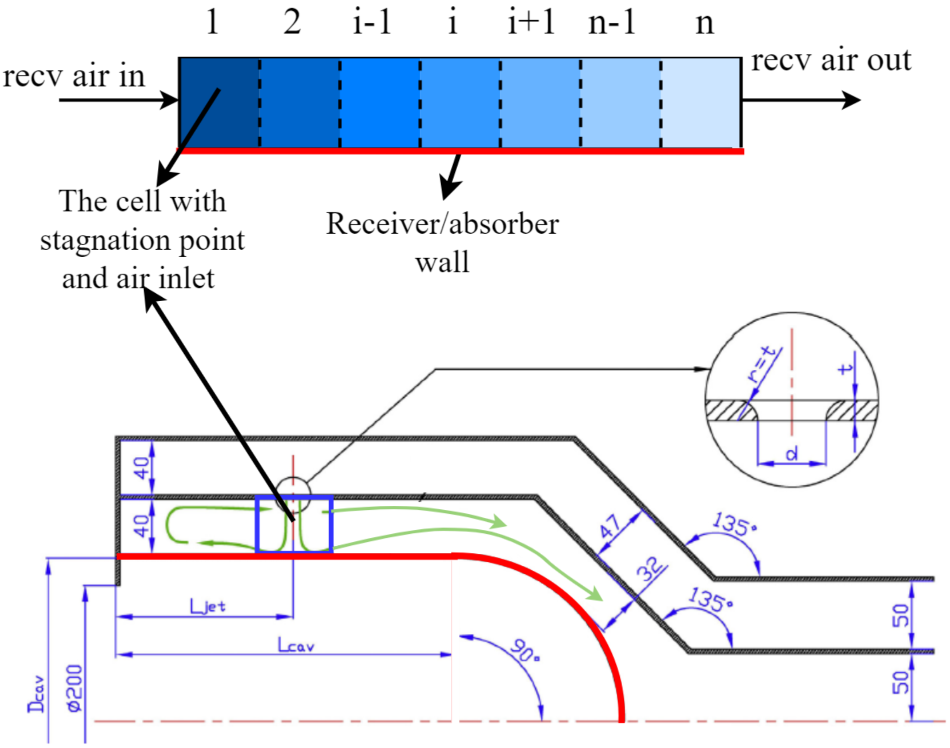

Figure 3.10: Thermal modelling approach of the solar receiver.

cells originating from the jet's left side are positioned. Subsequently, the flow on the jet's right side is discretised, and the resultant cells are positioned after the previously arranged ones. Every cell functions as a lumped volume in which conservation equations are resolved. These equations have exclusively been addressed for energy considerations and solely for the receiver's metal. This exclusion of the fluid is attributed to the fluid's notably lower thermal inertia. The governing equation for a single cell is expressed as follows.

$$\frac{1}{n}Q_{in}-\frac{1}{n}Q_{loss}-Q_{abs,i}=\frac{1}{n}M_{recv}C_{recv}\frac{dT_{m,recv,i}}{dt} \tag{3.42}$$

where the subscripts of in, $loss$, abs,i, $recv$ and $m,recv$ refer to the input heat to the solar receiver, heat loss, absorbed heat by the air inside the ith cell, receiver and mean-wall of the receiver. All of the heat transfer rates of Equation 3.42 are explained below.

1. Input heat to the solar receiver

The intercepted heat on the cavity receiver wall is calculated based on the below equation. As it was mentioned before, optical efficiency is the main parameter that defines what portion of the heat arrives at the receiver window.

$$Q_{in} = DNIA_{eff}\eta_{opt} \tag{3.43}$$

where A_{eff} and ηopt are the effective area and the optical efficiency of the solar parabolic dish.

2. Heat loss to the ambient

Heat loss of the solar receiver mainly accounts for two main losses: Convection and radiation heat loss which are calculated with the below equations.

$$Q_{loss} = Q_{conv,loss} + Q_{rad,loss} \tag{3.44}$$

$$Q_{conv,loss} = U_{conv,loss}A_{recv}(T_{m,recv} - T_{amb}) \tag{3.45}$$

$$Q_{rad,loss} = U_{rad,loss}A_{recv}(T_{m,recv} - T_{amb}) \tag{3.46}$$

where the subscripts of $conv, loss$, $rad, loss$, amb, $m, recv$ refer to convection loss, radiation loss, ambient condition and mean-wall of the receiver. The heat transfer coefficients are calculated based on the below equations referred to [100].

$$Nu_{rad} = 0.000154Gr^{0.627}(2 + cos(\phi))^{-1.054}(1 + \varepsilon)^{0.0313}AR^{1.638} \tag{3.47}$$

$$Nu_{conv} = 0.00106Gr^{0.149}2 + cos(\phi)^{7}.228(1 + \varepsilon)^{-0.0849}AR^{1.466} \tag{3.48}$$

where Nu, Gr, ϕ, ε and AR are the Nusselt number, Grashof number, tilt angle of the cavity receiver, the emissivity of the inner wall of the cavity and aperture ratio, respectively. Aperture ratio is a dimensionless parameter defined as the ratio of the aperture diameter to the inner diameter of the cavity. Grashof number is calculated as follows.

$$Gr = \frac{L_s g \beta (T_{m,recv,i} - T_{amb})}{\nu_{air}} \tag{3.49}$$

in which L_s, g, β and ν are the characteristic length, gravitational acceleration, thermal expansion coefficient and kinematic viscosity of the air at ambient temperature, respectively. The characteristic length is computed as follows.

$$L_s = \Sigma a_i cos(\phi + \psi_i)^{b_i} L_i \tag{3.50}$$

where the constants of a_i, b_i and ψ_i are summarised in Table 3.1.

i	a_i	b_i	(ψ_i)
1	4.08	5.41	-0.11
2	-1.17	7.17	-0.30
3	0.07	1.99	-0.08

Table 3.1: Constants of Equation 3.50 for calculation of the cavity length scale [100].

By computing the Nusselt number for convection and radiation loss, the heat transfer coefficients can be found below.

$$U_{conv,loss} = \frac{k_{amb} Nu_{conv}}{L_s} \tag{3.51}$$

$$U_{rad,loss} = \frac{k_{amb} Nu_{rad}}{L_s} \tag{3.52}$$

where k_{amb} is the thermal conductivity of the air at ambient conditions.

3. Absorbed heat by air

The absorbed heat by the air for each cell is attributed to the heat transfer coefficient and the heat transfer area between the air and the absorber wall in that specific cell.

$$Q_{abs,i} = U_{abs,i}A_{recv}(T_{m,recv,i} - \frac{T_{recv,in,i} + T_{recv,out,i}}{2}) \tag{3.53}$$

in which the subscripts of abs, i, $recv, in, i$ and $recv, out, i$ refer to absorbed heat by air in the ith cell, receiver inlet and outlet air associated with the ith cell.

Since the solar receiver is equipped with an impinging jet, the heat transfer coefficient in each cell is calculated differently depending on the distance from the stagnation point. The local heat transfer coefficient for the cells that are affected by the impinging jet, is calculated as follows [101].

$$Nu_x = 0.055{Re_{st}}^{0.75}Pr^{0.42}e^{-0.025(x/d)^2} \quad 0 \leq x/d \leq 8 \tag{3.54}$$

$$U_x = \frac{Nu_x k_{air}}{d} \tag{3.55}$$

$$Re_{st} = \frac{4\dot{m}}{\mu n_{nozzle}\pi d} \tag{3.56}$$

where x, d, k_{air} and n_{nozzle} are the distance from the stagnation point, nozzle diameter, air thermal conductivity and the number of nozzles on the receiver. The subscripts of x and st are referred to as the distance from the stagnation point to represent the local parameter and stagnation point. This equation is only valid for a limited distance from the stagnation point. For the cells, where x/d is higher than the value of 8, the heat transfer coefficient is calculated with the help of the Dittus-Boelter Nusselt empirical correlation [91].

$$Nu = 0.023Re^{0.8}Pr^{0.33} \tag{3.57}$$

Solar receiver pressure drop model

Since the solar receiver is an impinging cavity receiver, the main pressure drop in the receiver is attributed to the jet impingement on the absorber wall. Therefore, it is reasonable to compute the pressure drop by computing the maximum existing pressure drop [98] which was validated in [99].

$$\Delta p_{recv} = \frac{\rho {V_{jet}}^2}{2{C_d}^2} \tag{3.58}$$

in which ρ, C_d are jet air density, discharge coefficient and V_{jet} is the air jet velocity that calculated as follows.

$$V_{jet} = \frac{4\dot{m}}{n_{nozzle}\pi\rho d^2} \tag{3.59}$$

where n_{nozzle}, d is the total nozzle number in the receiver geometry and the diameter of the nozzle exit hole.

3.2.4 Plenum: Artificial component

The plenum is an artificial component that has been added to the thermodynamic model to take into account mass imbalances which is implemented by solving the mass conservation equation. This means that the outlet pressure of the compressor and the inlet pressure of the recuperator and the solar receiver does not change instantaneously in each time step. The outlet mass flow rate of the compressor and the inlet mass flow rate of the turbine have a difference due to the large volumes of the recuperator and solar receiver in each time step. This causes the discharge pressure of the compressor to undergo a time delay from one off-design point to another. To account for this effect, an equation is formulated to describe the change in compressor outlet pressure, taking into account the change rates in pressure associated with the inlet and outlet mass flow rates. The values of these mass flow rates are determined using the compressor and turbine performance maps, as discussed earlier.

$$\frac{dp_2}{dt} = \frac{RT_2}{V_{plenum}}(\dot{m}_c - \dot{m}_t) \tag{3.60}$$

where R and V_{plenum} represent the gas constant and the plenum volume, respectively. The plenum volume is a combination of the air side volumes of the cold side of the recuperator and solar receiver.

3.2.5 Shaft

The shaft is the component that represents the mechanical model of the system. As previously stated, the mechanical model of the CSP-MGT serves as a bridge connecting the thermodynamic model and the electrical model. It undergoes four main sources of torque: Compressor, turbine, PMSM and loss torque. Therefore, by writing the energy conservation for the MGT shaft, the differential equation of the shaft will become as follows.

$$\tau_t - \tau_c - \tau_A - \tau_{loss} = J\frac{d\omega}{dt} \tag{3.61}$$

where τ, ω and J are torque, rotational speed and shaft inertia, and the subscripts of t, c, A, $loss$ refer to the turbine, compressor, high-speed alternator (PMSM) and mechanical loss. This must be noted that ω is the rotational shaft speed in rad/s and the torques are in $N.m$. Compressor and turbine torques for each time step are calculated as follows.

$$\tau_c = \frac{PW_c}{\omega} \tag{3.62}$$

$$\tau_t = \frac{PW_t}{\omega} \tag{3.63}$$

The torque loss is linked to the power reduction caused by the presence of bearings along the shaft. The power loss of the shaft called mechanical loss is calculated as follows for one bearing [75] that will be multiplied by the number of bearings on the shaft.

$$PW_{loss} = 4.87 \times 10^{-15} D^{3.95} N^{1.75} \mu_{oil}^{0.4} + 3.19 \times 10^{-10} N D \dot{m}_{oil} \tag{3.64}$$

where D, μ_{oil} and $\dot{m}_{oil}$ are pitch circle diameter of the bearing, oil viscosity and oil mass flow rate. The value of the oil mass flow rate is assumed to be constant in this study. By dividing the power loss over rotational speed, the torque loss is calculated.

3.3 Electrical model

The electrical part of the CSP-MGT system has the duty of transforming the mechanical power generated by the MGT to electrical power or the other way around. The former is associated with the generation mode and the latter is for the motoring mode which happens during the start-up and shutdown phases. Since the main aim of the current study is the motoring mode, the electrical model is mainly explained for the start-up phase. The electrical system of CSP-MGT is comprised of three main components which are PMSM as the high-speed alternator, grid-side (or load-side) and PMSM-side bi-directional converter, Figure 3.11. The two bi-directional converters could operate in both AC/DC and DC/AC transformations. This leads to the capability of the system to operate in both motoring and generation modes. In the case of motoring mode, the three-phase current is taken from the grid with a frequency of 50 Hz and a voltage of 400 V. Since the required current of the PMSM is within a higher frequency and the voltage is also varying with time, the grid-side converter transforms the three-phase alternating current (AC) to direct current (DC). Afterwards, the PMSM-side converter produces a new three-phase AC current with the required voltage and frequency which will be delivered to the PMSM. The PMSM then generates the required torque to alter the speed of the shaft to the requested value. However, this must be noted that this arrangement is for the case of a grid-connected system. If the CSP-MGT operates in the off-grid mode, the power source could be a battery that provides a DC current. This means that there is no need for two converters during the motoring mode and only one converter during start-up is required to provide AC current for the PMSM. Nevertheless, during the generation mode, depending on the consumer which could require either AC or DC electric current, the second bi-directional converter can be used.

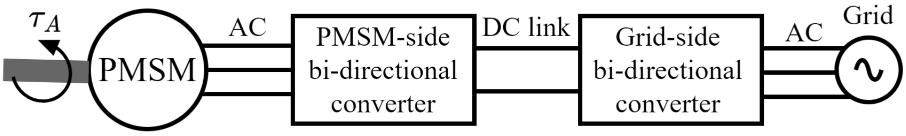

Figure 3.11: Schematic of the electrical system components and their arrangement in the motoring mode (grid-connected).

3.3.1 Permanent magnet synchronous machine (PMSM)

In a PMSM, the rotor contains permanent magnets that create a fixed magnetic field. The stator, which surrounds the rotor, consists of windings that carry AC current. As the electric current flows through the stator windings, a rotating magnetic field is created. This rotating magnetic field interacts with the fixed magnetic field of the permanent magnets, causing the rotor to rotate. The control of a PMSM can be challenging due to its three-phase AC current and the complexity of regulating speed in such a system. To simplify the control process, three-phase variables are transformed into a two-dimensional coordinate system (d-q frame) using two DC values. This approach is advantageous because the control of DC current is more convenient and it is extensively studied in classical linear control theory [102]. This methodology is called Park-Clark transformation. The mathematical model of the PMSM written with DC transformed current and voltage parameters are shown in the below Equations. The equations represented by 3.65 and 3.66 originate from the constituent terms of the stator voltage, specifically the voltage drop across the stator resistors and the induced voltage resulting from the varying magnetic flux. The derivative of the current in both equations relates to the induced voltage term. Additionally, in Equation 3.65, ϕ_{mg} denotes the magnitude of the flux generated by the rotor's permanent magnets, which is also derived from the induced voltage term in the original equation. This must be noted that the transformed DC current does not exist physically and it is only used for mathematical calculations.

$$\frac{dI_q}{dt} = \frac{1}{L_q}[V_q - R_s I_q - L_d \omega_e I_d - \phi_{mg} \omega_e] \tag{3.65}$$

$$\frac{dI_d}{dt} = \frac{1}{L_q}[V_d - R_s I_d + L_q \omega_e I_q] \tag{3.66}$$

$$\tau_A = \frac{2Z_P}{3}[\phi_{mg} I_q + (L_q - L_d) I_q I_d] \tag{3.67}$$

where I_q,I_d, V_q, V_d, R_s, L_q, L_d, ϕ_{mg}, ω_e, τ_A and Z_p are q-axis current, d-axis current, q-axis voltage, d-axis voltage, the resistance of PMSM stator, q-axis inductance, d-axis inductance, flux induced by the permanent magnets of the rotor, electromagnetic speed, electromagnetic torque and pole pairs of the PMSM. The electromagnetic speed is calculated as follows.

$$\omega_e = \omega_m Z_p / 2. \tag{3.68}$$

The model of the PMSM which is used in this study however does not include the dynamics of the PMSM current, and it is assumed that the two terms of dI_q/dt and $dI_d dt$ are equal to zero. This is a reasonable assumption since the dynamic of the electric current is 1000 times faster than the dynamics of the shaft based on the experimental data. Therefore, by removing the dynamic terms from the above equations (3.65-3.67), the equations for finding RMS (root mean square) voltage, RMS current and the required power of the PMSM become as follows. As I_d component does not produce torque it is usually controlled to be 0 [102]. It is worth noting that the RMS value is the effective value of a varying voltage or current. It is the equivalent steady DC value which gives the same effect of the associated AC current. The RMS value of a quantity is the square root of the mean value of the squared values of the quantity taken over an interval.

$$I_q = \frac{2}{3Z_p}\frac{\tau_A}{\phi_{mg}} \tag{3.69}$$

$$I_d = 0 \tag{3.70}$$

$$V_d = -L\omega_e I_q \tag{3.71}$$

$$V_q = R_s I_q + \phi_{mg}\omega_e \tag{3.72}$$

$$I_{RMS} = \sqrt{I_q^2 + I_d^2} \tag{3.73}$$

$$V_{RMS} = \sqrt{V_q^2 + V_d^2} \tag{3.74}$$

$$PW_A = \omega_m \tau_A \tag{3.75}$$

It must be noted that the calculated value for electric power, is the one that is provided by PMSM for the MGT during the start-up phase. However, the power source required to provide the required power for PMSM has a higher value. This power is found by adding up PMSM power losses to the previously calculated electric power. PMSM has different losses such as copper, iron and windage losses [103]. The copper loss is mainly due to the existing resistance of the wires of the PMSM which have been already included in the calculated voltage. The other losses such as iron and windage losses are calculated using a coefficient that was found by experimental measurements in the previous study [8]. Therefore, the required electric power source to provide the feeding voltage to the PMSM is calculated as follows, Equation 3.76.

$$PW_e = \frac{3}{2}V_q I_q + K_{HSA}N \tag{3.76}$$

in which PW_e and K_{HSA} are the electric power required for the PMSM and HSA multiplier for PMSM losses excluding the copper loss.

3.3.2 Bi-directional converter

The bi-directional converter is placed before PMSM where the DC current is transformed to a three-phase AC to be fed to PMSM. This component is composed of a number of insulated-gate bipolar transistors (IGBTs) as switches. The converters are used for AC/DC, DC/AC electric current transforming and controlling the voltage by feeding and modulating the current with the help of Pulse width modulation (PWM). This technique involves generating a series of pulses where the width of each pulse is adjusted to achieve the desired average voltage, effectively simulating a continuous analogue voltage [102]. IGBT converters usually have six IGBTs for three-phase currents which were also adopted for this study. The power loss of the whole component is calculated by computing power loss in each IGBT multiplied by the number of these elements [104]. The power loss in one IGBT is comprised of two types of losses which are conduction and switching loss [105]. By finding the power loss, the power that is required to be fed to the bi-directional converter is calculated.

$$PW_{cvt} = PW_e + PW_{cvt,loss} \tag{3.77}$$

where cvt refers to the bi-directional converter and PW_{cvt} is the power of the current to be fed to the converter. The power loss of the converter, denoted as $PW_{cvt,loss}$, consists of two components that will be elaborated upon.

IGBT conduction power loss

During the on-state condition when the current through IGBT is not zero, IGBT is equivalent to two components connected in series which are a resistor and a DC voltage source. Figure 3.12 shows the equivalent circuit of a conducting IGBT. The power losses in both resistor and DC voltage source contribute to the IGBT conduction power losses. The DC voltage $V_{0,I}$ is the zero current voltage of IGBT, which can be obtained from the IGBT current and voltage characteristic plot that could be found in the datasheet [106]. The procedure for finding the resistance shown in Figure 3.12 is explained in Appendix D.

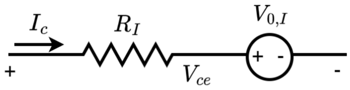

Figure 3.12: Equivalent circuit of an IGBT for on-state condition [104].

Based on the equivalent circuit shown in the figure, the conduction power loss is calculated by Equation 3.78.

$$PW_{cond} = {I_{RMS}}^2.R_I + V_{0,I}.I_{avg} \tag{3.78}$$

where R_I is the resistance of the IGBT on collector-emitter current (on-state resistance) and I_{avg} is the average current that is calculated by using RMS current ($I_{avg} = 2.\sqrt{2}.I_{RMS}/\pi$). The subscript of *cond* stands for conduction loss.

IGBT switching power loss

Since IGBTs are switching devices, some of the energy is lost during switching on and off. The values for E_{on} and E_{off} which are the energy loss for switching on and off respectively, are provided by the manufacturer in the datasheet for IGBT energy losses in specific test conditions. However, most of the operating conditions are different from the test conditions with different voltage and current. According to [107], E_{on} and E_{off} are proportional to the current through IGBT in on-state conditions and voltage in off-state conditions. Therefore, on-state current and off-state voltage are adopted from the datasheet as references and the actual energy losses are estimated based on Equations 3.79 and 3.80 [104].

$$E_{on,I} = \frac{V_{ce}}{V_{ce,ref}} \cdot \frac{I_c}{I_{c,ref}} . E_{on,ref} \tag{3.79}$$

$$E_{off,I} = \frac{V_{ce}}{V_{ce,ref}} \cdot \frac{I_c}{I_{c,ref}} . E_{off,ref} \tag{3.80}$$

where the subscripts of ce, c and ref account for collector-emitter, collector and reference value respectively.

The calculated energy is for a duty cycle of PWM. The duty cycle is expressed as a percentage and represents the fraction of time that the signal is "on" or in the high state compared to the total period. In order to find out the power loss of the switching devices, the calculated energies should be multiplied by the frequency of the switching. The value of switching frequency which is significantly higher than the frequency of the electric current, is provided in the next sections.

$$PW_{sw} = (E_{on,I} + E_{off,I}) \cdot f_{sw} \tag{3.81}$$

where PW_{sw} and f_{sw} are the switching loss and switching frequency.

3.4 Control system

The control strategy for CSP-MGT does not involve adjusting the specific fuel flow rate like fuelled MGTs. Since the input thermal power in these systems is intermittent and beyond control, an alternative parameter is used for the CSP-MGT control system. Based on the previous study on CSP-MGT [8], the electric voltage was identified as the optimal parameter for controlling the operation of the system. As the controlled parameter is the shaft speed, a PI controller was chosen over a PID controller due to the rapid changes in shaft speed that could introduce noise caused by the derivative term in the control equations. The PI controller requires two design coefficients, namely the proportional gain (k_p) and integral gain (k_I), which need to be determined for controller design. To find these coefficients, it is necessary to derive the system's transfer function. The implementation of the controller on the system is depicted in Figure 3.13, illustrating the closed-loop configuration.

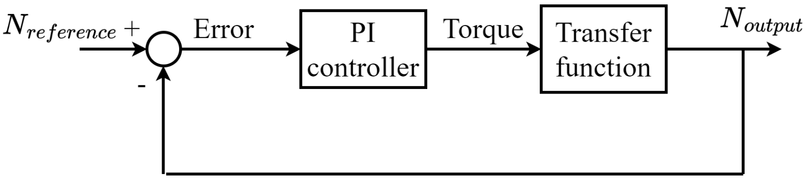

Figure 3.13: Closed loop of the system with a controller.

In order to derive the transfer function of the entire system, it is necessary to extract the governing equations. In Figure 3.13, the controlled parameter is the speed, while the torque value serves as the controlling parameter. This is due to the reason that in this study, the dynamics of the current and voltage were not taken into account, resulting in the exclusion of their dynamic equations. However, in reality, the controlling parameter should be the PMSM voltage, as mentioned earlier. As a result, a steady-state model was adopted for voltage and current calculations, and they are not incorporated into the transfer function. Consequently, the torque parameter was used as the controlling parameter instead of voltage.

The CSP-MGT system has six main transient sources: Compressor and turbine heat soakage, recuperator and solar receive heat soakage, mass imbalances and shaft speed. Since speed is the direct corresponding state variable with respect to the control system and the rest of the state variables are already included in the torque calculations, the differential equation of the shaft speed (3.61) is the only equation that is used for the transfer function where the difference between turbine torque and compressor torque and τ_A is named τ_g and torque loss could be estimated as a linear function of shaft speed ($B\omega$ where B value is found from Equation 3.64 by considering the first term of this equation negligible. By getting a Laplace transformation of Equation 3.61, the equations will be in the frequency domain.

$$J s \omega = \tau_t - \tau_c - \tau_A - B\omega \tag{3.82}$$

$$\tau_t - \tau_c - \tau_A = \tau_g \tag{3.83}$$

$$\frac{\omega}{\tau_g} = \frac{1}{Js + B} \tag{3.84}$$

The PI controller function in the frequency domain is as follows.

$$k_p + \frac{k_I}{s} \tag{3.85}$$

Therefore, the closed-loop becomes as follows.

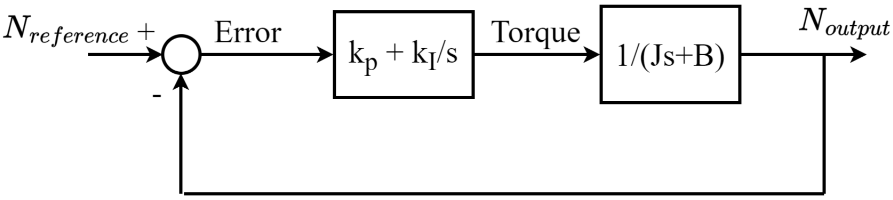

Figure 3.14: Closed-loop of the system with the transfer function and PI controller

As it can be observed from Figure 3.14, the open-loop function of the system is $1/Js+B$. Based on the general form of the function of a first-order system which is $C/1+\tau s$ (where C is a constant value and τ is the time constant), it can be deduced that $\tau = B/J$.

By using the closed-loop system shown in Figure 3.14, the whole system transfer function with the controller can be written as below.

$$\frac{Output}{Input} = \frac{k_p s + k_I}{Js^2 + (k_p + B)s + k_I} \tag{3.86}$$

With the help of the standard form of the second-order equations which has a denominator of $s^2 + 2\zeta\omega_n s + (\omega_n)^2$, the two coefficients of the PI controller are found. The values for the PI controller coefficients are provided in the next sections.

3.5 Simulation process

In this study, the focus is on simulating the off-grid operation of the CSP-MGT during the start-up phase, which means that it operates independently without relying on the national grid. Therefore, during the system's start-up phase, it is assumed that a battery is used as the power source, providing DC electrical current. As depicted in Figure 3.15, the calculated electric power at each time step represents the power that needs to be supplied to the bi-directional converter located before the PMSM. The transient model of the CSP-MGT system was developed based on the ICV methodology to include mass imbalances during the transient operation as mentioned earlier in this chapter. The transient model of the whole CSP-MGT system includes a set of ordinary differential equations which are coming from the model of each subsystem. There is one equation for the compressor, one for the turbine, five for the recuperator, seven for the solar receiver, one for the shaft and one for the plenum. Figure 3.15 shows a flowchart of the simulation procedure of the transient model.

The flowchart depicts the transient model, highlighting the five main state variables: $T_{m,c}$, $T_{m,t}$, $T_{m,recu}$, $T_{m,recv}$, p_2, N. Among these, $T_{m,recu}$ and $T_{m,recv}$ are composite variables with five and seven temperatures respectively, as they represent the one-dimensional model of the recuperator and solar receiver. The initial values of these state variables depend on the system's initial conditions, which are determined by the start-up type (cold or warm start-up, explained in Chapter 4). The model receives two sets of inputs: ambient conditions and PMSM voltage. The PMSM voltage originates from the bi-directional converter, which receives it from a power source that was assumed to be a battery. The voltage value is determined by the controller, as illustrated in the flowchart. Once the initial conditions and inputs are set, the simulation begins. The calculations commence from the compressor and proceed according to the flowchart's

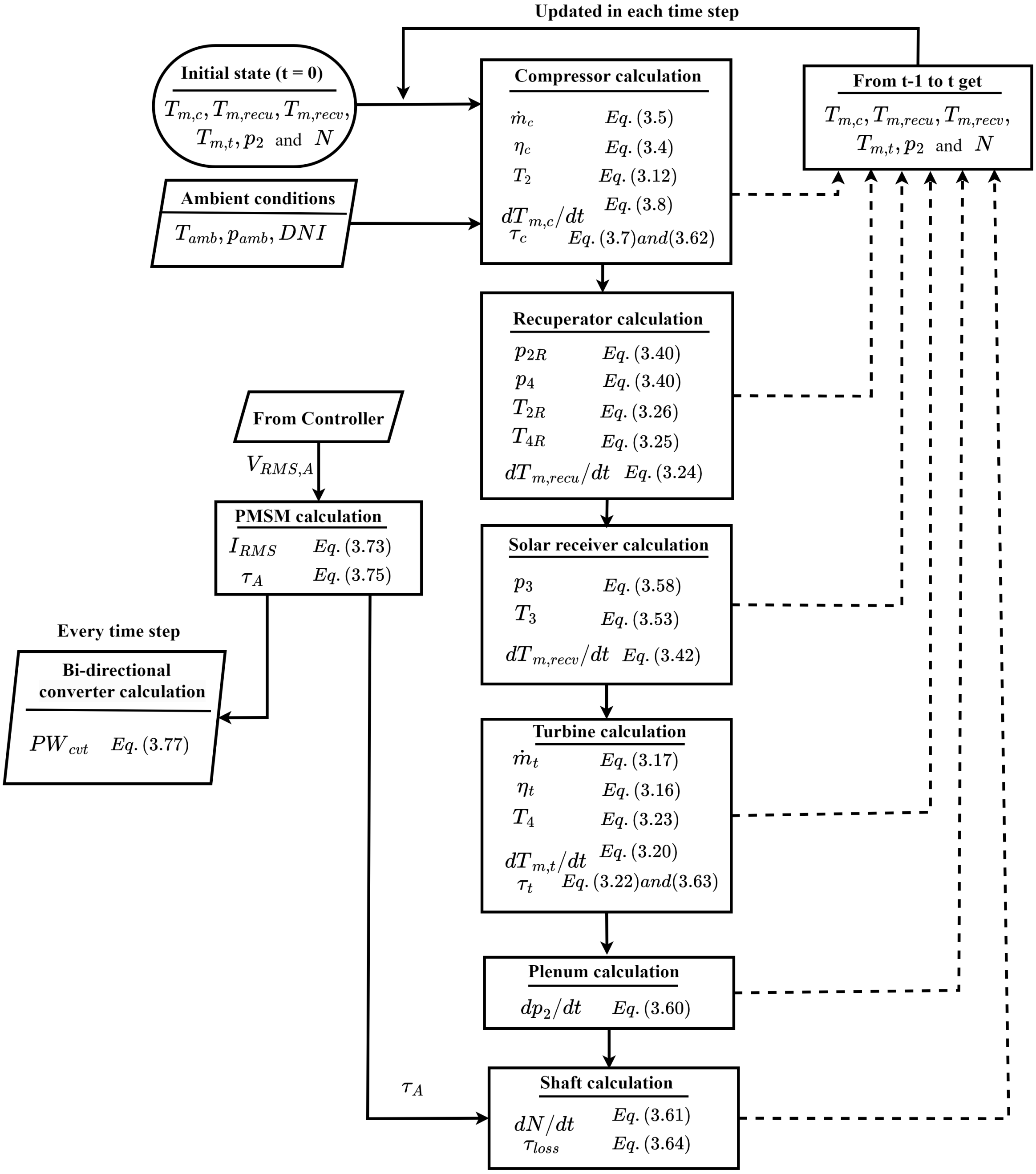

Figure 3.15: The flowchart of the transient model of the CSP-MGT system.

sequence. At each time step, the six sets of state variables are updated based on the calculations of each model component. These updates are represented by dashed lines in the flowchart. To determine the new value of the N state variable, the required torque by the compressor (τ_c), the generated torque by the turbine (τ_t), and the mechanical torque loss (τ_{loss}) are added to the torque from the PMSM (τ_A). Subsequently, by solving the differential equation, the new value of the state variable of N is obtained. The speed feedback signal is then fed into the controller, which generates the required PMSM voltage to produce the τ_A torque. This step, although not explicitly shown in the flowchart, has been previously illustrated in Figure 3.1 at the beginning of this chapter.

3.6 Validation of the model

In order to evaluate the efficacy of the model results, it is necessary to compare the outputs of the model with experimental measurements. This process is typically accomplished through validation and verification, which occur in two distinct stages in this study. The first stage involves the validation of individual components against available experimental data, with a focus on analysing their transient behaviour. In the second stage, the results of the whole model of CSP-MGT are also compared against experimental measurements. The second stage is crucial for understanding the transient effects of the components on each other. The necessary experimental data were obtained from experimental tests conducted on the CSP-MGT demonstration plant from the OMSoP project. The plant was installed at ENEA (Italian National Agency for new technologies, energy and sustainable economic development) Casaccia site, near Rome which was commissioned in the winter of 2017. The measurements were only obtained for the motoring mode of the system and there are no available data for the generation mode. The data have been provided by the City, University of London as one of the OMSoP project partners. A number of tests have been conducted on the plant that all of them have been analysed to select the most suitable ones for the validation of the developed model. Some of the tests have been carried out while the CSP dish was out of focus. These cold tests were performed to verify the full operability of the different system apparatuses: mechanical/electrical/control and confirm the pre-calculated critical MGT speed range [29]. Therefore, the on-sun tests where the parabolic dish was focused to have the thermal input power, were chosen for the validation procedure.

3.6.1 Turbomachinery components

As previously mentioned, the low-speed curves of the turbomachinery components' performance map are generated by interpolating between existing curves and using a zero-speed line and point for the compressor and turbine, respectively. However, since the map is generated based on a mathematical approach, it needs to be calibrated using available experimental data. Each speed curve includes multiple operating points with varying pressure ratios and modified mass flow rates. Ideally, multiple measurements corresponding to each speed curve would be needed to accurately calibrate the generated curves. However, in most cases, including this study, only one operating point per speed curve is available. For the calibration of the generated speed curves, experimental data from City, University of London are utilised. These data are obtained from tests conducted on a 6 $[kW_e]$ MGT at the university laboratory. It should be noted that the MGT was originally designed to operate at the design point, not at low speeds. Consequently, the relative uncertainty of the measurements for operating points at lower speeds is higher compared to operating points closer to the design conditions.

Tuning the generated map

To adjust the generated map at lower speeds according to the measured data, two types of errors must be considered: relative uncertainty and standard deviation. Relative uncertainty is associated with the measurement tools and is based on a study conducted by City, University of London [89]. On the other hand, standard deviation represents the variation of the measured parameter around its mean value, as shown in the two plots for pressure ratio and modified mass flow rate at a modified speed of 2283,3.16 (one of several available modified speeds).

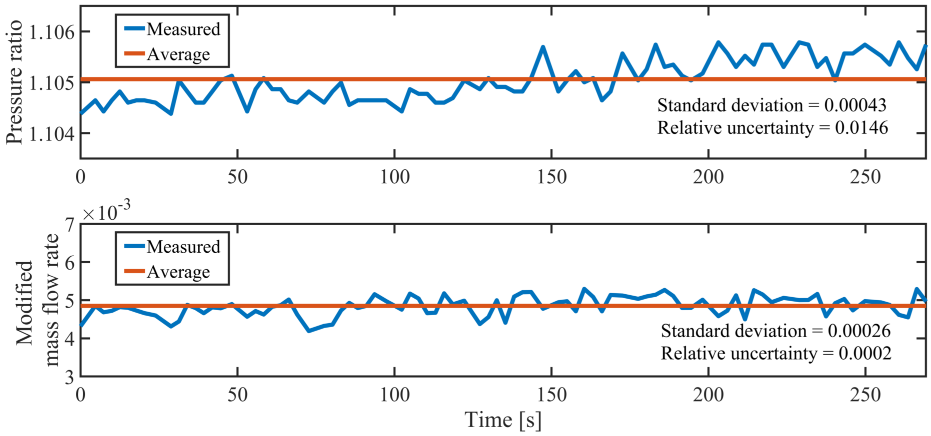

Figure 3.16: Representation of two types of errors for the modified mass flow rate and pressure ratio in the modified speed value of 2283.

As shown in Figure 3.16, both types of errors mentioned earlier, namely the errors in pressure ratio and modified mass flow rate, are observed. To tune the generated map accurately, the larger of the two errors is chosen as the relative error for the experimental operating point. This approach ensures that the generated speed curves are properly calibrated. To adjust the generated map, the position of the speed lines was modified slightly, while maintaining their shape, until they matched the measured data. The tuning results for the compressor and turbine maps can be seen in Figures 3.17 and 3.18, respectively.

Once it has been validated that the generated performance map accurately represents the actual steady-state operating points for the low-speed region, it is necessary to confirm the validity of the interpolation methodology for all operating ranges of the performance map. The validation of the operating points found through interpolation from performance maps is typically achieved by comparing them to steady-state off-design experimental data. The measured data for the mass flow rate are used to validate the generated performance map related to the

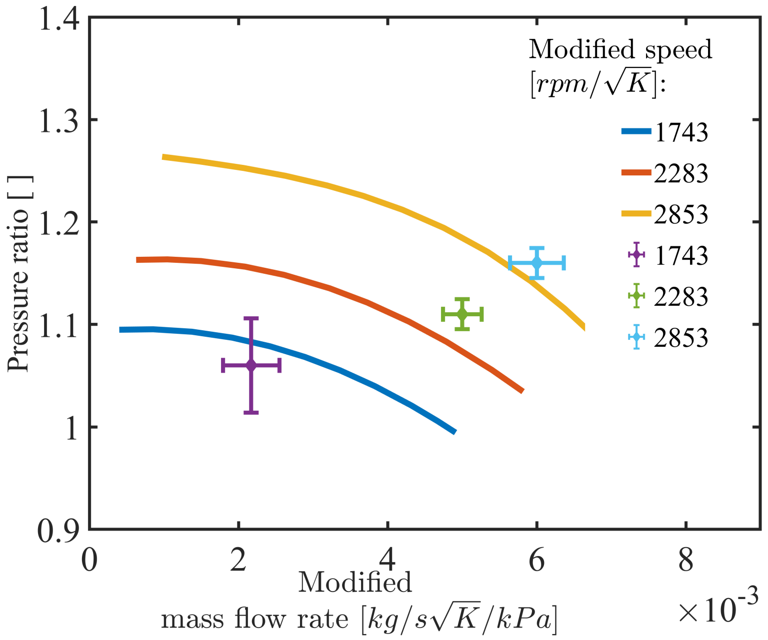

Figure 3.17: Tuning the generated map for the low-speed curves of the compressor with the measured data.

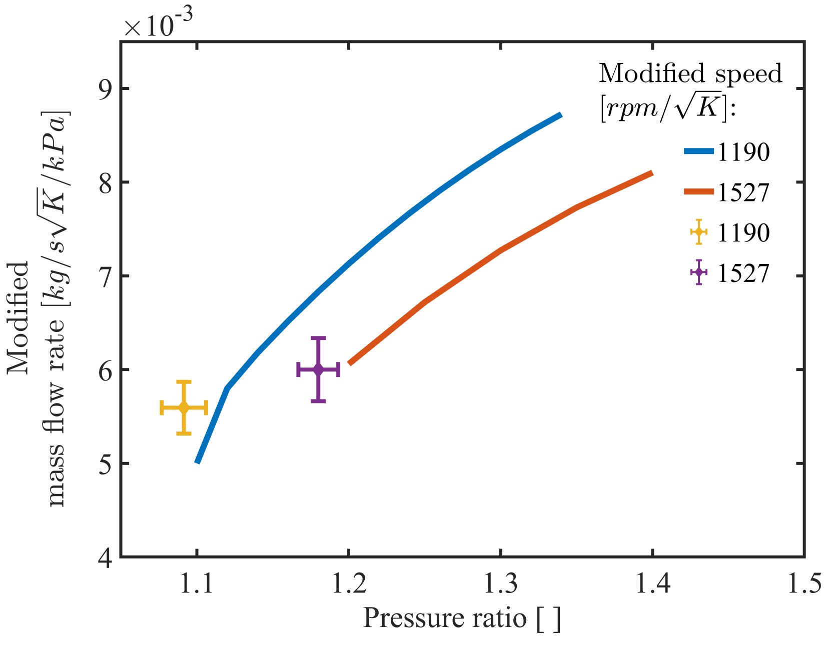

Figure 3.18: Tuning the generated map for the low-speed curves of the turbine with the measured data.

modified mass flow rate. To validate the generated curves of isentropic efficiency, the model output for the outlet temperature of the turbomachinery component was compared with the measurements. For this purpose, the performance map of the Turbec T100PH Series as reported by the German Aerospace Center (DLR) was utilised [108]. The validation results are shown in Table 3.2. Since the experimental data were only available for the compressor, the validation was only done for the compressor which is also applicable for the turbine. The parameters of validations were chosen to be the air mass flow rate and the steady-state compressor outlet temperature.

Parameter	Relative error
Compressor air mass flow rate $[kg/s]$	< 6 %
Compressor outlet temperature $[K]$	< 3.2 %

Table 3.2: The validation of the model of the turbomachinery components for steady-state values.

As it is illustrated in Table 3.2, the maximum error is about 6% which is an acceptable error for this study.

The transient model of the compressor and turbine was also simulated for the two cases of with and without heat soakage in the whole CSP-MGT system validation procedure (will be explained later in this chapter). The results indicate a notable enhancement in predicting TIT and TOT in the simulation of the whole system of CSP-MGT by approximately 20-30% closer to the measurements when heat soakage is included. This substantial improvement clearly demonstrates the positive impact of incorporating heat soakage. This shows that in spite of the compact volume geometry of turbo-machinery components, the significant temperature differentials experienced during start-up can lead to substantial heat transfers.

3.6.2 Recuperator

The initial validation of the recuperator focused on the Colburn and friction factors, utilising experimental data. This validation process was applied to a plate-fin heat exchanger with dimensions of 1/10-27.03 as detailed in a study by [92], with the geometric specifications sourced from Kays and London’s work [109].

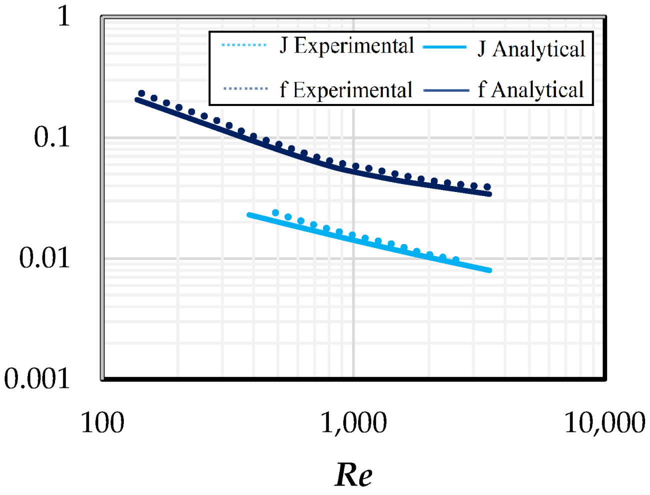

Figure 3.19: Variation of Colburn and friction factors with Reynolds number [110]

This result ensures that the heat transfer coefficients used in the energy conservation equation and the friction factor used in calculating the pressure drop are in agreement with experimental data. Additionally, another validation has been done from the thermal point of view for the outlet temperatures of the recuperator. Therefore, a layout was defined for the recuperator, shown in Figure 3.20. The inputs of the model layout are cold and hot side air temperature and air mass flow rate taken from measurements. The outputs which are the cold and hot side outlet air temperatures will be compared with their experimental counterparts.

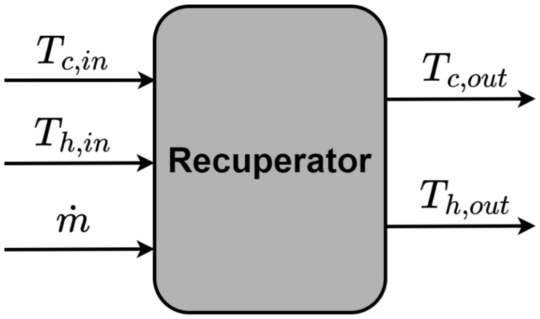

Figure 3.20: The layout of the recuperator component for the thermal model.

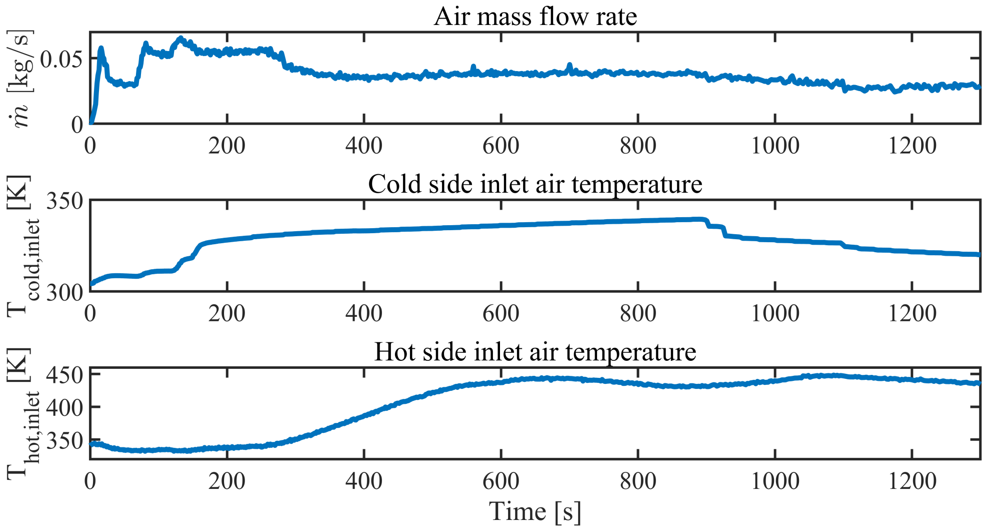

Figure 3.21: The inputs of the recuperator thermal model for validation.

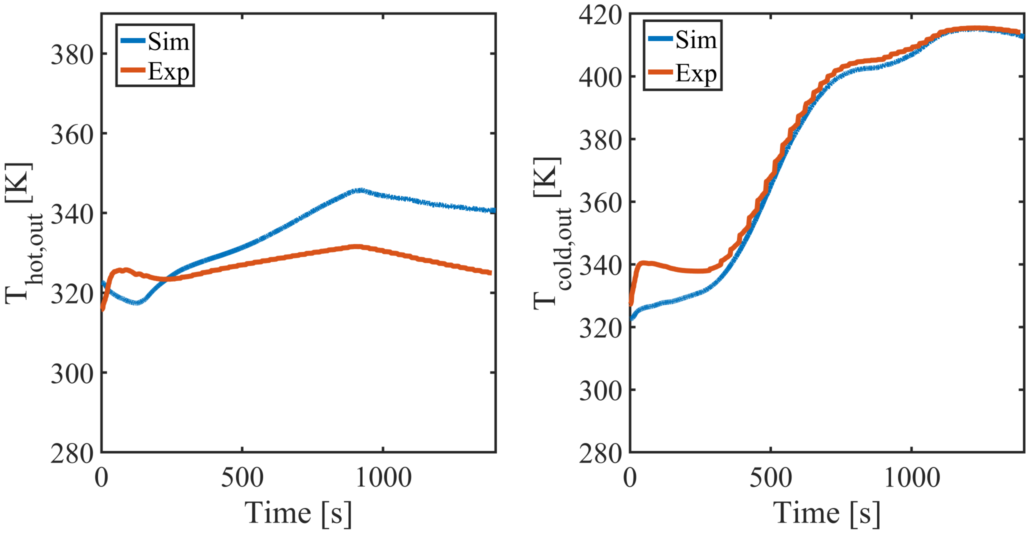

Figure 3.22: Validation results of the recuperator thermal model.

Based on the obtained results, it can be seen that the maximum deviation of hot and cold side outlet air temperatures from their corresponding experimental values are 4.6% and 4.7%, respectively. Furthermore, the trend of the temperature variations was also captured with an acceptable level of accuracy. Nevertheless, at the initial stage of the outlet temperature, a distinct pattern deviating from the experimental measurement is evident. This deviation can be attributed to the sudden increase in the air mass flow rate, which may be influenced by potential measurement uncertainties associated with low values of mass flow rate. Additional factors could be linked to inaccuracies in the model caused by the lack of precise information about the initial temperature of the recuperator metal during the experiment.

3.6.3 Solar receiver

The approach for validating the thermal model of the solar receiver is similar to that of the recuperator. Therefore, the same strategy was used for this component. The layout of the thermal model of the solar receiver is shown in Figure 3.23.

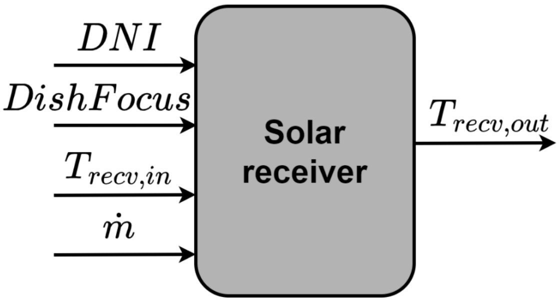

Figure 3.23: The layout of the thermal model of solar receiver component in the transient model.

The thermal model of the solar receiver has four main inputs: DNI, Dishfocus schedule, receiver inlet air temperature ($T_{recv,in}$) and mass flow rate ($\dot{m}$). The Dishfocus is a schedule that determines the periods when the CSP dish is either focused or not focused. It is worth mentioning that, during the experimental test, the dish was intentionally not maintained in a focused state for an extended duration to avoid excessive heating of the turbine bearings. The Dishfocus schedule is established using two parameters: sun azimuth angle and dish azimuth angle. When these two angles are identical, it indicates that the dish is directed towards the sun and thus in a focused position.

In this study, the Dishfocus schedule establishes that when the difference between the sun and dish azimuth angles exceeds 20 degrees, the dish is deemed to be out of focus, and no thermal power is directed towards the dish's focal point. As the angle difference reduces below 20 degrees, the focusing process initiates, and the input thermal energy progressively increases until the dish aligns with the sun azimuth angle. Once this alignment is achieved, the dish is considered fully focused. It is important to note that the specific threshold value for the angle difference may vary depending on the characteristics of the CSP dish and the requirements of the solar receiver under investigation. The specific value of 20 degrees was originally established in the OMSoP project and is being applied here accordingly. The receiver model's inputs are illustrated in Figures 3.24 and 3.25.

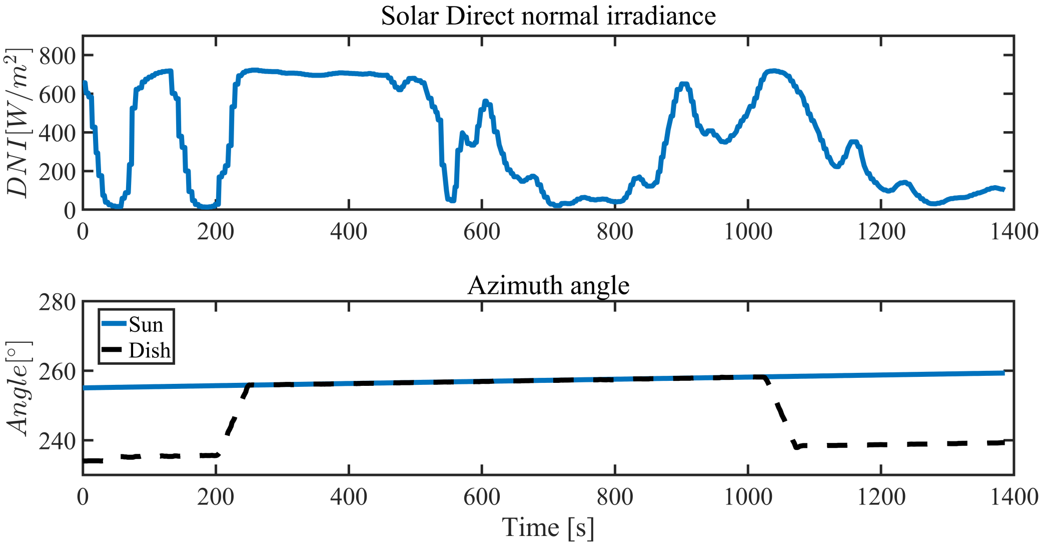

Figure 3.24: DNI and Dish focusing schedule for the receiver thermal model.

Using the inputs given to the solar receiver model, the outlet air temperature of the receiver is computed. The results of the model and the corresponding experimental measurements are presented in Figure 3.26 for comparison. The validation of the solar receiver model focused solely on its thermal aspects since the equation of pressure drop has been already validated in [96].

As depicted in Figure 3.26, the maximum deviation of the solar receiver's outlet air tem-

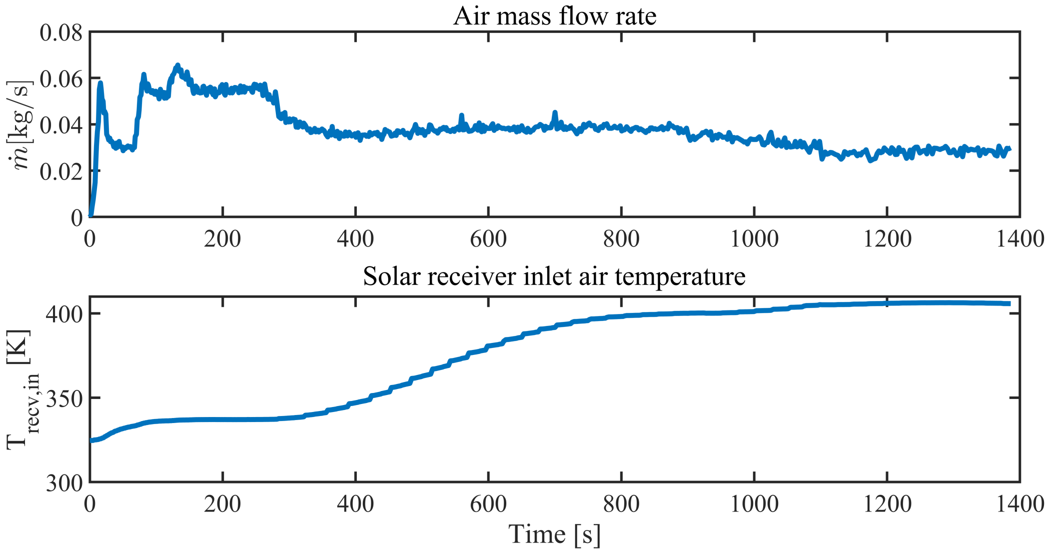

Figure 3.25: The inputs of the solar receiver thermal model for validation.

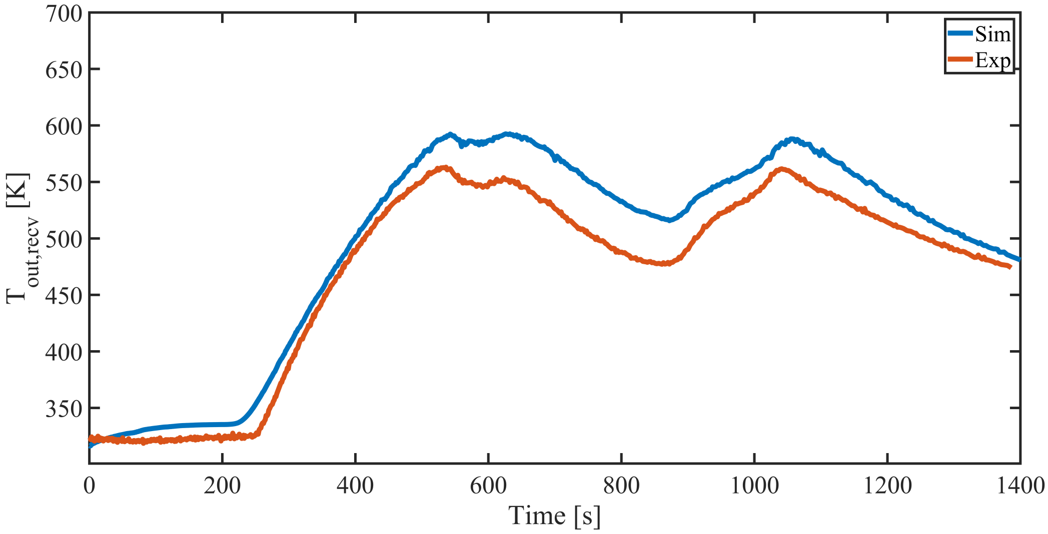

Figure 3.26: Validation results of the solar receiver thermal model.

perature is approximately 8%, indicating a relatively high level of error. It should be noted, however, that due to limited access to the experimental plant, a comprehensive understanding of the system's components was not possible. Specifically, it is plausible that the solar receiver might have experienced greater heat losses compared to the predicted amount in this study.

3.6.4 Permanent magnet synchronous machine (PMSM)

The validation of PMSM was only performed under on-design conditions. Specifically, it was shown that for an electric torque of 0.44 (the predicted torque at the on-design condition with the electric power of 6 [kW_e] and a speed of 130 [krpm]), the RMS voltage and current were calculated to be 170 [V] and 13 [A], respectively. It was explained that the RMS current is proportional to the torque, and therefore, if the torque is calculated accurately, the RMS current should also accurately predict the measurements. The torque, in turn, is related to the generated power or required in the MGT and is a function of the enthalpy difference in the compressor and turbine, which are related to the inlet and outlet temperatures of these two components. Since these temperatures have been validated, it can be inferred that the RMS current accurately predicts the physical values. The RMS voltage, on the other hand, is related to the speed. Therefore, it is necessary to ensure that, for a specific torque and speed, the value of the RMS voltage matches the value expected at on-design conditions based on the datasheet of the PMSM [111]. Given that the PMSM's design condition is to operate at 6 [kW_e] and 130 [krpm], the desired line voltage, which corresponds to the phase to neutral voltage, is expected to be 170 [V]. However, when the model is used to calculate the voltage under the same conditions, it yields a value of 168.1 [V], resulting in a 1% deviation.

3.6.5 Bi-directional converter

The selection of an IGBT converter is crucial in determining its performance in a given operating condition. The main parameters that are considered when selecting an IGBT converter include its nominal voltage and electric current ratings. The six IGBT topology is commonly used in three-phase converters as it provides a reliable and efficient means of converting power. With six IGBTs, the converter can switch the power flow between the input and output phases of the system, providing the required voltage and current levels. This ensures a stable and efficient power transfer, making it a popular choice for many applications. Based on the datasheet from [106], the chosen IGBT for the study was selected to ensure its suitability for the intended application. This must be noted that since the bi-directional converter operates in both motoring and generation conditions, the efficiency in the two operating modes is different. This is due to the dependency of the power loss on the upstream voltage. This means that when the converter is working in the motoring mode, the DC link voltage is used in Equation 3.79 and 3.80 and when it is working in generation mode, the RMS voltage of the three-phase voltage after the generator is used. The main information of the datasheet used in this study is shown in Appendix D. The assumed switching frequency for calculating the IGBTs' switching losses is determined to be 16 kHz based on experimental data.

3.6.6 Control system

Another important aspect of the system model is the design of the control system, which should be tailored to the system's characteristics. To design the controller model for a given system, it is crucial to take into account the system's characteristics and its transfer function. As mentioned earlier, the transfer function of the system with the controller can be represented as a second-order equation, which can be expressed in the standard second-order system form by factoring the denominator of the transfer function, as shown in Equation 3.87. Once the transfer function is in this standard form, it becomes possible to define the damping ratio (ζ) and natural frequency (ω), which are the key parameters that determine the system's behaviour. Knowing these two parameters allows for the determination of the two coefficients of the controller, as illustrated in Figure 3.3.

$$s^2 + 2\zeta\omega s + \omega^2 = s^2 + \frac{(k_p + B)}{J}s + \frac{k_I}{J} \tag{3.87}$$

It is true that the value of the damping ratio is subjective and depends on the specific requirements of the system. However, it is also a well-known fact that second-order systems with damping ratios greater than 1 are over-damped and do not exhibit oscillation. Conversely, systems with damping ratios below 1 and over 0 are under-damped and may exhibit oscillatory behaviour. In many practical cases, a damping ratio of 0.707 is often considered to be an optimal value that strikes a balance between stability and performance. By assigning the value of 0.707 to ζ the calculated coefficients of the controller can be determined as below.

Coefficient	Value
k_p	8.4e-5
k_I	4e-4

Table 3.3: Coefficients of the designed PI controller.

3.6.7 CSP-MGT system

After validating each component using available experimental data, and also defining the coefficients of the control system model, the validation of the entire system becomes necessary. Integrating all the components together allows for consideration of the transient effects they have on one another. The developed transient model for the CSP-MGT system can be compared with experimental data to validate the accuracy of the model. Similar to each component model, the inputs of the CSP-MGT system including ambient conditions (ambient temperature, ambient pressure), DNI and dish focusing schedule are given to the system model, Figure 3.27. Afterwards, the validation results that compare the model outputs, including TIT, TOT, compressor outlet temperature (COT), air mass flow rate, compressor pressure ratio, and turbine pressure ratio, with corresponding experimental measurements are provided.

As previously described in the solar receiver model, the CSP-MGT system has not continuously maintained solar dish focus on the receiver due to the possibility of bearing overheating. To mitigate this issue, a focusing schedule was implemented to adjust the orientation of the dish,

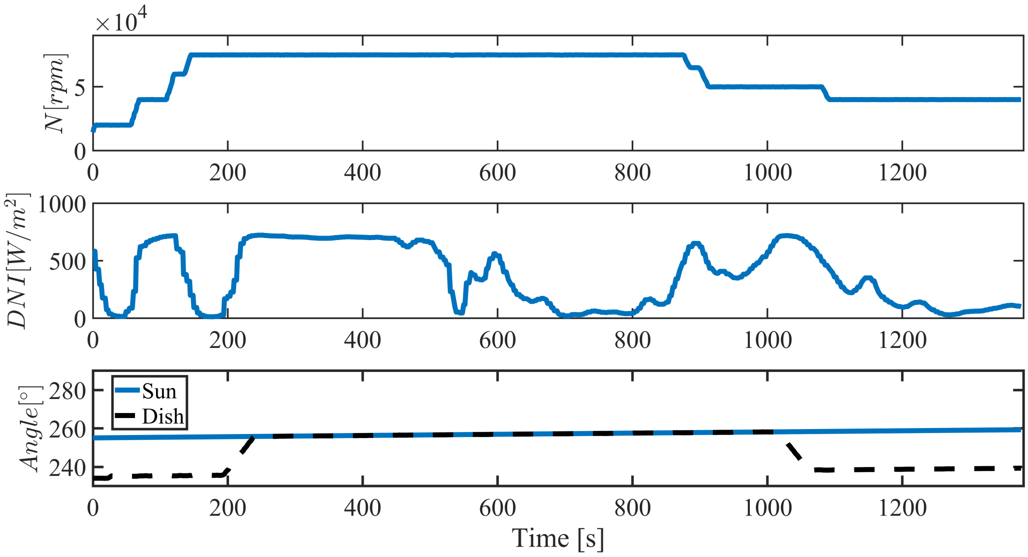

Figure 3.27: The inputs of the CSP-MGT system model for validation.

thereby reducing the likelihood of prolonged focus on the receiver. The current focusing schedule used in the system has not been fully optimised and was instead chosen based on operator feedback to maintain the system's thermal safety. By using these inputs, the resulting outputs of the system are compared with the corresponding experimental data, shown in Figure 3.28.

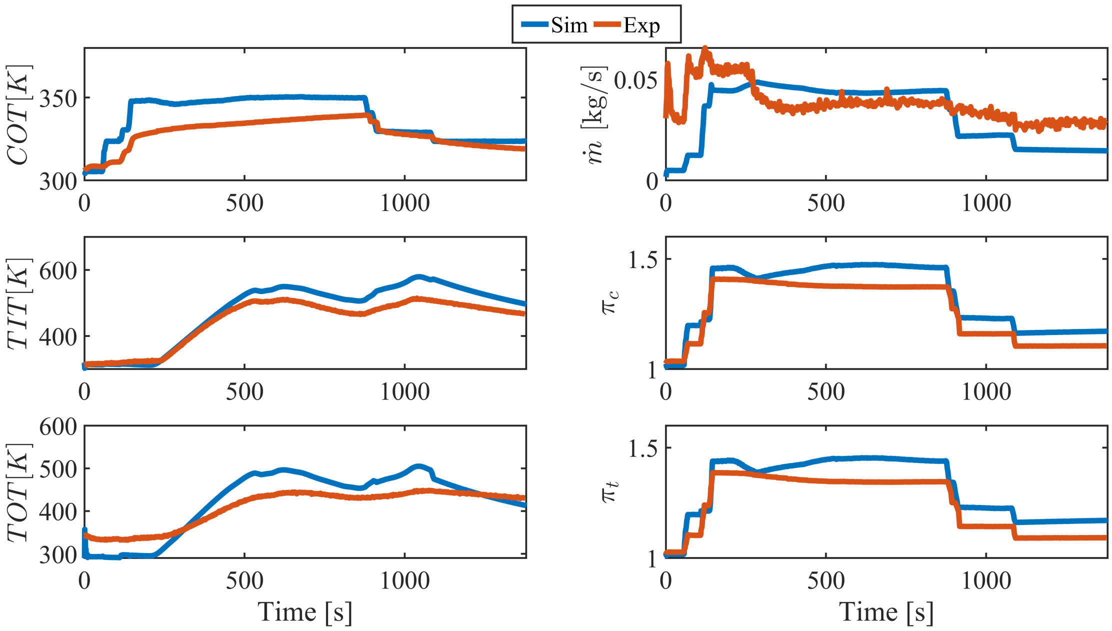

Figure 3.28: Validation results of the CSP-MGT system model.

The figure shows that the predicted COT, which is indicative of the isentropic efficiency, pressure ratio, ambient temperature, and heat soakage, has a maximum deviation error of 4%. Furthermore, it predicts the trend of temperature change quite well. TIT and TOT temperatures have a maximum deviation of 8%, which is considered acceptable for the transient response according to the reason provided for the solar receiver model results. However, the air mass flow rate shows the highest deviation from the experimental measurements due to the high measurement error of this parameter during the tests. As it was mentioned earlier, this can be attributed to the fact that the system was designed to operate at design conditions. The pressure ratio of the compressor and turbine shows a maximum deviation of 7% from the measured data and they also represent the trend of their experimental counterpart, quite well.

3.7 Conclusion

In this chapter, the development of a transient model for a CSP-MGT which is comprised of thermo-mechanical and electrical parts, has been explained in detail. The thermo-mechanical part of the model is based on the lumped volume and one-dimensional discretisation approach which is capable of simulating the transient performance of the system in response to the intermittent nature of the input thermal power. Thermodynamics, heat transfer to the casing and surroundings, shaft rotation, electrical system, control system dynamics as well as mass and heat storage are simulated together to account for their interactions. The model could also be used for real-time simulations due to having 300 times less simulation time than the real transient process. Furthermore, the following points can be concluded from the results presented in this chapter.

- The generation of the low-speed curves of turbomachinery components (from zero-speed to the lowest available one) required for the start-up phase modelling, has been done by introducing a zero-speed curve in the compressor and a zero-speed point in the turbine. This methodology has been shown to be efficient since air mass flow rate and outlet temperature of the turbomachinery components in steady-state conditions have been predicted with an acceptable accuracy of less than 6 %.

- Another crucial aspect examined in this research was the incorporation of heat soakage within turbomachinery elements. By accounting for heat soakage of these components, the analysis of the start-up phase of MGT was enhanced, leading to a 20-30% improvement in temperature prediction accuracy. These findings emphasise the necessity of considering heat soakage when modelling the start-up phase, given the significant temperature differentials involved.
- The transient model's validation has been accomplished for both individual components and the entire CSP-MGT system. Among the component models, solar receiver exhibited the highest discrepancy in outlet temperature with a maximum error of 8%. In the validation of the entire system, the most significant deviation was observed in the predicted air mass flow rate. This disparity could potentially be linked to the substantial measurement inaccuracies encountered at lower speeds.
- The developed model has the potential to be applied in diverse analyses concerning various operations of the CSP-MGT. With its incorporation of an electrical system model, it has the capacity to offer transient insights into both electrical and thermo-mechanical parameters.

Chapter 4

Characterisation of the CSP-MGT start-up schedule

After successfully developing a mathematical model to simulate the transient behaviour of the CSP-MGT system during the start-up phase and validating the results through experimental measurements, the subsequent objective is to establish a tailored start-up sequence for the CSP-MGT. The literature review highlighted that several researchers studied the start-up sequences of the fuelled gas turbines (Chapter 2). Nonetheless, due to the controllable thermal input power, which is not the case in solar-only systems, the start-up phase for solar-only configurations is different and faces additional challenges. Therefore, this chapter focuses on determining the crucial parameters that form the start-up phase of the CSP-MGT. Initially, a modification of the thermal inertia of the turbomachinery components is explained. Subsequently, by using the CSP-MGT with the modified characteristics of the turbomachinery components, the various types of start-up phases are defined based on the system's initial conditions. Finally, the defining elements of the start-up schedule, which rely on the shaft speed, are introduced to characterise the CSP-MGT's start-up process.

4.1 Modifying the CSP-MGT system in terms of thermal inertia

The system specifications that were used in the previous chapter for validation were taken from the real test setup commissioned as a demonstration plant of the OMSoP project at Cassacia. The MGT was designed at City, University of London, as mentioned previously. Due to the shortage of time for the project preparation, the compressor and turbine casing could not be manufactured to be in their ideal form. Manufacturing a single casing unit based on a specific design requires an expensive casting manufacturing process. Consequently, given that the primary objective of manufacturing MGT was for a single demonstration plant and not for large-scale production, the decision was made to fabricate it through a machining process instead. Through this particular manufacturing method, due to the inability to achieve the intended shape for the casings, there was an additional weight for every turbomachinery component. Presented in Figure 4.1 is a cross-section of the designed MGT for the OMSoP project, showcasing the outer side of the casings. The figure was sourced from City partners.

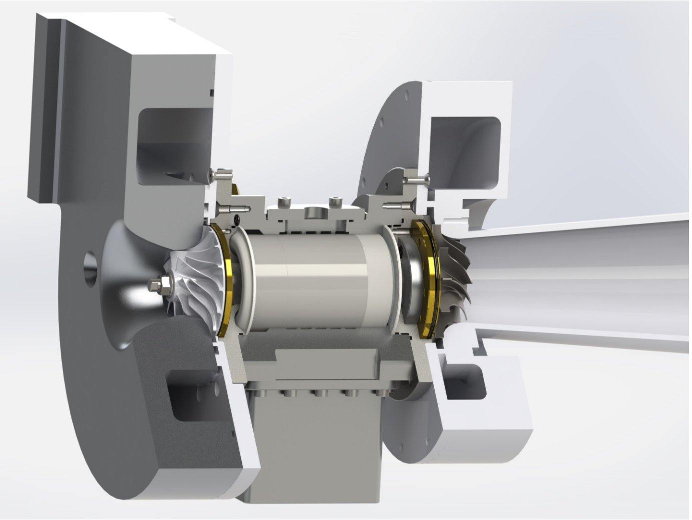

Figure 4.1: The designed MGT for the OMSoP project. [29].

Nevertheless, based on the communications with the designers and manufacturers of the MGT, it was revealed that if the casings' manufacturing was finalised with the help of extra machining or they were fabricated by casting in the first place, the weight of both compressor and turbine were reduced by 75 % which is a significant value. Therefore, for further calculations, the thermal inertia of the turbomachinery components was multiplied by the value of 0.25. Figure 4.2 shows the portion of the thermal inertia of the compressor and turbine before and after this modification.

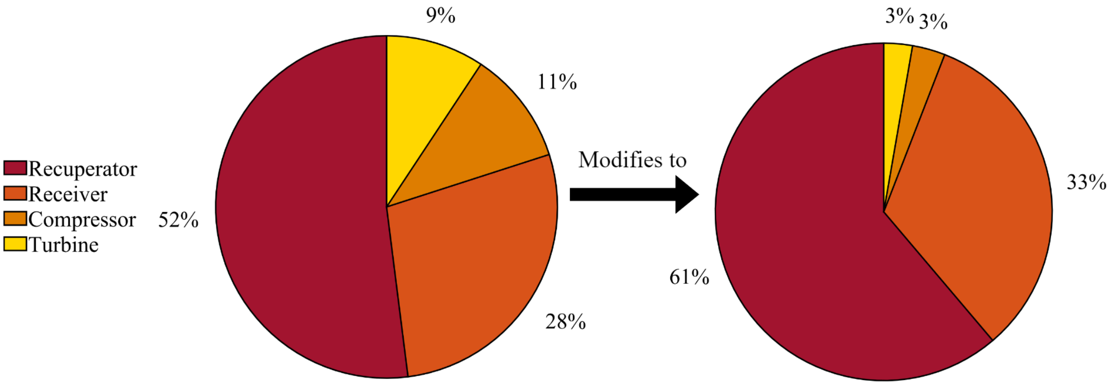

Figure 4.2: The portion of the thermal inertia of each turbomachinery component of CSP-MGT before and after modification.

The figure illustrates that the thermal inertia of turbomachinery components even before modification is significantly lower than that of the solar receiver and recuperator and the two latter components have the dominant thermal inertia in the system. However, due to a high-temperature difference in the turbine, the effect of the turbomachinery component becomes important.

4.2 Start-up types of the CSP-MGT system

It is evident that the types of start-ups for heavy-duty gas turbines are defined based on the duration they have been shut down, whereas for MGTs which are operating solely with solar energy, the strategy for defining the types of start-ups is different. This is due to the fact that these systems do not operate at design conditions most of the time and their operation mode is mainly transient. Therefore the time that the system remains in shut-down mode leads to different conditions for the next start-up. The term "cold start-up" refers to a situation in which the initial temperature of the components' metal is equal to the ambient temperature, which is more likely to occur in the early morning. On the other hand, "warm start-up" refers to the moment when TOT reaches a particular temperature. In the experimental setup, this was chosen to guarantee the prevention of turbine bearing overheating during a re-start-up [81]. Apart from this mentioned reason, TOT is chosen as a criterion for defining the start-up type, because in most of the cases, it is easier to measure and due to having a lower temperature than TIT, the measurement errors are lower [112]. It should be noted that this particular definition of the warm start-up is specific to the OMSoP project, as there is a temperature limit of 120 °C for the turbine bearings. In cases where such limits do not exist or the maximum temperature tolerance is different, the criteria for defining a warm start-up may vary. In a general sense, warm start-up can be described by establishing a specific temperature (mostly TOT) associated with a system component. Based on this strategy, it was agreed that when the system begins to shut down, the shaft speed is kept at 20 krpm and it continues until the recuperator hot side inlet temperature or TOT reaches around 120 $^{\circ}C$. The value of 20 krpm is not an optimum value for the speed and it is the value that was chosen during the tests for cooling down the metal temperatures. When the TOT reached the mentioned value, the shaft speed was decreased to become zero. In the developed model of this thesis, it was assumed that the temperature increase during the time of speed reduction to zero is negligible due to the short time for the speed reduction. Therefore the value of 120 $^{\circ}C$ was used for the warm start-up for further evaluation. Apart from that, it will be shown in the later chapters that the consumed energy for achieving the speed of 20 krpm is very insignificant in comparison with the energy consumption during the whole start-up period. Figure 4.3 shows the hot side air inlet temperature of the recuperator and shaft speed of a conducted test during a day. This test shows two main re-start points that happen during the test. As it is observed in this figure, when the temperature was around 120 $^{\circ}C$ (393 K), the operators decided to re-start the system.

Although the temperature that is shown in Figure 4.3 is associated with the air inlet temperature of the hot side of the recuperator, it is taken as the initial value of the mean wall temperature of the recuperator. The rationale behind this is that, in the transient model, the state variables, including the mean wall temperature of the recuperator, are initialised with spe-

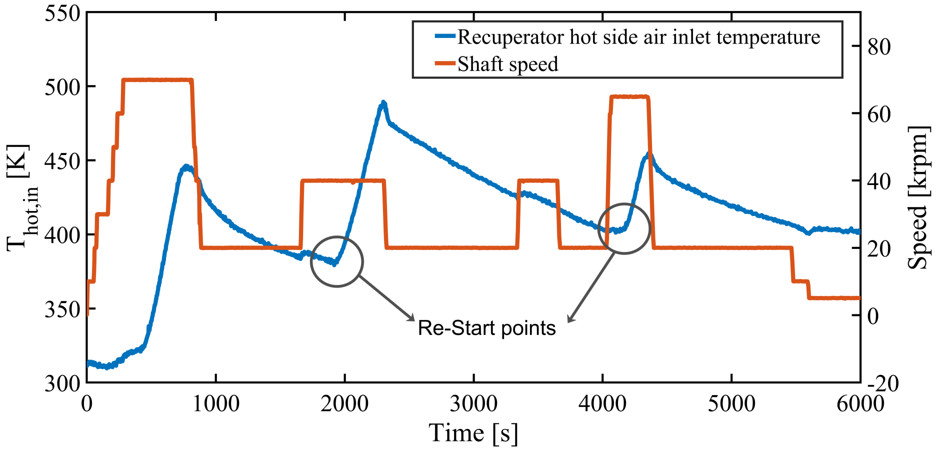

Figure 4.3: Start and re-start points of CSP-MGT during a test for recuperator hot side inlet air.

cific values. Furthermore, the prolonged duration of low shaft speed and the system's consistent maintenance of a single speed value support the reasonable assumption that the hot side inlet air temperature and the wall temperature of the recuperator are nearly identical. Therefore, the temperature value of 120°C was chosen to be the initial temperature of the recuperator metal. The initial temperature of the solar receiver metal was also chosen based on the same strategy from experimental test results. The initial temperature of the solar receiver metal is slightly higher than the recuperator temperature, Figure 4.4. It is essential to note that the temperature value presented for the solar receiver is an average value derived from four sensor data measurements taken at different locations on the solar receiver wall.

The experimental data are provided for compressor and turbine metal temperature as well, Figure 4.5 and 4.6. The mean wall temperature of the compressor, as determined by the outlet temperature, is primarily influenced by the shaft speed and pressure ratio, rather than the duration of solar dish focusing. Consequently, the average inlet and outlet temperature of the compressor does not depend on the initiation time of solar dish focus, but rather on the increase in shaft speed. Thus, the time of the re-start points which were defined by three other components, were used to find the compressor metal temperature.

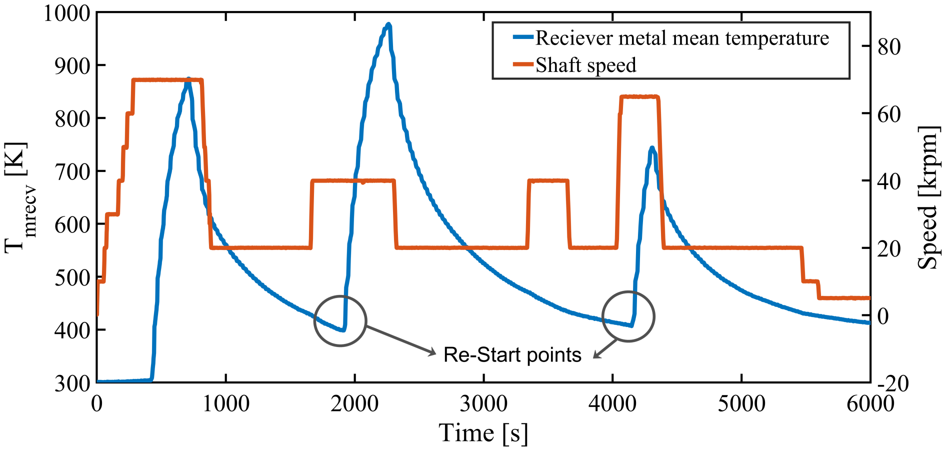

Figure 4.4: Start and re-start points of CSP-MGT during a test for solar receiver metal temperature.

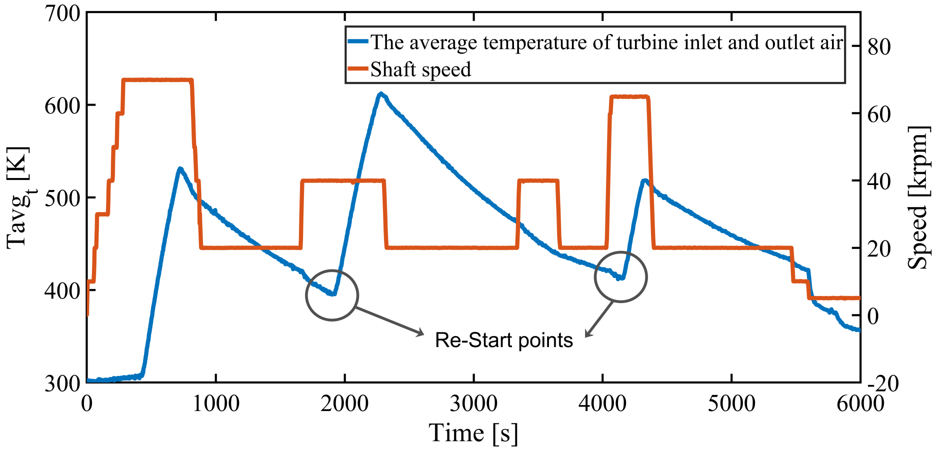

Figure 4.5: Start and re-start points of CSP-MGT during a test for turbine inlet and outlet air average temperature.

Based on the above statements, the initial conditions for the state variables of the CSP-MGT transient model which belong to the components' metal temperatures are provided in Table 4.1 for two types of start-ups: warm and cold start-ups. It must be noted that the ambient condition is chosen to be equal to the ISA at sea level as specified by the ISO.

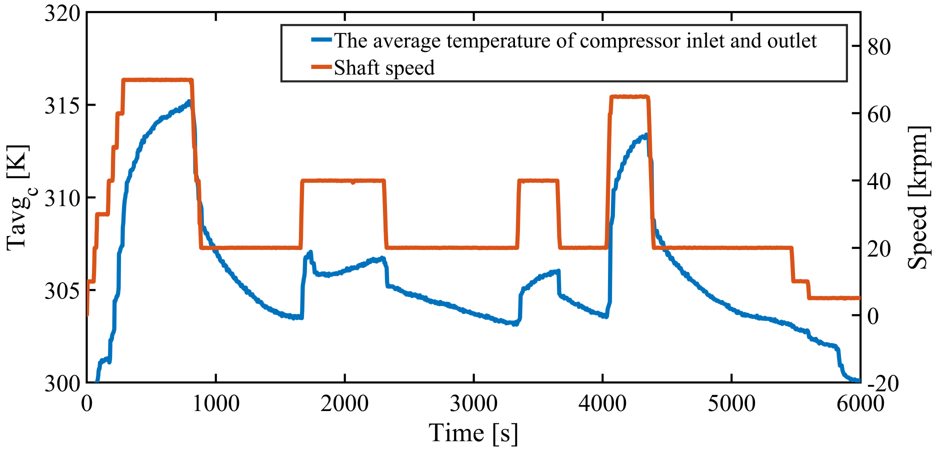

Figure 4.6: Start and re-start points of CSP-MGT during a test for compressor inlet and outlet air average temperature.

Parameters	**Warm start-up**	**Cold start-up**
Receiver mean wall temperature [K]	405	288
Recuperator mean wall temperature [K]	393	288
Turbine mean casing temperature [K]	397	288
Compressor mean casing temperature [K]	308	288

Table 4.1: Initial conditions for the four temperatures of the state variables belonging to the two types of start-ups.

4.3 The defining elements of the start-up phase

As it has been seen in Chapter 2 [8], researchers have revealed that the most effective method to control CSP-MGT operation is by varying shaft speed through voltage adjustments. While maintaining a constant TIT at its maximum value establishes the reference speed as an input for the control system during load fluctuations to achieve peak efficiency, a different reference speed is necessary during start-up. It is important to note that during start-up process, the maximum value of TIT serves as a safety limit for the system rather than a targeted operational strategy. Therefore, to initiate the CSP-MGT start-up process, the system requires a reference speed as an input, which is directly used for controlling the shaft speed. The reference speed is not given to the system as a constant value which might lead to a rapid acceleration due to an undefined speed increase rate. This is due to the fact that the electric drive of MGT (PMSM) needs to accelerate from zero to the reference value within a short period of time, which may not always be feasible depending on the aimed reference value. This is because it might require a high electric current, which is limited to a maximum value, related to the constraints of the electric drive. The speed schedule can be defined through various methodologies such as continuous mathematical equations like polynomial sentences or sequential separate mathematical parameters. The latter strategy is more flexible because it can be more definitive for the stages of the start-up phase. Therefore it has been adopted for producing the speed schedule. Based on the start-up sequence in the fuelled MGTs in the literature, three steps have been also adopted for the CSP-MGT start-up schedule [27]. Figure 4.7 shows the form of speed schedule parameters of the speed schedule and Table 4.2 explains each parameter.

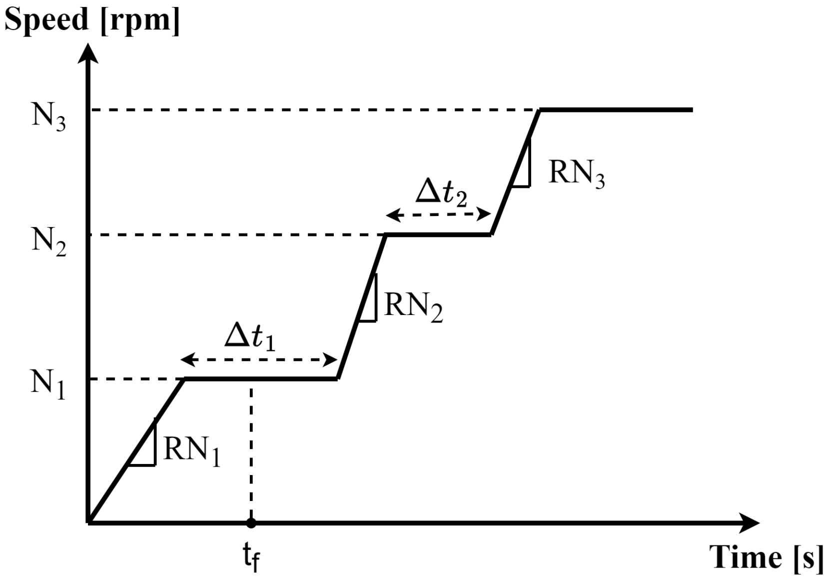

Figure 4.7: The defined parameters of the CSP-MGT start-up speed schedule.

The specific ranges have been assigned to speed schedule parameters, and their ultimate values must fall within these predefined boundaries. The determination of these ranges is influenced by the physical constraints of the CSP-MGT system and the desired operating conditions, which are dependent on the thermal input power. Table 4.3 displays the designated values for

Parameter	Definition
$N_1[krpm]$	First resting speed (Focus speed)
$RN_1[krpm/s]$	First speed change rate
$t_f[s]$	Focus time
Δt_1	First resting time period
$N_2[krpm]$	Second resting speed
$RN_2[krpm/s]$	Second speed change rate
$\Delta t_2[s]$	Second resting time period
$N_3[krpm]$	Third resting speed (Rated speed for the specific DNI)
$RN_3[krpm/s]$	Third speed change rate

Table 4.2: The definition of the parameters of start-up speed schedule.

the speed schedule parameters. The reasoning behind the selection of each parameter's range is explained in the subsequent paragraphs.

- **N_1:** This speed represents the initial resting speed of the MGT at which the CSP dish begins focusing. A lower resting speed shortens the time required for the solar receiver to heat up, as it reduces the mass flow rate during thermal energy absorption. The maximum value for this speed range is constrained by temperature limitations in the solar receiver as the critical component. On the other hand, the minimum value is determined by the electric drive capacity of the system, which has a predefined maximum electric current threshold and cannot handle higher values. Consequently, when the turbine is not generating power from solar thermal power, the electric drive can only increase the speed to a maximum of 90 krpm. To ensure adequate mass flow rate of the solar receiver, the minimum value for N_1 has been established as 10 krpm.

- **RN_1:** This parameter specifies the speed at which the electric drive needs to reach the shaft speed to achieve the desired N_1 value. To establish the minimum and maximum values for this parameter, we considered the time required for the speed to increase from zero to N_1 values to be 5 s and 20 s. By dividing the larger speed difference by the shorter time period, the upper limit of RN_1 is computed. Conversely, the lower limit is calculated by determining the minimum speed rate from zero speed to the lowest value of N_1 within the longest feasible time frame, subject to the constraints. Furthermore, the two computed speed change rate values were tested on the model, revealing that the rate cannot exceed 18 krpm/s due to insufficient current of the electric drive. This is because, the term of $J\frac{d\omega}{dt}$ in Equation 3.61 becomes significant and adds up to τ_A substantially. To establish the upper limit of the speed change rate, a slow rate was computed by selecting a 20 s time period for the speed to reach 10 krpm (the lower bound of N_1). Since the lower bound of this parameter is of less importance, a value based on the sense of engineering has been chosen.

- **Δt_1:** During this specific duration, the shaft speed of N_1 remains constant. If this duration is too short, there won't be enough time for the solar receiver to warm up sufficiently, resulting in a substantial amount of torque being required from the electric drive. Consequently, the electric drive will be unable to supply the high electric current. On the contrary, if this duration is excessively long, the input heat will cause the receiver's mean-wall temperature to increase at a higher rate, which can result in overheating. The range chosen for this duration was established between 1 second and 8 minutes, with the maximum limit varying for each DNI. The upper bound of this parameter decreases as the DNI value increases. It is important to emphasise that the values for the lower and upper bounds were determined through optimisation using arbitrary values, aiming to identify an appropriate range that is believed to satisfy the constraints. A minimum value of 1 second has been designated for this parameter, taking into account the shortest timescale required for start-up time. The decision to avoid selecting zero as the value is attributed to the need for allocating time for CSP dish focusing.

- **t_f:** The beginning of dish focus refers to the time when the solar dish of a CSP system begins transferring solar energy to the solar receiver. This can occur either at the moment the shaft speed reaches the value of N_1, which ensures that a continuous airflow through the MGT is maintained to prevent overheating, or when the shaft speed initiates the increase to the value of N_2. As a result, the value range for the focus time, denoted by t_f, is determined based on the values of N_1, RN_1, Δt_1.

$$t_{f_{min}} = \frac{N_1 - 0}{RN_1} \tag{4.1}$$

$$t_{f_{max}} = \frac{N_1 - 0}{RN_1} + \Delta t_1 \tag{4.2}$$

where the term $t_{f,min}$ represents the moment when the shaft speed reaches N_1, while $t_{f,max}$ represents the time when the shaft speed transitions from N_1 to N_2 and begins to increase.

- **N_2:** This parameter is the second speed where the shaft speed remains constant. The value of this speed must be greater than the first speed (N_1) to form the speed schedule shown in Figure 4.7. This speed has to be equal to or lower than the rated speed of the corresponding DNI value. To define the widest possible range for N_2, the lower bound of this parameter was set to be 10 krpm greater than the lower bound of N_1). The upper bound of this parameter is defined based on the rated speed of each DNI value.

- **RN_2:** This parameter refers to the rate of speed increase from N_1 to N_2. The strategy for defining the upper and lower bounds is similar to RN_1. However, the computed values were almost the same and it was decided to use the same range.

- **Δt_2:** This parameter denotes the duration over which the speed of the shaft remains constant at N_2. The lower bound of Δt_2 is zero, as it is possible that the shaft may not need to maintain at the constant value of N_2 and can continue accelerating. On the other hand, the maximum allowable value for Δt_2 is decided to be equal to the high bounding limit of Δt_1.

- **N_3:** This parameter is the ultimate shaft rotational speed obtained through computations for the steady-state off-design speed, resulting in the maximum power output for each

DNI. This speed is called rated speed. The lower and higher bounding limits of this parameter are equivalent.

- RN_3**:** This parameter is the speed increase rate from N_2 to N_3. The lower bound of this parameter is zero due to the case in which the shaft speed increases from N_1 to N_3 directly. The higher bound of this parameter is decided to be equal to the higher bounding limit of RN_2 and RN_1.

The strategy for defining the lower and upper bounds of these parameters of the speed schedule was used for each DNI. Table 4.3 illustrates the lower and upper limits of these parameters for DNI=900 (The highest DNI value which was used in this study) as an illustration.

Parameter	Lower and upper limits
$N_1[krpm]$	[10 to 90]
$RN_1[krpm/s]$	[0.5 to 18]
$t_f[s]$	[t_1 t1+Δt_1]
$\Delta t_1[s]$	[1 to 480]
$N_2[krpm]$	[20 to 123.4]
$RN_2[krpm/s]$	[0.5 to 18]
$\Delta t_2[s]$	[0 to 480]
$N_3[krpm]$	[123.4]
$RN_3[krpm/s]$	[0 to 18]

Table 4.3: The design space for main parameters of the speed schedule for DNI=900 [W/m^2] as an example.

where t_1 is the time at which the speed reaches N_1 and is calculated as follows.

$$t_1 = N_1/RN_1; \tag{4.3}$$

The speed value of 123.4 krpm is the speed at which the CSP-MGT system can generate the highest power according to the DNI value of 900 W/m^2.

4.4 The requirements of the start-up procedure

The start-up phase of the CSP-MGT follows a procedure which is related to the control strategy. Based on the control strategy, shaft speed is required to follow a reference speed schedule to reach a specific speed. The reference speed is defined based on the measured value of DNI and the initial condition of the system. This schedule is then given to the control system as a reference schedule. The comparison between the current speed and the reference value generates a different voltage for PMSM which requires a different electric current. Consequently, a different torque is produced by PMSM to alter the shaft speed. A general procedure of the start-up procedure from sensing the DNI to introducing the speed schedule is illustrated in Figure 4.8.

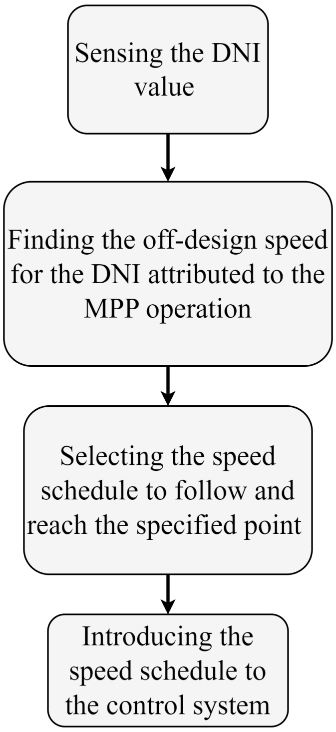

Figure 4.8: The sequential stages for introducing the speed schedule to CSP-MGT system.

As it can be observed in Figure 4.8, in order to proceed with the start-up, knowing the rated speeds for each DNI value is required. The value of the rated speed is found based on having MPP operation for the specific value of DNI. In the previous study, the rated speeds were calculated with the help of an off-design calculation [8]. However, the results were not validated with the experimental test results because the experimental measurements were not available at that time. In this study, the rated speeds for each DNI are found by running the transient model for different cases until they reach their steady-state condition. Then the steady-state values of the transient responses would be the off-design values for the associated DNI. Based on this strategy, the rated speeds for each DNI related to the MPP operation are demonstrated in Table 4.4.

DNI [W/m^2]	N [krpm]
300	63.15
400	78.65
500	89.9
600	99.63
700	107
800	115.5
900	123.4

Table 4.4: The rated speeds for each DNI based on MPP operation strategy.

Figure 4.9 illustrates the power generation results of the CSP-MGT system for different DNI values. In the previous study focusing on the CSP-MGT system during the design phase, it was determined through off-design modelling that at DNI = 800 W/m^2 and N = 130 krpm, the generated mechanical power was 6.5 kW, resulting in an electric DC output power of 5.5 kW_e with an electric efficiency of 88 %. However, upon validating the transient model with experimental data, it was determined that achieving this design condition was not feasible for the CSP-MGT demonstration plant. Consequently, under the MPP operating condition with DNI = 800 W/m^2, the generated electric DC power was approximately 30% lower.

As depicted in the figure below, power generation commences when the DNI reaches a value between 200 and 300 W/m^2 and the power generation at 265 W/m^2 is zero. The electric DC power generated at a DNI value of 300 W/m^2 is relatively low, amounting to 0.255 kW_e.

Furthermore, it will be addressed in future sections that the start-up phase of the system, specifically when the DNI is 300, necessitates a significant duration of around 20 minutes. However, considering that the DNI is not constant during the start-up period and it either fluctuates or increases on sunny days, this DNI value can serve as a suitable criterion for initiating system operation.

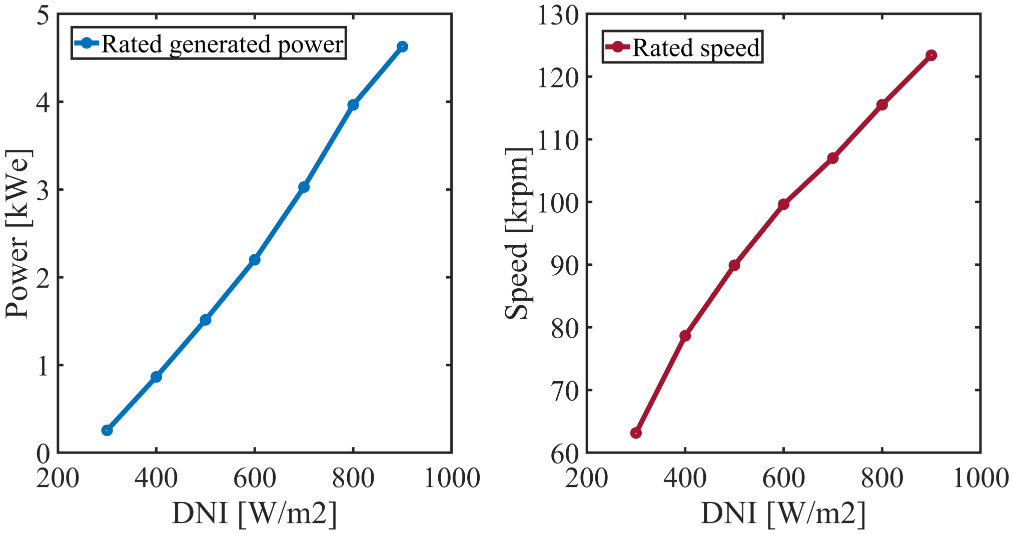

Figure 4.9: The generated power and associated rated speed for the MPP operation in various DNIs.

It is worth mentioning that the focus of this study is on the CSP-MGT in off-grid mode where there is limited access to the national grid. In addition to that, due to the intermittency of solar energy, these systems cannot be used to respond to consumers' demands (load-following operations) without a backup such as a combustor or thermal energy storage. Therefore, a scenario has been adopted for this study that the required power for start-up is coming from a DC source like battery and on the generation side, the amount of DC power is evaluated that could be used for applications like electrolysis for producing hydrogen.

4.5 Conclusions

The main objective of this chapter was to delineate the crucial parameters influencing the start-up phase of the CSP-MGT system where the MGT operates solely with solar energy. Firstly, a modification to the thermal inertia of turbomachinery components is implemented and explained. Secondly, the types of start-up phases have been categorised according to the initial conditions of the entire system. Thirdly, the factors that define the start-up schedule, based on the shaft speed, were presented. This approach was employed to establish a framework for characterising the start-up schedule of the CSP-MGT system. The technical conclusions are listed below.

- A novel approach is presented to categorise the type of start-up for a CSP-MGT system that relies solely on solar energy. Rather than considering shut-down duration, a specific system temperature, specifically the mean wall temperature of the recuperator, is proposed as the criterion to differentiate between warm and cold start-up types. This is because, the CSP-MGT system does not shut down from the same operating condition every time, as is the case in fuelled MGTs.
- In contrast to fuelled MGTs, CSP-MGTs are controlled based on a reference speed rather than a reference input of fuel mass flow rate. It has been demonstrated that a speed reference schedule is necessary instead of a fixed speed value. This requirement arises from the constraints imposed by the electric current.
- Evidence demonstrated that employing a sequential approach in formulating the speed schedule of a CSP-MGT, with distinct stages for speed, is more advantageous than adopting a continuous speed schedule. The rationale behind this preference lies in its ability to offer greater flexibility, particularly in accurately determining the various phases of the start-up process.

- The speed schedule of a CSP-MGT consists of distinct stages, with each stage being characterised by a parameter that is assigned within a specific range. The boundaries of these parameter ranges are determined based on the safety considerations associated with the entire system. The safety criteria which play an important role in defining the bounding limits for each parameter are electric current, electric power and critical components' temperature.

Chapter 5

Optmisation of the start-up schedule

As demonstrated in the preceding chapter, it is apparent that optimisation is necessary for the start-up phase of the CSP-MGT. During this phase, there are several concerns that highlight the importance of discovering the optimal schedule. The primary concern is associated with the safety of the entire system. The second concern is linked to the energy consumption, the maximum required power, and the time required for the motoring mode. It is essential to minimise the energy consumption and maximum required power while reducing the start-up time for the CSP-MGT system. These three factors are important as they are considered to be the cost factors of the system operation. In addition to that, it is important to find a definitive form for the start-up schedule that is the finalised optimal sequences of the start-up phase of a CSP-MGT which provides safety and efficiency.

5.1 Analysis of the optimisation problem

In the field of engineering, optimisation is a common approach used to enhance the performance of various systems. The primary objective of optimisation problems is to find the optimal values of decision parameters that can minimise the objective function(s) of the system. The decision parameters, objective functions and constraints are the three main parameters of an optimisation problem. The decision variables are the parameters that can be adjusted to optimise the system, while the objective function(s) represents the performance measure(s) of the system that needs to be minimised. Constraints are the limitations or conditions that the solution must satisfy. The optimisation procedure is executed within the decision space, which is the range of values within which the decision variables can be varied. During the optimisation process, the mathematical algorithm may generate results that exceed acceptable limits (constraints of the model). In these situations, the system model assigns the highest value among the outputs (objective functions) to these outcomes. Since the goal is to minimise the objective functions, they are consequently removed from the final set of solutions. This ensures that only feasible solutions are considered for the optimal design of the system.

5.1.1 Defining the decision variables and constraints

This section aims to identify the decision variables and system constraints necessary for conducting the optimisation procedure. As previously explained, the speed schedule which is used as an input (reference speed) for the CSP-MGT during the start-up phase, defines the transient performance of the system during this phase. Consequently, it determines the system safety, energy consumption, start-up time and maximum electric power requirements. Therefore, the decision variables consist of parameters used to characterise the speed schedule, which has been explained in detail in Chapter 4. The safety of the start-up is evaluated based on various constraints, including critical temperatures, compressor surge margin, maximum electric current of the drive, and maximum electric power. If any of these constraints exceed their limit, the optimisation framework will not consider the associated speed schedule parameters as a solution for the system start-up. The critical temperatures are determined based on the thermal tolerance of the material used for each component. In this regard, Austenitic stainless steel 253 is used for the solar receiver, which can withstand temperatures up to 1150 °C, while the maximum temperature tolerance of the recuperator material, which is made of stainless steel, is around 650 °C that limits the TOT value. The turbine for the OMSop project was made of titanium aluminide (AlTi), which is capable of withstanding temperatures as high as 900 °C which means that the air inlet temperature of the turbine cannot exceed 900 °C. Another limiting constraint is related to the compressor surge margin which is calculated using equation 5.1, and it is based on a constant speed curve strategy where π_s is the pressure ratio on the surge line associated with π_{op} at the same speed curve, as outlined in [113].

$$SM = (\frac{\pi_s}{\pi_{op}} \frac{\dot{m}_{mf,op}}{\dot{m}_{mf,s}} - 1) \times 100 \tag{5.1}$$

where SM is the compressor's surge margin and the subscripts of mf,s and mf,op refer to the modified parameter on the surge line and operating line respectively. As it was explained in [75], for a generating gas turbine, the surge margin should not be less than 15-20 %.

In addition to these constraints, the maximum electric current that can be extracted from the electric drive is 13 Amps, based on the technical data from the datasheet of the chosen electric drive. The maximum value of electric current is a limiting factor for shaft speed which confines the increase rate and the aimed shaft speed in the start-up procedure.

5.1.2 Defining the objective functions

The start-up phase is considered to be a cost factor of the CSP-MGT operation where no electric power is generated, instead, electric power is required. In this case, a starter is necessary for the start-up phase to provide the required electricity. Determining the starter capacity is an important parameter, particularly when the system is operated in off-grid mode, as it determines the maximum battery capacity required to initiate the system operation. In this context, the term "capacity" refers to the battery's nominal power output. However, when the system operates in grid-connected mode, the calculation of starter capacity is not necessary since the required power for start-up is supplied from the grid. It is worth noting that the maximum required power as an objective function is different from the nominal power of the PMSM and other components of the drive since they are regarded as constraints of the CSP-MGT transient model. The first objective in determining starter capacity is to calculate the maximum value of the required power in the transient response of the transient model during start-up. This objective is found with the help of the transient response of the required electric power during the start-up phase.

$$Maximum\ required\ power = Max(PW_e(t)) \tag{5.2}$$

The second objective is to determine the consumed energy by the system until it reaches the self-sustaining point or the beginning of the generation point. This objective is calculated by integrating the area under the electric power versus the time curve. It must be noted that the self-sustaining point is referred to the operating point that the generation and motoring power are equal.

$$En_e = \int_0^{SS_{point}} |PW_e(t)|\, dt \tag{5.3}$$

where SS_{point} is referred to self-sustaining point and the subscript of e refers to the electric.

The optimisation process also considers a third objective function, namely the duration of the start-up phase. A shorter start-up time allows for a longer power generation period, while also reducing the likelihood of changes in DNI occurring during the start-up phase. Minimising the start-up time increases the flexibility of the system as well. Flexibility in power generation refers to the ability to respond rapidly to changes in demand or compensate for fluctuations in renewable energy generation. The calculation of this objective function involves the incorporation of the speed schedule parameters and the time required for the system to initiate the generation mode and it is calculated as below.

$$ST = \frac{N_1 - 0}{RN_1} + \Delta t_1 + \frac{N_2 - N_1}{RN_2} + \Delta t_2 + \frac{N_3 - N_2}{RN_3} + \Delta t_g \tag{5.4}$$

where Δt_g is the duration when the shaft speed remains constant with N_3 value until the generation begins.

In this study, in order to conduct the optimisation procedure for finding the optimised parameters of the speed schedule, it was assumed that the DNI does not change during the start-up phase. Although this assumption is far from reality, the optimised parameters of the speed schedule for each DNI value will be applied to the real condition by adopting a methodology which will be explained in detail in the next chapter for the annual analysis of the CSP-MGT performance.

5.1.3 Sensitivity analysis

The sensitivity of the defined objective functions to the decision variables must be evaluated once the objective functions are established. This is important for determining the necessity of conducting optimisation and also identifying which decision variables have the least impact on the objective functions. The sensitivity analysis is performed for the three objective functions of maximum required power, energy consumption, and start-up time. To conduct the sensitivity analysis, a reference point must be defined to compare different cases with this point. Since there is no predefined speed schedule, the reference values for the decision variables were set as the average value between the maximum and minimum bounding limits. Although the analysis was done for all DNI values, the sensitivity analysis was only presented for a DNI value of 800 $W/m2$. Since the maximum value of DNI is mainly between 900 and 800, and DNI=900 $W/m2$ is not a frequently occurring maximum value for DNI, the value of 800 has been chosen as the maximum DNI value that might occur during a day. The results of sensitivity analysis for the three mentioned objective functions are shown in Figures 5.2 to 5.3. There are nine variables whose bounding limits are shown in table 5.1.

	N_1 $[krpm]$	RN_1 $[krpm/s]$	Δt_1 $[s]$	N_2 $[krpm]$	RN_2 $[krpm/s]$	Δt_2 $[s]$	RN_3 $[krpm/s]$	N_3 $[krpm]$	tf $[s]$
Min	10	0.5	1	20	0.5	0	0	115.5	0.551
Max	90	18	580	115.5	18	580	18	115.5	760.0

Table 5.1: The bounding limits of each decision variable of start-up phase for DNI = 800 $[W/m2]$

For conducting the sensitivity analysis, 2 × 8 simulations have been conducted. Two is for the low and high bounding limits and eight is for the eight decision variables. Since the variable of N_3 does not have a maximum and minimum and it is a constant value, it is not taken into account in the sensitivity analysis which makes the number of the decision variables eight from nine. At each step, one of the variables is tested for sensitivity analysis and the maximum and minimum value of the regarding parameter is used for forming the speed schedule while the rest of the variables are in their reference values. Since the reference point was chosen to be the mid values of all decision variable ranges, there are some cases that the speed schedule includes a decreasing trend in the speed schedule instead of an increasing trend. For example for evaluating the effect of the minimum bound of N_2 value, the speed schedule uses N_1 parameter with its reference value (mid value) which is 50 [krpm] and N_2 parameter with the value of 20 [krpm]. This causes an invalid speed schedule according to the aim of the start-up. In those cases, the value of each objective function is shown to be equal to their reference values (with a sensitivity of 0%) which in the above figures they seem to be undisplayed. In another case, when the minimum bounding limit of RN_3 which is zero is chosen, it means that the N_2 speed remains at its reference value for the whole start-up time and the speed will not reach N_3. This will cause the receiver mean-wall temperature raises to the critical value and the start-up procedure stops. In this case, also it was decided to use the result of the value of the objective function according to the reference value.

Apart from the mentioned cases, there are some occasions when the electric current is more than the limit which required the electric power of the motor to be higher than 6 [kW_e]. These cases are associated with a high increase rate of speed and also remaining at a constant speed for a short time that does not give the chance for the receiver mean-wall temperature to raise and therefore the generated power by the MGT cannot assist the motor during the start-up. For these mentioned cases, the required power is more than the maximum limit and they are shown with a value of nominal power in the figures. Figure 5.1, to 5.3 show the sensitivity analysis results for the three mentioned objective functions. The percentage of change in the objective function amount is compared with the case that the decision variables have their reference values.

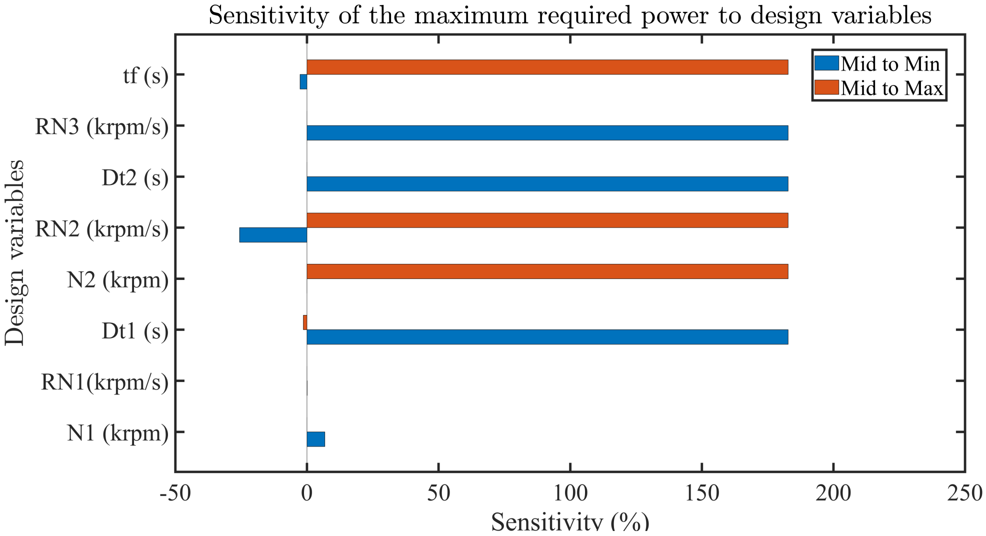

Figure 5.1: Sensitivity analysis of the maximum required power to the speed schedule parameters for DNI = 800 [W/m^2].

Analysing Figure 5.1, with the exception of cases where the speed schedule is invalid, it is evident that most decision variables can cause the required power to exceed the limit, indicating that the decision variable values are either too low or too high. Therefore, the impact of decision variable values on the required power is clearly observable. Notably, the increase rate of the first speed, RN_1, has the least effect on the maximum required power. This is primarily because when the change rate of the speed is significant, it is multiplied by the speed itself, thereby

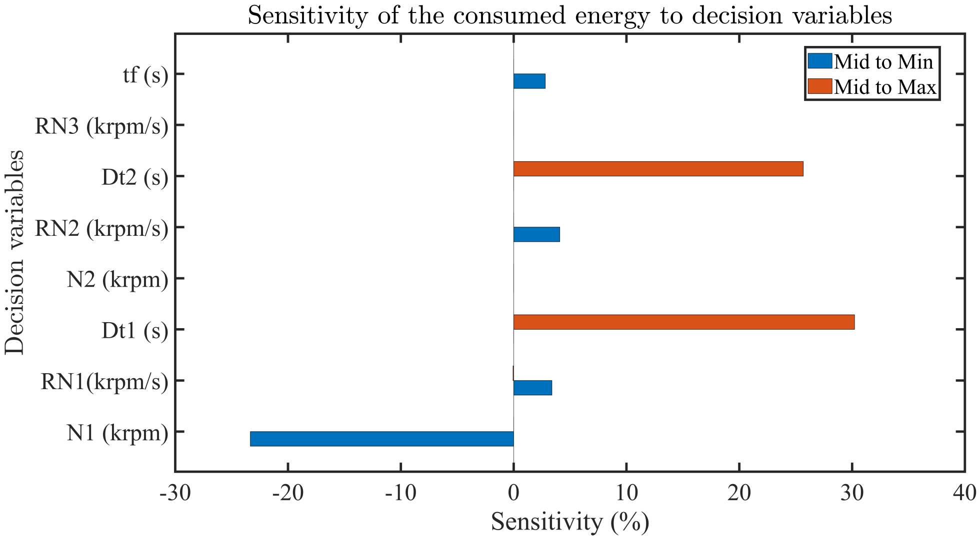

Figure 5.2: Sensitivity analysis of the consumed energy to the speed schedule parameters for DNI = 800 $[W/m^2]$.

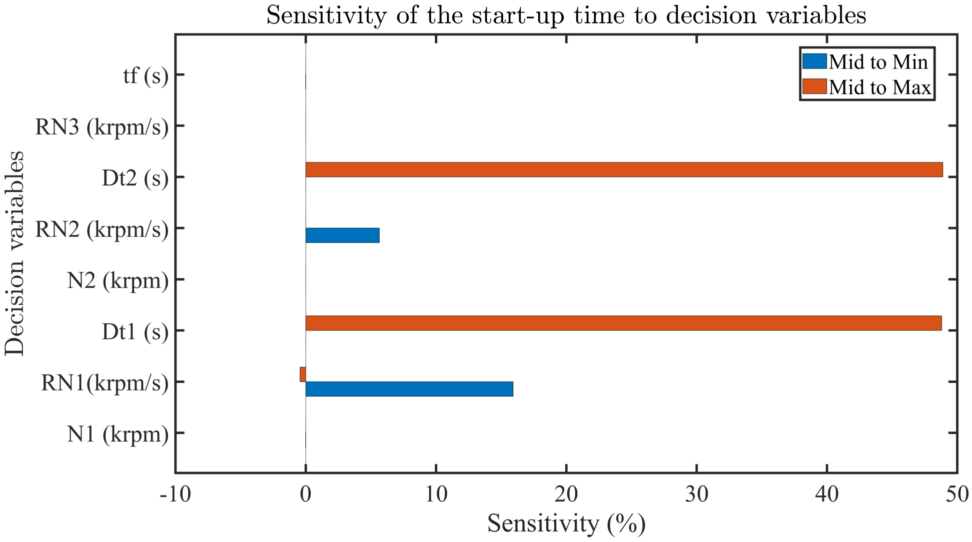

Figure 5.3: Sensitivity analysis of the start-up time to the speed schedule parameters for DNI = 800 $[W/m^2]$.

amplifying the influence of the speed value as well and since the value of the N_1 is not high, it has the least effect on the required power.

When the speed change rate is insignificant, the term $J\frac{dN}{dt}N$ in the energy conservation equation of the shaft, is even less effective on the required power. Furthermore, the first speed,

N_1 has the least impact on this objective function after RN_1. It is observed that even utilising the minimum bounding limit of N_1 increases the required power, albeit by a very small amount. As for the other speed, N_2 it can also be noted that the lower bounding limit leads to an invalid schedule which is not shown in the figure. However, setting a higher bounding limit for $N_2(N_3)$ requires a power higher than the nominal value for the start-up. This is because, for a constant value of RN_2 the shaft speed must reach N_3 from a lower speed, necessitating more time for speed to increase and thereby the likelihood of increasing the term of $J\frac{dN}{dt}N$ is raised which yields to a high value of power requirement. The change rate of speeds appears to be limited when used with their high bounding limit. In the case of RN_2, it is demonstrated that using the lower bounding limit decreases the maximum required power by approximately 25%. This is because at this stage when CSP dish is focused, it is beneficial to increase the shaft speed as slowly as possible. On the other hand, for RN_3 it is observed that increasing the shaft speed at a slower rate, results in overheating of the solar receiver which stops the simulation and it is not shown in the results.

The timing of the focusing process reveals that if it occurs late, the required power exceeds the limit, whereas if it occurs early, it may require the same or lower power compared to the reference schedule. Hence, it is preferable for the dish to focus as early as possible. Regarding the Δt terms, it is evident that they should be as large as possible, as the shortest period does not allow sufficient time for the entire system to warm up.

Figure 5.1 illustrates the impact of decision variables on energy consumption during start-up. Unlike maximum required power, there is no upper limit for energy consumption, so the cases with exceeded limits are not shown in the figure. The analysis reveals that setting a minimum bounding limit for N_1 leads to a 25% decrease in energy consumption, indicating its significant effect on the objective. This is attributed to a lower air mass flow rate resulting in a faster warm-up of the solar receiver. The two increase rates of speed (RN_1 and RN_2) have minimal impact on energy consumption, unlike power requirements. During resting periods, employing the highest bounding limit for Δt_1 leads to a 30% increase in energy consumption, and Δt_2 shows less impact but it is still noticeable.

The final sensitivity analysis pertains to the start-up time. As mentioned earlier, it is not feasible to evaluate the start-up time for cases where system constraints are not met. Nevertheless, among the analysed cases, it is evident that the two resting time periods (Δt_1 and Δt_2) have the most significant impact, resulting in an increase of over 50% in the start-up time. Additionally, the first speed increase rate (RN_1), which had minimal effect on the previous objective functions, is shown to increase the start-up time period by 20%.

It is crucial to emphasise that all decision variables have inter-dependencies. While this sensitivity analysis primarily concentrated on evaluating the effects of individual parameters, it yielded valuable insights for the optimisation process. Consequently, it can be inferred from this analysis that optimisation is necessary to ensure both safe and efficient operation for the start-up phase.

5.1.4 Multi-objective optimisation algorithm

The three earlier explained objectives are interrelated which means any change in one of them would cause a change in one another. The start-up phase of the CSP-MGT system is aimed to require the minimum power and consume the minimum amount of energy. In the meanwhile, the start-up time is aimed to have the minimum value which leaves more time for power generation and also it can make the system more flexible. A common technique for conducting the optimisation problem is to adopt a single function which is made of combining the mentioned objective functions as it is shown in Equation 5.5.

$$F(x) = \omega_1 f_1(x) + \omega_2 f_2(x) + \ldots + \omega_N f_N(x) \tag{5.5}$$

where $f(x)$ represents individual functions each of which is multiplied by a weight factor, ω. However, such combination technique suffers from a main problem in that they rely on how they are defined which directly affects the final function and consequently, it affects the optimisation results. In order to deal with the shortcoming of this method, Pareto front concept has been introduced. Pareto front concept gives the chance to do an equally weighted study for multi-objective optimisation. This means that no weighting factor is required and results are not presented in one single point but a number of answers which form the optimal front will be taken as solutions. This concept is shown in Figure 5.4.

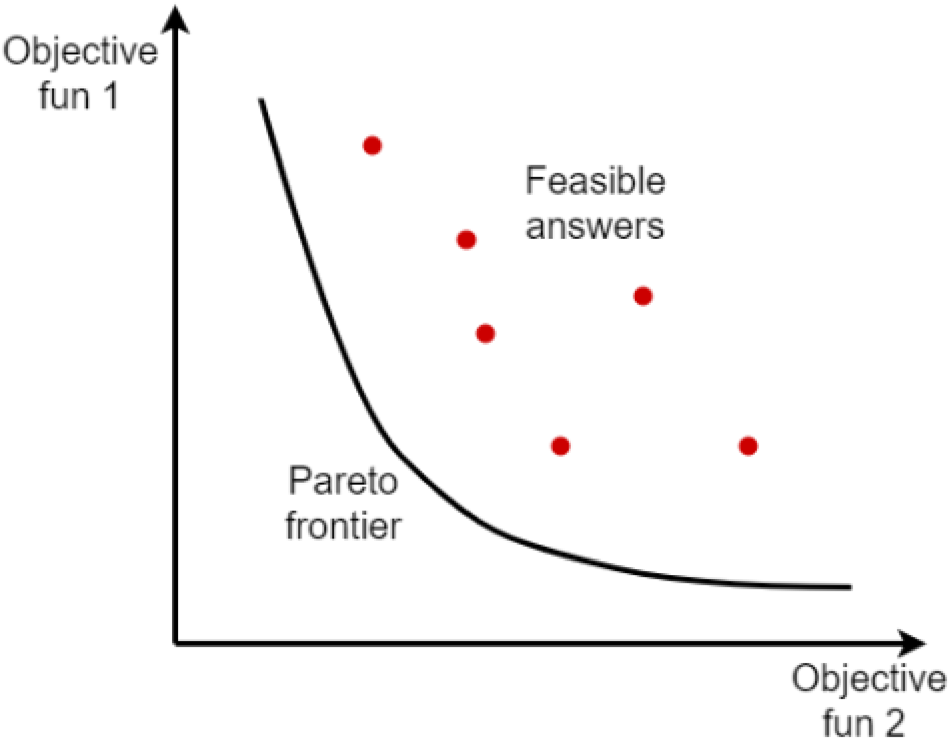

Figure 5.4: Pareto optimality.

Every single point on the optimal front is attributed to a set of particular decision variables [x], in which a better objective function cannot be found when the other one does not change. Therefore, a trade-off among the results is required to select one or a few particular points as the best decision. To choose an appropriate multi-objective optimisation algorithm, studies conducted by [34], [114] have been taken into account which emphasises that for the energy system like solar-powered gas turbine cycles the optimisation problems are non-linear and include several local minima and discontinuity. For the start-up optimisation of gas turbine cycles other studies by [115] and [86], also confirm the non-linearity of these problems. Therefore, evolutionary algorithms (EAs) are considered to be suitable tools for this kind of problem because of their robustness and their ability to find the global minimum. These algorithms mimic biological evolution and they are based on a natural selection process. They repeatedly modify a population of individual solutions. Generating new populations is continued until the population evolves toward an optimal solution.

5.1.5 Optimisation framework

The optimisation framework designed for this study is comprised of two main modules which are the transient model and the optimisation programme, Figure 5.5. The optimisation programme generates and modifies the values of the decision variables (defining parameters of the speed schedule). The transient model produces transient responses and the objective functions are calculated in a separate code for any sets of the given decision variables. Apart from the fact that the objectives are aimed to be minimised, not all of the objective functions which are calculated could be considered solutions. As was explained previously, there are some constraints that have to be implemented in the model or the optimiser. Since the model is developed in MATLAB/Simulink, the optimisation programme does not have direct access to the model. In order to calculate the objective functions and give them to the optimiser, the Simulink model is called in an m-file with one line code. When the simulation is finished in Simulink, the objective functions are calculated using the transient response of the electric power. The constraints are inserted in the Simulink model with this procedure so that when any limit is surpassed, the simulation stops. In this case, the calculated output (objective function) of the Simulink is allocated to be the maximum value of its possible value range. Consequently, these outputs are not taken into account as solutions and the new decision variables will be selected with respect to these deleted solutions.

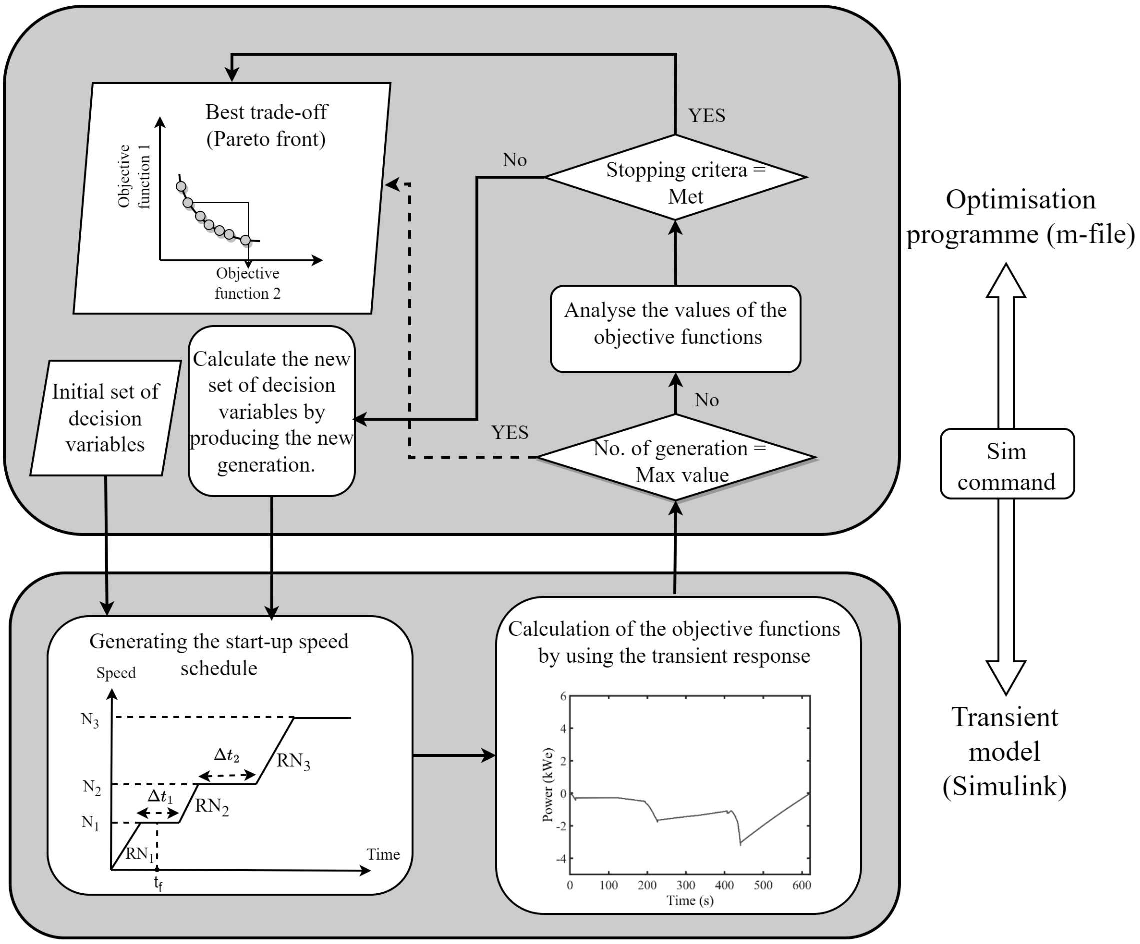

Figure 5.5: The diagram of the optimisation framework.

To create the first generation of the decision variables, the optimisation algorithm creates a random initial population with a uniform distribution. This ensures that the initial area of decision variables covers the whole decision space. Then, the optimisation programme analyses the values of the objective functions that have been calculated from the transient model. By using two main functions of mutation and crossover, the next generation is produced by modifying the previous generation. These two functions are responsible for providing selection pressure and population diversity for the modified generation, respectively. Selection pressure refers to the solutions with higher fitness value and population diversity refers to producing new generations from the whole design space that all of the feasible solutions could be considered.

5.2 Optimisation of the speed schedule of the start-up phase

The optimisation of speed schedules is performed for two primary types of start-up (cold and warm start-ups) and for three main objectives grouped into two sets: maximum required power and energy consumption, and energy consumption and start-up time. As previously mentioned, all three objective functions are interdependent, making single-objective optimisation inadequate. Therefore, in order to determine the optimal combination of objective functions for conducting multi-objective optimisation, it is necessary to comprehend their relationships. Calculating the maximum required power is essential to identify the highest value of the electric source for start-up, reducing the initial cost of the system. Furthermore, energy and power have conflicting relationships, which aligns with the principles of multi-objective optimisation. As a result, these two objective functions comprise the first set of optimisation. Afterwards, energy consumption and start-up time are optimised together to minimise energy consumption and start-up time.

5.2.1 Start-up maximum required power and energy consumption

The current research assumes that the CSP-MGT system functions in an off-grid capacity, with a focus on scenarios where it is situated in isolated areas without access to the national power grid. As a result, an external electric power source is necessary to start the system's operation, and any DC power source with enough capacity can be utilised for this purpose. It is necessary to determine the capacity of the DC source based on the CSP-MGT system's specifications, ensuring that it can provide sufficient electric power for the start-up phase. Choosing a smaller starter capacity can result in lower initial infrastructure costs. To determine the necessary capacity, it is first necessary to identify the DNI that necessitates the maximum power requirement, followed by identifying the type of start-up that necessitates the highest power. Therefore, optimisation was carried out for various DNIs with one start-up type (either cold or warm) to establish the previously stated situation. Figure 5.6 shows the Pareto fronts of different DNIs for a warm start-up.

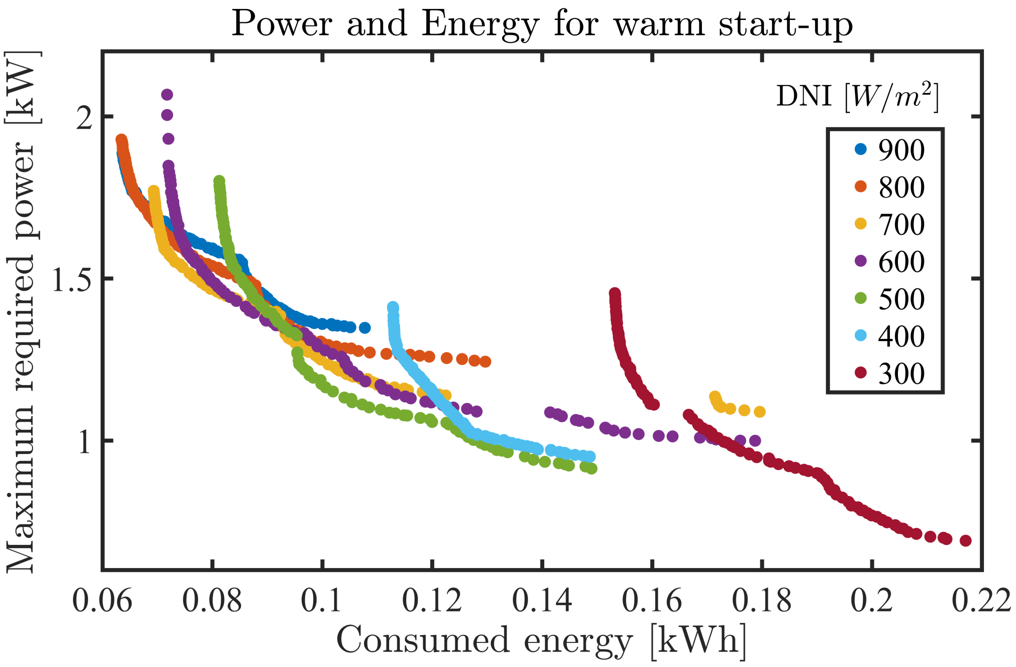

Figure 5.6: Pareto fronts of multi-objective optimisation of the maximum required power and energy consumption for warm start-up.

The figure presented in this analysis indicates that there is a positive correlation between the DNI value and the required maximum power. The rationale behind this finding is that as the DNI value increases, the rated speed of the system also increases, thereby necessitating a higher power requirement from the electric drive. This is due to the fact that power, which is primarily associated with the compressor power requirement, is related to the speed with the power of three, leading to a cubic growth in power when the speed is raised. While all Pareto-optimal solutions for DNI = 900 $[W/m^2]$ could potentially be utilised to establish a speed schedule, the solution with the highest power value on the frontier determines the necessary starter capacity. The maximum power requirement value on the frontier is approximately 2. However, to ensure safety during operation, a safety factor of 25% necessitated a starter capacity of 2.5. Incorporating an additional 0.5 [kW_e] into the determined starter capacity leading to a 25% increase is related to the range of the solutions found for the required power on the calculated frontier in Figure 5.7. This value (2.5 [kW_e] represents approximately 42% of the DC power generated under design conditions (6 [kW_e]). The investigation now turns to whether a cold start-up requires higher power than a warm start-up, given the observed relationship between DNI and required power. Figure 5.7 represents the Pareto front of DNI = 900 [W/m^2] for both warm and cold start-ups.

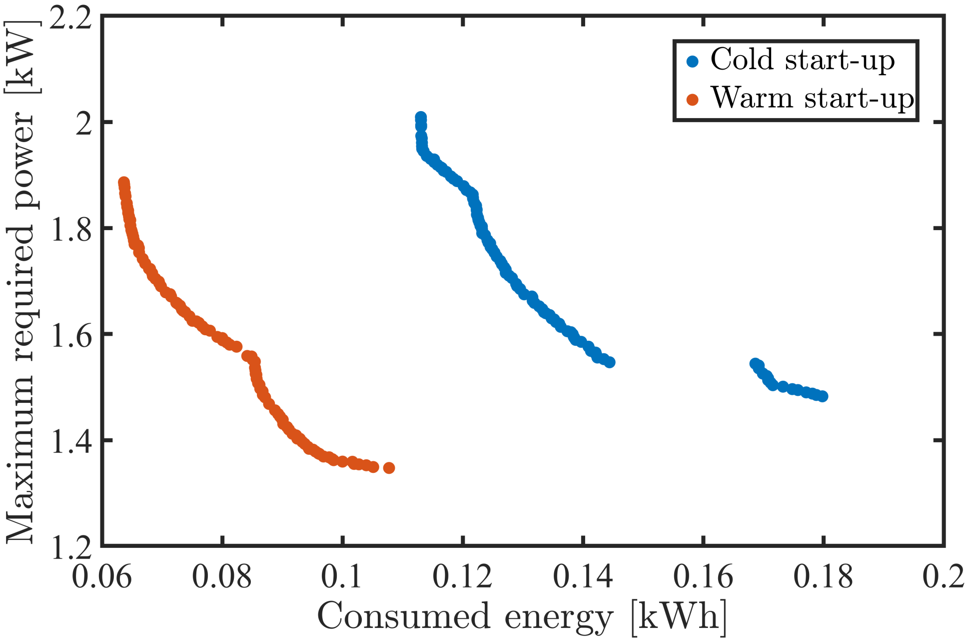

Figure 5.7: Pareto fronts of multi-objective optimisation of power and energy for warm and cold start-up for DNI =900 [W/m^2].

The figure presented in the analysis clearly indicates that the range of maximum required power for both warm and cold start-up types is similar. However, it is apparent from the figure that the maximum required power for a cold start-up is noticeably higher than that of a warm start-up for a given energy consumption. This implies that the previously chosen value for the starter capacity should remain unchanged. With the starter capacity established, it is used as a limiting factor in all subsequent simulations. This means that in the start-up procedure, the maximum power in the transient response of electric power cannot exceed 2.5 $[kW_e]$.

5.2.2 Start-up energy consumption and time

Having established the starter capacity as an added limitation to the system, the next step is to determine the optimal parameters for constructing a speed schedule, which can be achieved through another multi-objective optimisation. For a single value of DNI, the energy consumption is entirely dependent on the speed schedule (when all of the system specifications are constant). This same principle applies to the start-up time. But when the DNI value changes, the energy consumption and start-up time change as well. Figure 5.8 and 5.9 show the Pareto fronts for different DNI values for warm and cold start-ups, respectively. As it is obvious from the figure, both objective functions have higher values for lower DNI values. The main reason for this result is that when the DNI value is low, it takes more time for the solar receiver to be heated up. In these figures, the minimum DNI that is shown is 300 $[W/m^2]$ since generation starts from the DNI value of 260 $[W/m^2]$.

As is illustrated in the figure regarding the warm start-up, the minimum start-up time is associated with the DNI = 900 $[W/m^2]$ as the highest evaluated DNI with 400 seconds and the maximum start-up time is related to DNI = 300 $[W/m^2]$ as the lowest evaluated DNI which is about 1500 seconds. The interesting result is that when the DNI reduces to 300 $[W/m^2]$, the Pareto front is placed significantly further than the rest of the Pareto fronts which stems from the fact that it takes a longer time for the system to reach a self-sustaining point. As it is shown in Figure 5.9, the same behaviour is depicted with different DNI values for cold start-up. This behaviour can be attributed to the reduced rate of temperature increase caused by the low thermal input power, as well as the low air mass flow rate, resulting in decreased

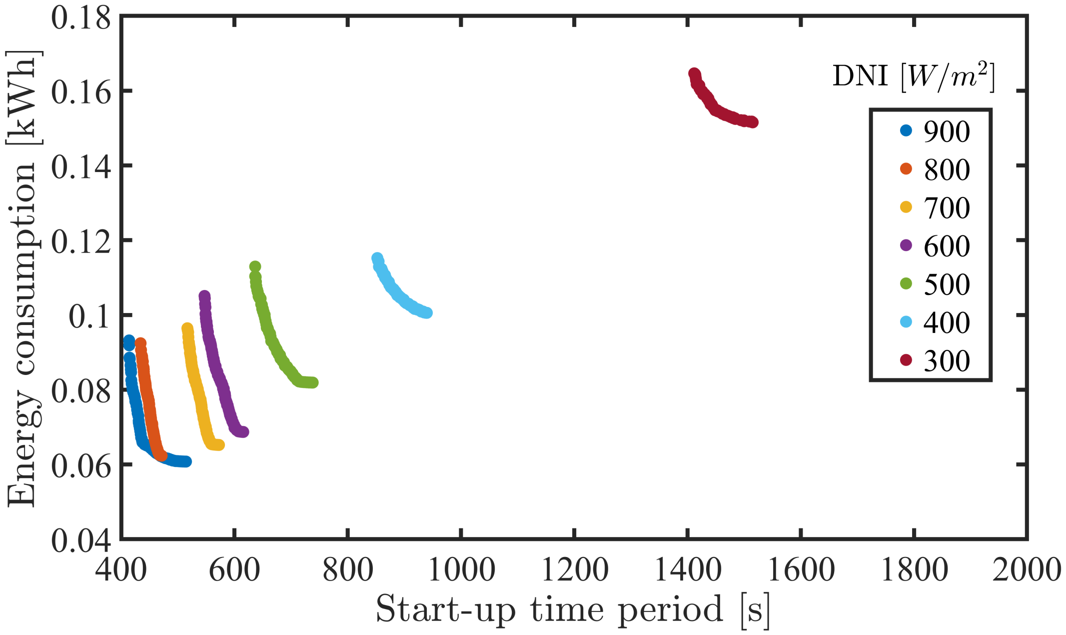

Figure 5.8: Multi-objective optimisation Pareto fronts for warm start-up energy consumption and time with varying DNI values.

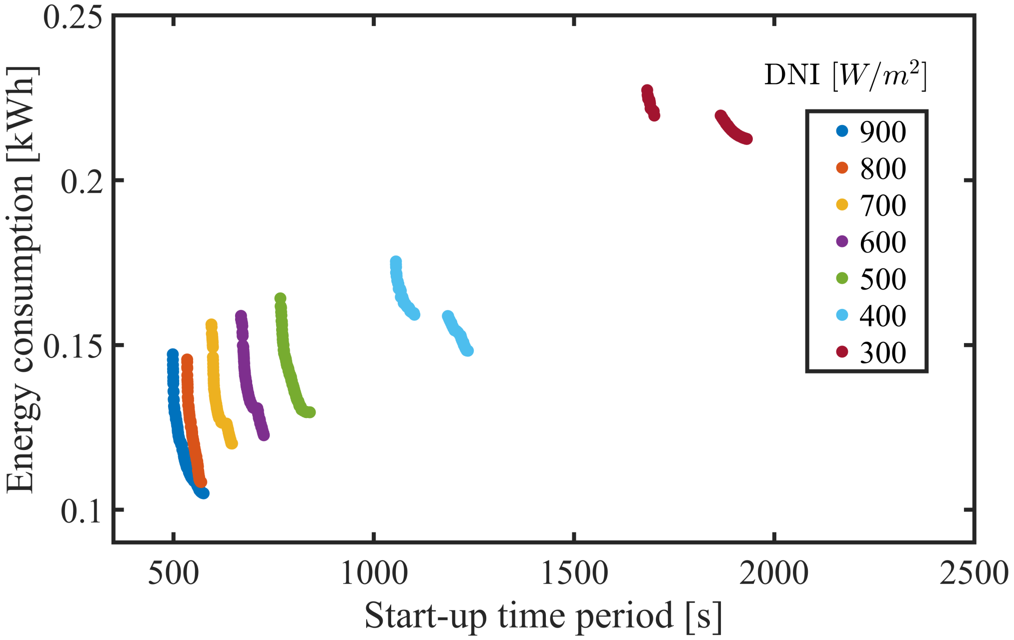

Figure 5.9: Multi-objective optimisation Pareto fronts for cold start-up energy consumption and time with varying DNI values.

thermal energy absorption. The amount of energy that is consumed during the start-up for all cases ranges from 0.06 to 0.24 $[kWh]$.

After the Pareto fronts are produced for various DNI values, a solution must be selected for each DNI for the two start-up types. In the cases that the DNI value is high, a strategy different from the ones with low DNI values could be taken for selecting the solution of speed schedule. In these cases, similar to the consumed energy during start-up that is lower than in the cases with lower DNIs, the produced energy during the generation mode could be higher than in the case with lower DNI values. Therefore, it is better to choose the case in which the motoring mode takes the shortest time which causes the energy consumption to have the highest value, instead, it leaves a longer time for the power generation. However, it should be evaluated whether it is worth or not consuming the maximum energy consumption among the solutions on the Pareto front during motoring mode to reach the generation point in a shorter time or not. This evaluation has been only done for warm start-up which is also applicable for cold start-up. In order to find the best solution on the Pareto front, a new parameter is defined which is called modified energy consumption, Equation 5.6.

$$En_{mf} = En_{mot} - En_{gen,\Delta t} \tag{5.6}$$

where En_{mf}, En_{mot} and $En_{gen,\Delta t}$ are modified energy consumption, energy consumption before the self-sustaining point and produced energy during the generation period. This parameter has been defined by subtracting the potential energy that can be produced if the system goes beyond the self-sustaining point for Δt seconds from the energy consumption of a point on the Pareto front (En_{mot}. The term Δt is the difference between the maximum start-up time on the Pareto front and the associated start-up time of En_{mot}. Figure 5.10 provides a visual explanation of these parameters.

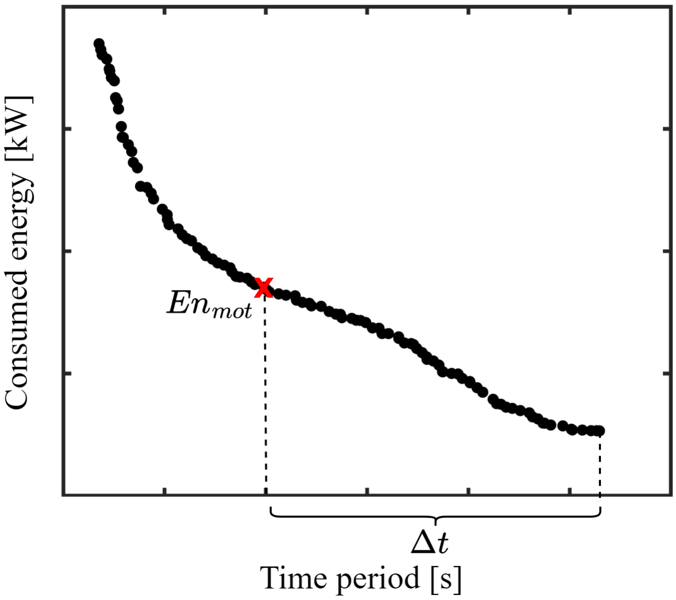

Figure 5.10: Representation of the energy consumption of CSP-MGT during start-up and finding the best solution for high DNI values according to final energy consumption.

The parameter of En_{mf} was used to see whether by selecting a solution that has a higher value for energy consumption and lower start-up time, the final energy consumption (En_{mf}) becomes less than the solutions with lower energy consumption values on the frontier. Since the DNI value is high, it was expected that the sooner the system begins generation, the less energy is consumed. Therefore this type of computation has been done for DNI =900, 800 and 700 and the result for only DNI=900 is shown in Figure 5.11. As can be observed from the figure, the Pareto front that includes saved energy has lower values for consumed energy in a way that one solution on the original Pareto front (blue curve) in spite of consuming higher energy than the case with the longest start-up time, saves more energy due to reaching self-sustaining point sooner. In that case, the high value of DNI allows the system to produce enough energy that it compensates for the amount used during the motoring mode.

Therefore, for the DNI value of 900 [W/m^2] the solution that results in the same energy consumption as the solution with the shortest time, is chosen. This strategy has been used for the rest of the cases with high DNI values. If the results were not the same as DNI=900

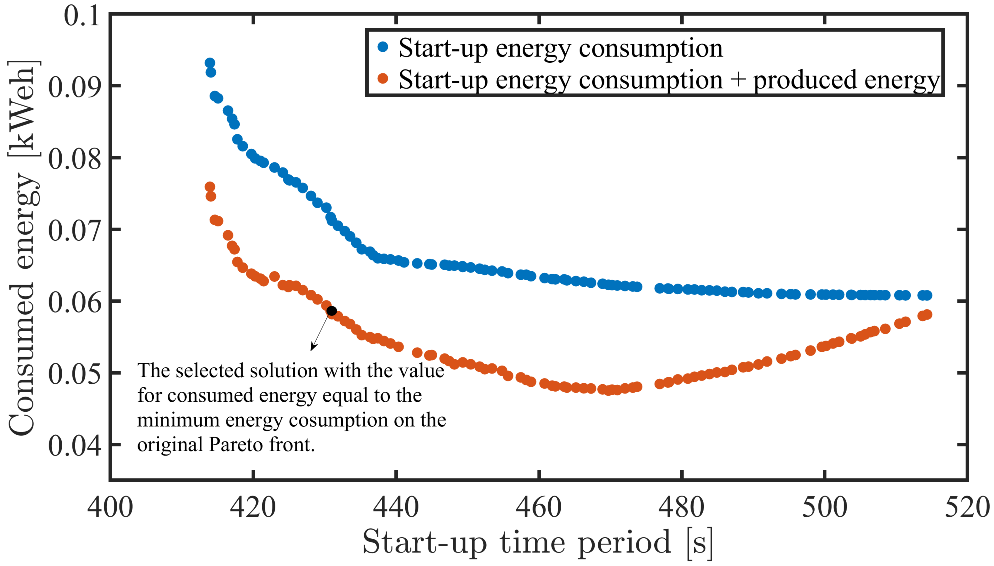

Figure 5.11: The comparison between the solutions for DNI=900 [W/m^2] for two cases of only including motoring mode energy consumption and the case of including produced energy.

[W/m^2] and the Pareto front including the saved energy is not significantly different from the original Pareto front, depending on the values of the start-up time and energy consumption, an appropriate solution was chosen. Firstly, it must be mentioned that based on the Pareto fronts found for all of the DNI values, the maximum difference in the start-up time on the frontier was about 120 seconds for a warm start-up which is a significant value for the high DNI values where the average start-up time is about 400 seconds. However, it is low for the low DNI values. For the cold start-up, this maximum difference is about 250 seconds. If the difference between the solutions of maximum and minimum start-up time is very low (lower than one minute), then the solution with the lowest energy consumption was chosen, especially for the cases where the whole start-up time is about 500 seconds which happens for the higher DNI values. However, for the low DNI values, choosing the least energy consumption is better since the start-up time is very long and if the maximum difference in the start-up time on the Pareto front is about 60 seconds, this selection becomes more logical due to the longer start-up time. In the cases where the solutions on the Pareto front are very close to each other for the two objectives (especially for the energy consumption), it was tried to select a solution which is a trade-off among the two objective functions.

In general, for all of the DNI values of the warm and cold start-up, the Pareto fronts with three candidate solutions are shown from Figure 5.12 to 5.19. In these figures, the Pareto front along with the previous generations of optimisation are shown. The algorithm converged after almost 100 generations for all of the DNI values. The results in the last generation, form a Pareto front. The population of the Pareto front solutions are chosen to be 105 (35 % of the total population for each generation). It can be observed from the provided Pareto fronts that the solutions on the frontiers are showing about 60% less energy consumption with approximately 60% less start-up time as well, compared with the rest of the solutions. This means that by using the speed schedules extracted from the selected solutions on the frontier, the start-up consumed energy and start-up time could be 60% less than the potential values which is a significant amount. However, since there was no pre-selected solution to compare the found schedules with, they are compared with the potential solutions which are based on the range of each speed schedule parameter defined in the previous chapter.

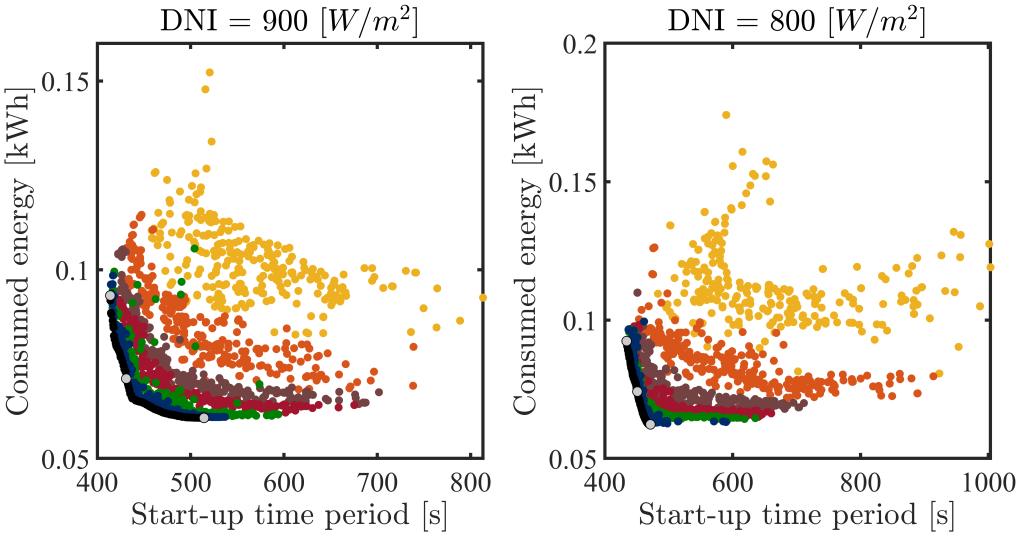

Figure 5.12: Evolution of the optimisation results towards Pareto front for warm start-up under DNI = 900 $[W/m^2]$ and DNI = 800 $[W/m^2]$.

The results of selected solutions for warm and cold start-up modes are also expressed as

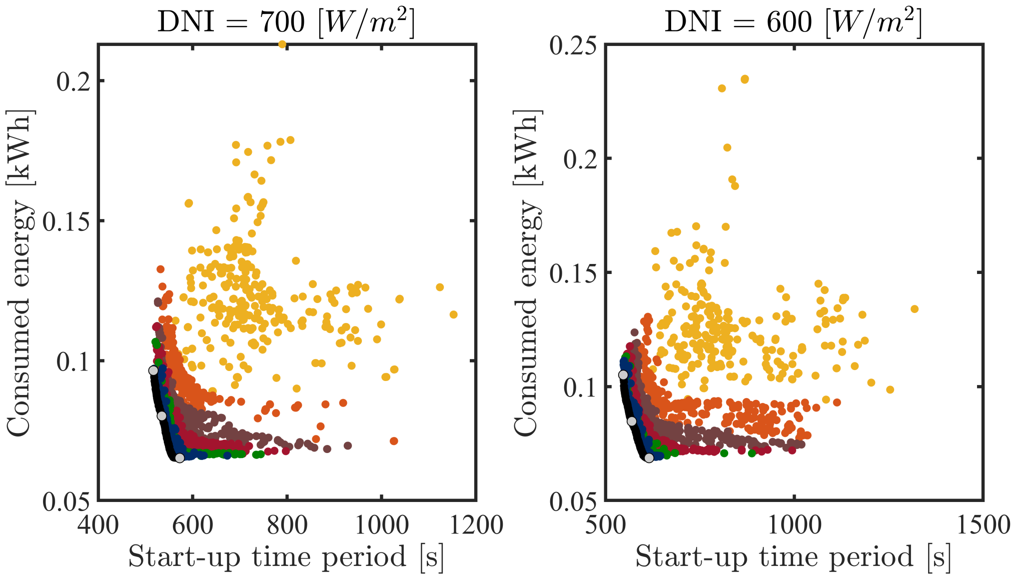

Figure 5.13: Evolution of the optimisation results towards Pareto front for warm start-up under DNI = 700 $[W/m^2]$ and DNI = 600 $[W/m^2]$.

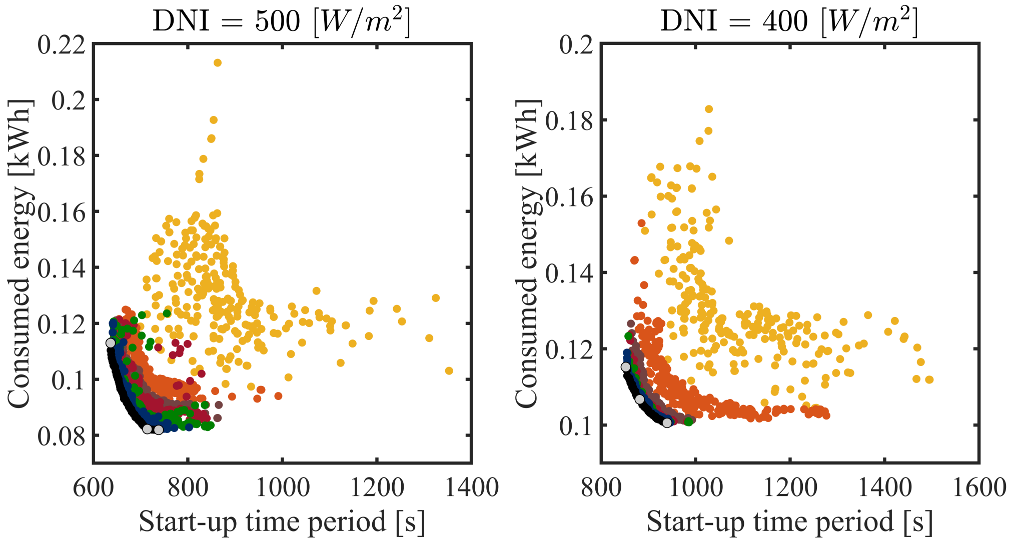

Figure 5.14: Evolution of the optimisation results towards Pareto front for warm start-up under DNI = 500 $[W/m^2]$ and DNI = 400 $[W/m^2]$.

relative values by dividing the original values over reference values, for each DNI. Tables 5.4 and 5.5 present the selected solutions and their corresponding relative values, respectively. The reference value of energy consumption for each DNI is determined based on the minimum start-up time which is obtained through the optimisation of the DNI value. The rated generated power associated with the steady-state mode multiplied by the regarding start-up time (the

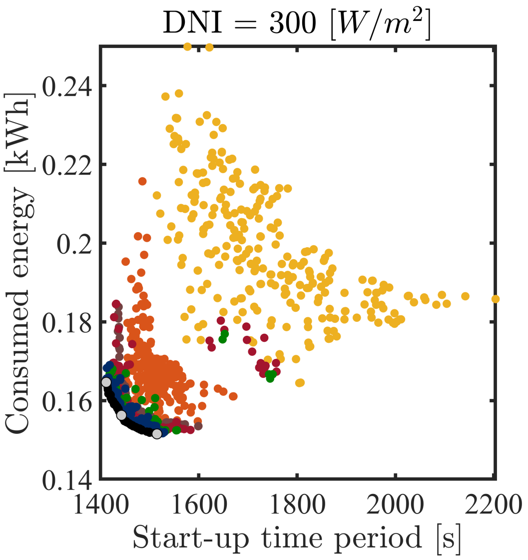

Figure 5.15: Evolution of the optimisation results towards Pareto front for warm start-up under DNI = 300 $[W/m^2]$.

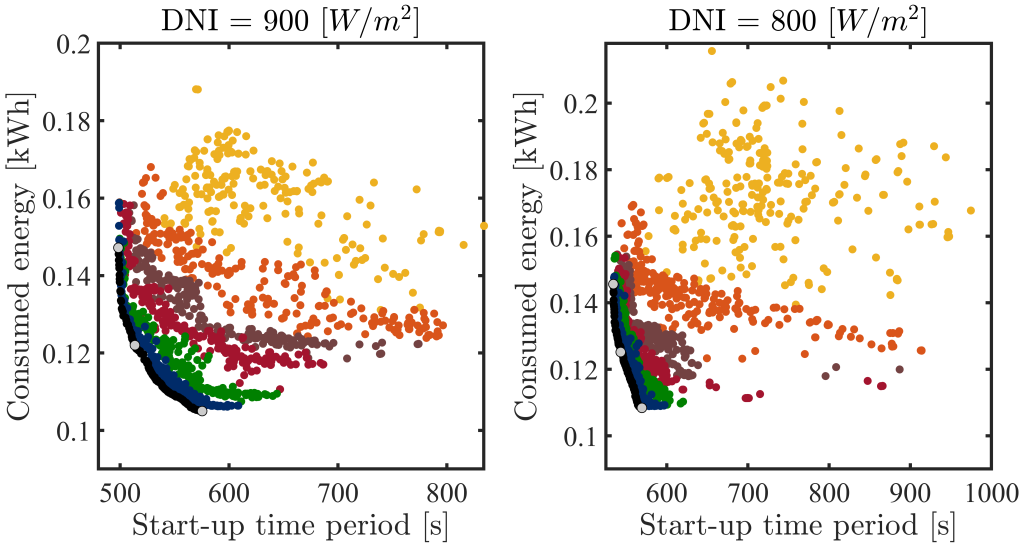

Figure 5.16: Evolution of the optimisation results towards Pareto front for cold start-up under DNI = 900 $[W/m^2]$ and DNI = 800 $[W/m^2]$.

minimum found start-up time on the frontier) is used to derive the reference value of energy consumption. The expression of the relative energy consumption is defined by Equation 5.7. It is noted that the reference value of energy consumption varies for each DNI, and indicates the amount of energy consumption produced by the system when operating in generation mode for the minimum value of the start-up time found from the optimisation procedure.

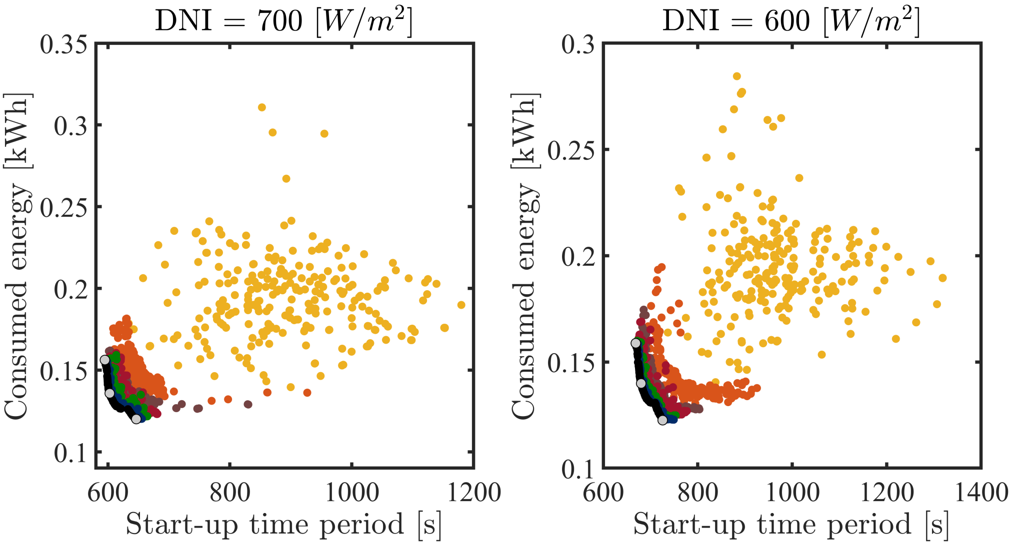

Figure 5.17: Evolution of the optimisation results towards Pareto front for cold start-up under DNI = 700 $[W/m^2]$ and DNI = 600 $[W/m^2]$.

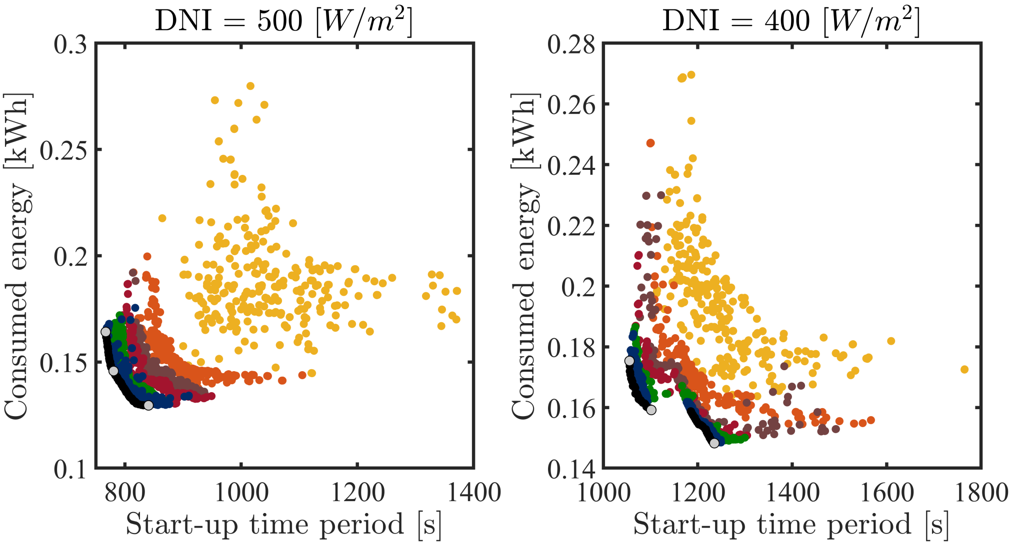

Figure 5.18: Evolution of the optimisation results towards Pareto front for cold start-up under DNI = 500 $[W/m^2]$ and DNI = 400 $[W/m^2]$.

$$En_{ref} = PW_{rated}.ST_{min,DNI} \tag{5.7}$$

where PW_{rated} and $ST_{min,DNI}$ are the rated power according to the related DNI and minimum value of the start-up time which is found from the Pareto front of the associated DNI and

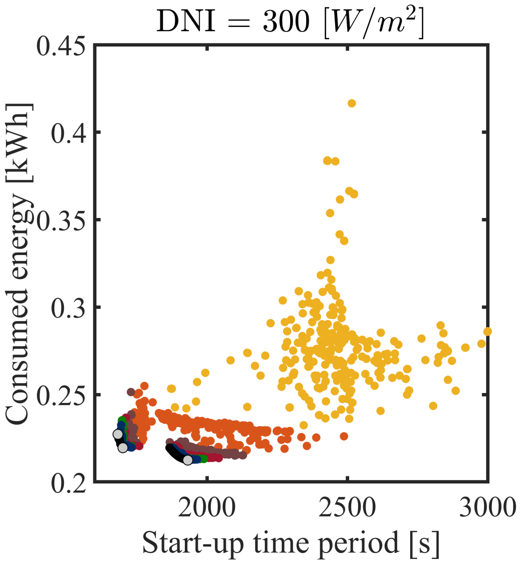

Figure 5.19: Evolution of the optimisation results towards Pareto front for cold start-up under DNI = 300 $[W/m^2]$.

it is called reference start-up time. The reference values for energy consumption and start-up time for each DNI value and for both warm and cold start-ups are shown in Table 5.2 and 5.3.

DNI $[W/m^2]$	900	800	700	600	500	400	300
En_{ref} $[kWh]$	0.53	0.48	0.43	0.33	0.27	0.20	0.10
ST_{ref} $[s]$	414	434	517	547	637	852	1412

Table 5.2: The reference values of the energy consumption and start-up time for each DNI for a warm start-up.

DNI $[W/m^2]$	900	800	700	600	500	400	300
En_{ref} $[kWh]$	0.64	0.58	0.5	0.40	0.32	0.25	0.12
ST_{ref} $[s]$	498	534	595	669	767	1056	1683

Table 5.3: The reference values of the energy consumption and start-up time for each DNI for a cold start-up.

The results presented in figures 5.20 and 5.21 demonstrate that an increase in DNI results in a decrease in energy consumption. Additionally, the ratio of energy consumption during the start-up phase to the potential energy production when the system operates at its rated power (relative energy consumption) also decreases. For the DNI value of 300 $[W/m^2]$, it is seen that the consumed energy during the start-up is even more than the case it could generate power

	DNI = 900 $[W/m^2]$				DNI = 800 $[W/m^2]$			
	En $[kWh]$	En_{rel} $[\%]$	ST $[s]$	ST_{rel} $[\%]$	En $[kWh]$	En_{rel} $[\%]$	ST $[s]$	ST_{rel} $[\%]$
Solution 1	0.0932	17.5	414	100.0	0.0924	19.3	434	100
Solution 2	0.0712	13.4	431	104.1	0.0742	15.5	451	103.9
Solution 3	0.0608	11.4	514	124.3	0.0624	13.1	471	108.6
	DNI = 700 $[W/m^2]$				DNI = 600 $[W/m^2]$			
Solution 1	0.0964	22.2	517	100.0	0.1051	31.4	547	100.0
Solution 2	0.0803	18.7	535	112.2	0.0847	25.3	570	104.1
Solution 3	0.0652	15	573	110.8	0.0687	20.6	615	112.5
	DNI = 500 $[W/m^2]$				DNI = 400 $[W/m^2]$			
Solution 1	0.1129	42.2	637	100.0	0.1152	56.3	852	100.0
Solution 2	0.0822	30.7	714	112.2	0.1067	52.2	882	103.5
Solution 3	0.0819	30.6	738	116.0	0.1006	49.2	940	110.3
	DNI = 300 $[W/m^2]$							
Solution 1	0.1646	164.6	1410	100.0				
Solution 2	0.1563	156.3	1443	102.2				
Solution 3	0.1515	151.2	1520	107.3				

Table 5.4: Candidate solutions in addition to the selected solution (red coloured values) for each DNI according to their frontiers for a warm start-up.

in the start-up period. This result indicates that the start-up process is more costly when DNI values are low compared to when they are high. This implies that when the thermal power input decreases, CSP-MGT utilises a greater proportion of the available energy production if it operates at its maximum power generation capacity.

5.2.3 Evaluation of the optimised speed schedules

Based on the results in the previous section, for each DNI of both warm and cold start-ups, a solution which was a trade-off between energy consumption and start-up time was chosen. Figure 5.22 to 5.28 represents chosen speed schedule with the focus time and the beginning of the power generation (self-sustaining point) with a dashed line. According to the findings, the recommended start-up procedure for a CSP-MGT involves a multi-stage schedule rather than a single ramp. This is because a single ramp was not deemed a feasible solution in the

	DNI = 900 $[W/m^2]$				DNI = 800 $[W/m^2]$			
	En $[kWh]$	En_{rel} $[\%]$	ST $[s]$	ST_{rel} $[\%]$	En $[kWh]$	En_{rel} $[\%]$	ST $[s]$	ST_{rel} $[\%]$
Solution 1	0.1472	23.0	498	100.0	0.1456	22.1	534	100.0
Solution 2	0.122	19	514	103.0	0.1252	19	544	102
Solution 3	0.105	16.4	575	115.7	0.1084	16.4	569	107
	DNI = 700 $[W/m^2]$				DNI = 600 $[W/m^2]$			
Solution 1	0.1562	31.2	595	100.0	0.1588	38.9	669	100.0
Solution 2	0.1359	27.2	603	101.3	0.1399	34.2	680	101.7
Solution 3	0.1201	24.0	646	108.5	0.1226	30	726	108.5
	DNI = 500 $[W/m^2]$				DNI = 400 $[W/m^2]$			
Solution 1	0.1642	50.9	767	100.0	0.1754	69.2	1060	100
Solution 2	0.1458	45.2	781	101.8	0.1592	62.8	1102	104.4
Solution 3	0.1296	40.2	841	109.6	0.1483	58.5	1240	117.0
	DNI = 300 $[W/m^2]$							
Solution 1	0.2273	190.7	1683	100.0				
Solution 2	0.2196	184.2	1701	210.6				
Solution 3	0.2125	178.3	1932	114.8				

Table 5.5: Candidate solutions in addition to the selected solution coloured in red for each DNI according to their frontiers for a cold start-up.

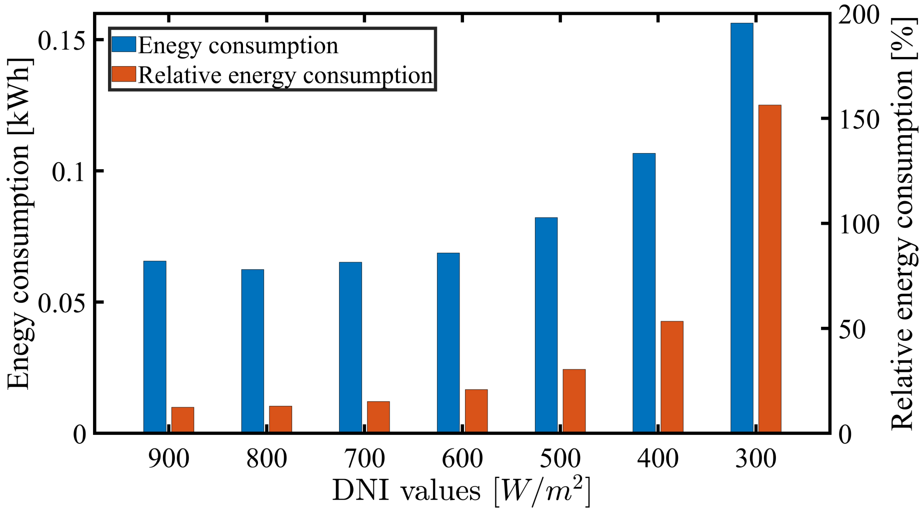

Figure 5.20: Consumed energy during a warm start-up for different DNI values in two absolute and relative forms.

optimisation outcome. When the solar receiver fails to heat up due to an increasing speed, the electric drive becomes the primary energy source for start-up, potentially exceeding the

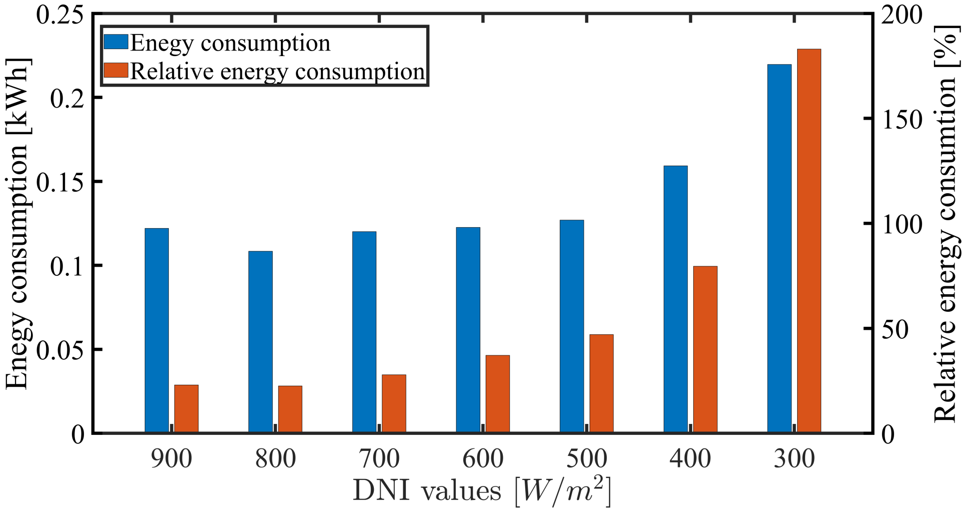

Figure 5.21: Consumed energy during a cold start-up for different DNI values in two absolute and relative forms.

electric current limit. As such, even for low DNI values where the rated speed is lower than the drive's maximum speed capacity, the simple single ramp or two ramps approach was not chosen. Additionally, it has been discovered that in order for the shaft to attain the rated speed according to the DNI value, the speed schedule must include two periods of stationary speeds. Even though it was possible for the shaft speed to increase straight from N_1 to the final rated speed, this approach was not selected during the optimisation process.

As can be clearly observed from the selected schedules, CSP dish focusing happens at the early beginning of the start-up phase immediately after the shaft speed reaches N_1 with a few seconds delay in some cases. This timing happens for both cold and warm start-ups and for all DNI values. This result has been also deduced from the sensitivity analysis earlier. The duration for which the shaft speed remains constant (Δt_1) during a cold start-up at speed N_1 is the same as or greater than that required for a warm start-up. This is also seen for Δt_2 where the speed of N_2 remains constant. Another interesting result is that the commencement of self-sustaining point takes place at the rated speed in all cases. In contrast to fuelled MGTs, where self-sustainability is achieved at a speed lower than the rated value, CSP-MGTs utilise a distinct control approach that prevents the system from achieving self-sustainability before reaching the final speed. This distinction arises because, in CSP-MGTs, speed is directly regulated, as opposed to being indirectly managed through fuel flow in fuelled ones. Consequently, during the initial phase of CSP-MGT start-up, when power generation begins at a speed below the rated value, the speed is subsequently augmented to attain the designated value. This, in turn, necessitates additional power from battery or the external source. In addition to that, the beginning of the power generation is clearly later for the cold start-up for all of the cases in comparison with the warm start-up.

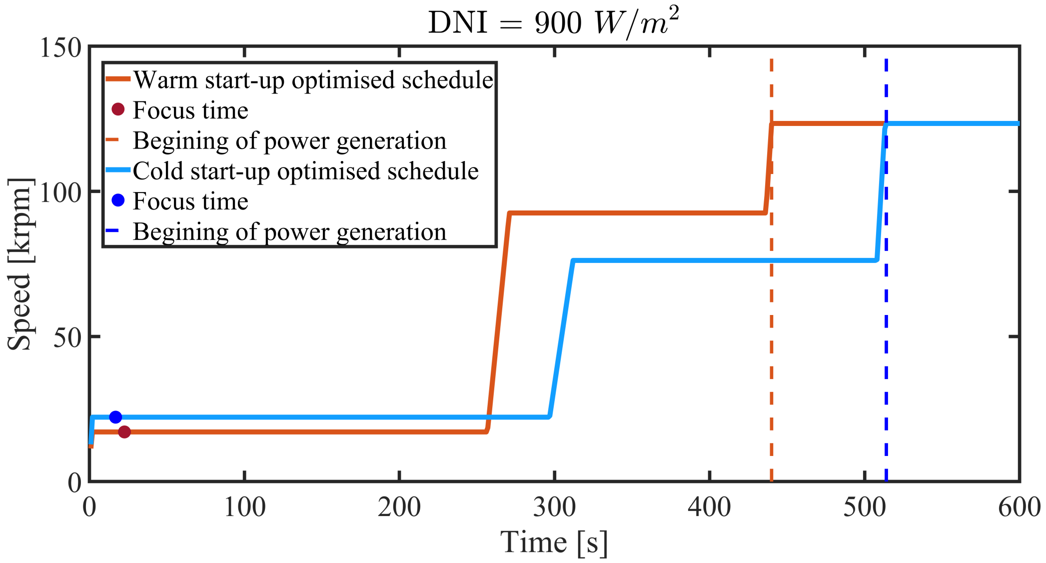

Figure 5.22: Optimised speed schedules for both warm and cold start-ups for DNI =900 $[W/m^2]$.

The speed schedules indicate that to achieve minimum energy consumption during the start-up, the speed schedule parameters should have a range of values, and some of these parameters appear to exhibit a pattern. To investigate this matter, four non-dimensional terms were defined for the four primary schedule parameters, namely N_1, N_2, Δt_1, and Δt_2 for each DNI. The speed values were normalised by the rated speeds of their respective DNI, and the time parameters were normalised by the start-up time of the corresponding DNI, resulting in N^* and Δt^*.

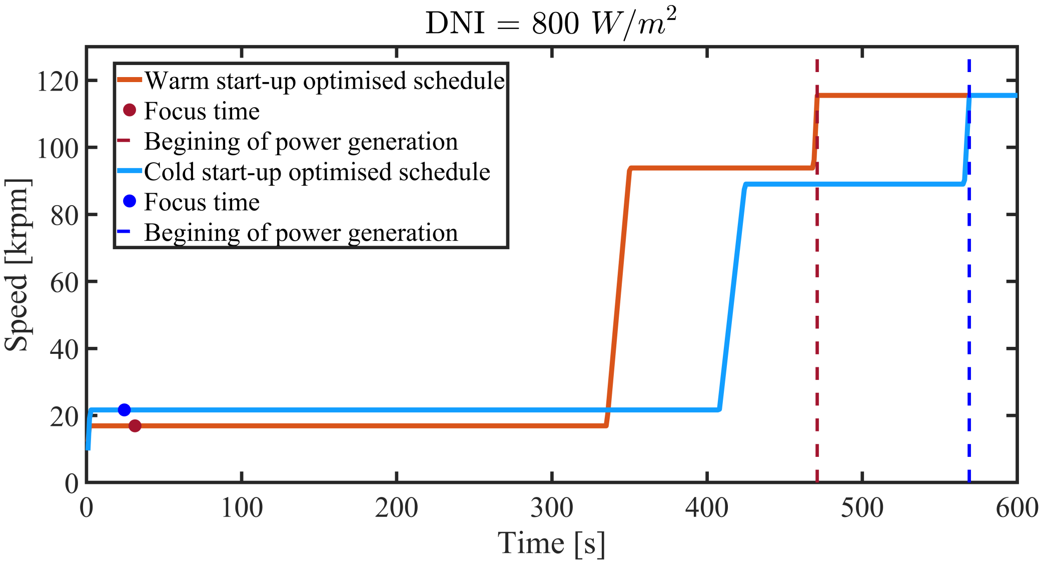

Figure 5.23: Optimised speed schedules for both warm and cold start-ups for DNI =800 $[W/m^2]$.

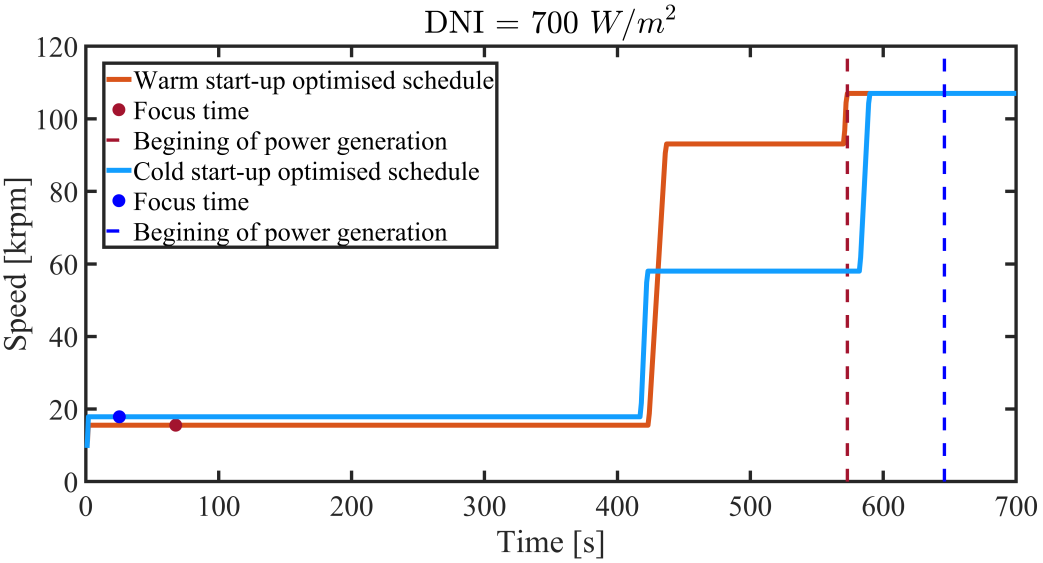

Figure 5.24: Optimised speed schedules for both warm and cold start-ups for DNI =700 $[W/m^2]$.

$$N_1^* = \frac{N_1}{N_3}.100 \quad and \quad N_2^* = \frac{N_2}{N_3}.100 \tag{5.8}$$

$$\Delta t_1^* = \frac{\Delta t_1}{STime}.100 \quad and \quad \Delta t_2^* = \frac{\Delta t_2}{STime}.100 \tag{5.9}$$

where $STime$ is the start-up time for the selected solution according to a specific DNI value and start-up type.

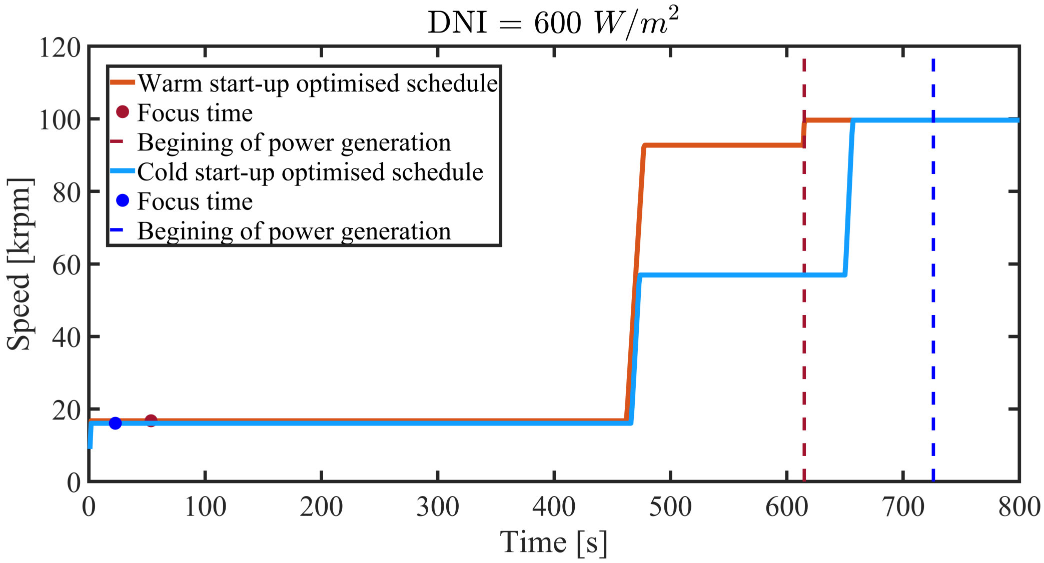

Figure 5.25: Optimised speed schedules for both warm and cold start-ups for DNI =600 $[W/m^2]$.

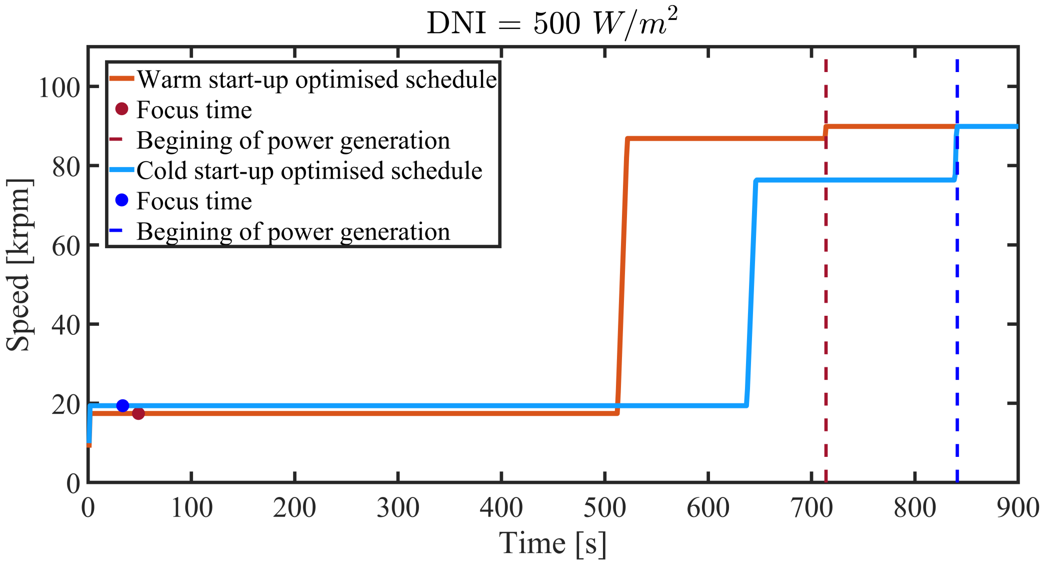

Figure 5.26: Optimised speed schedules for both warm and cold start-ups for DNI =500 $[W/m^2]$.

Figure 5.29 and 5.30 show the four selected parameters in relative form for both warm and cold start-ups.

Figure 5.29 depicts that the non-dimensional parameter of N_1 attains a peak value at a DNI of 300 $[W/m^2]$ and exhibits a minimum value at a DNI of 900 $[W/m^2]$. Nevertheless, the actual speed of N_1 appears to remain uniform across all DNI values, with a maximum deviation

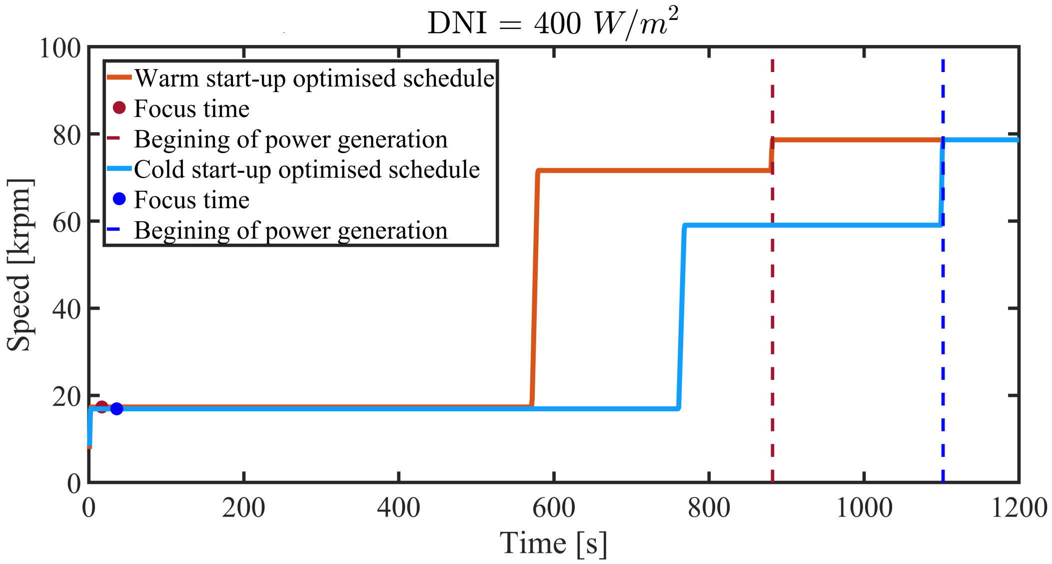

Figure 5.27: Optimised speed schedules for both warm and cold start-ups for DNI =400 $[W/m^2]$.

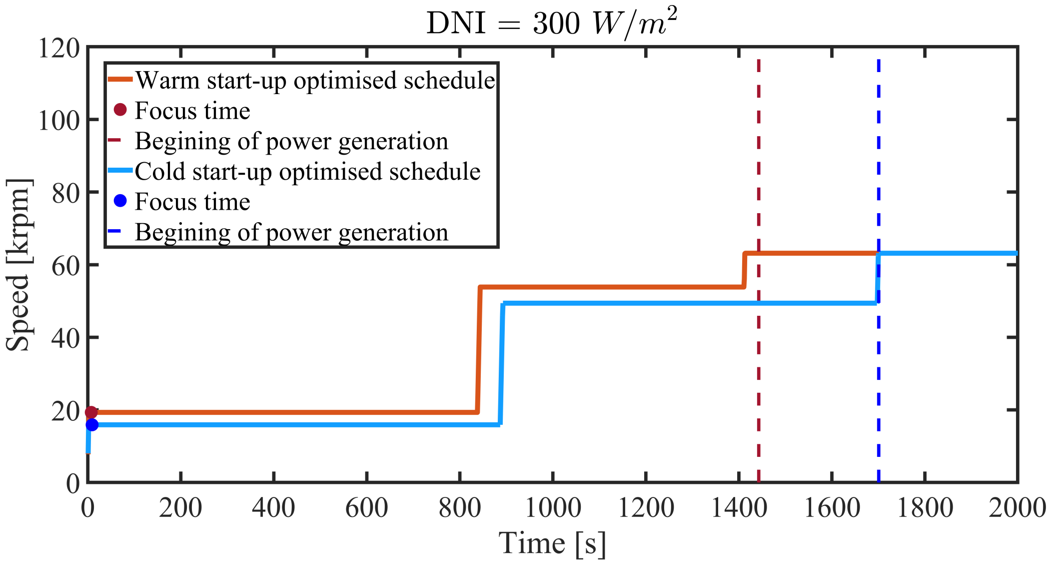

Figure 5.28: Optimised speed schedules for both warm and cold start-ups for DNI =300 $[W/m^2]$.

error of 4% from the average speed of 17 [krpm]. But due to the higher rated speed for higher DNI values, the relative value becomes lower as DNI increases. This speed is the first speed that the MGT shaft reaches and remains constant for a while until the next ramp starts for speed increasing. Due to the low value of this speed compared with the rated speed, the power required for increasing the shaft speed to this target is not very significant and since the time that it takes for the speed to reach this target is very short (in the order of seconds), the energy

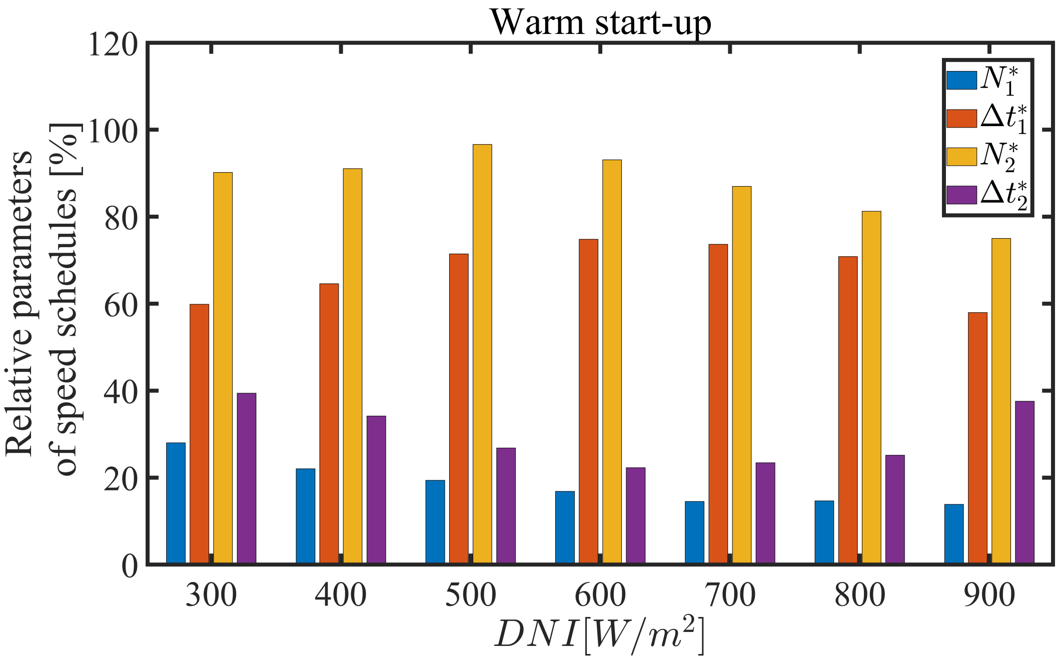

Figure 5.29: Four main parameters of the speed schedules in relative form for a warm start-up.

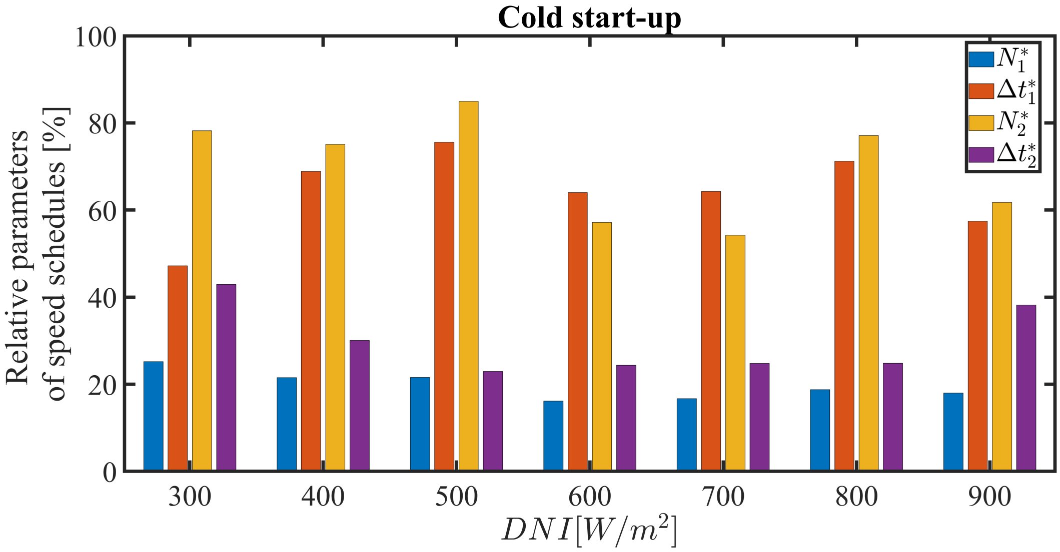

Figure 5.30: Four main parameters of the speed schedules in relative form for cold start-up

consumed in this part of the start-up is negligible. Therefore, it can be a valid statement that we use the average relative value for the N_1 speed and have a conclusion from the results. Although the standard deviation from the average value of $N_1{}^*$ is 28%, it can be concluded that $N_1{}^*$ is better to be 18 % of the rated speed for a warm start-up (which is a type that is more likely to happen during the day). The second speed, however, has great importance due to the fact that the power required which belongs to the compressor, is proportional to the speed with the power of three and the value of this speed strongly affects the energy consumption as well. The relative value of N_2 is 88% of the rated speed with a standard deviation error of 8.4%.

As it is represented in the figure, the first time interval that the system standstills is significantly longer than the second time interval. This is due to the reason that the air mass flow rate has to remain constant with a low value to leave enough time for the solar receiver to warm up and continue for the rest of the start-up. One common thing among all of the relative values for Δt_1 is that they are all higher than 60% of the whole start-up period which is very significant. On the other hand, the other time interval is shorter than the first one. However, there is no specific pattern for the value of this time interval and it is defined based on the DNI value and the type of the start-up. Figure 5.30 shows the same parameters for cold start-up. A similar conclusion can be deduced from the speed schedule parameters of the cold start-up with different values.

5.3 Conclusions

The primary aim of this chapter was to develop a framework for the optimisation of the start-up schedule of the CSP-MGT system. The objective was to find an optimised start-up schedule that minimises the energy consumption, maximum required power, and time during the motoring mode while ensuring that the overall system's safety is provided. To demonstrate the importance of optimisation, a sensitivity analysis was conducted. The analysis revealed that for most decision variables, setting maximum and minimum bounding limits could lead to the system's constraints being exceeded. Further technical conclusions are listed below.

- The DNI value directly correlates with the power required for start-up, with cold-start-ups demanding more power compared to warm start-ups. Consequently, the maximum required power, determining the starter capacity (in this case, the battery), was determined through the optimisation of cold start-ups for the objectives of maximum required power and energy consumption. The optimised capacity was found to be approximately 42% of the DC power generated in the case of nominal power generation of PMSM (6 [kW_e]), representing the maximum power point on the frontier of the Pareto front.

- Through optimisation, speed schedules were derived to simultaneously minimise energy consumption and start-up time, revealing a direct relationship between lower DNI values and increased energy consumption. For instance, at DNI = 300, the energy consumption nearly doubles that at DNI = 900 due to a slower rate of temperature rise. Conversely, higher DNI values result in shorter start-up times. Warm start-ups at DNI = 300 take roughly four times longer (1600s) to reach generation than DNI = 900 (400s). This indicates that 30 minutes are needed to achieve generation at a constant DNI of 300, requiring an equal or higher amount of time to compensate for consumed energy during start-up.
- The optimisation results, showcased for various DNI values and both types of start-ups, revealed that the solutions on the frontier achieved around a 60% reduction in energy consumption and a similar reduction in start-up time compared to the remaining potential solutions. Although a direct benchmark for comparison was not provided, these outcomes are essential in establishing an effective speed schedule for a CSP-MGT.
- As the DNI value decreases, the ratio of energy consumption during start-up to potential energy production (when the CSP-MGT operates in generation mode at maximum power generation rating) also increases.
- The optimised speed schedules for the CSP-MGT system indicate that a minimum of three steps is necessary. While a two-step schedule could have been considered, the find-

ings highlight the importance of incorporating at least three steps in the speed schedule.

- Parabolic dish focusing occurs right at the beginning of the start-up process, immediately after the shaft speed reaches N_1, irrespective of whether it is a cold or warm start-up.
- The self-sustaining point for CSP-MGT systems during their startup phase is reached at the rated speed, unlike fuelled MGTs, where this point is achieved at a speed below the rated value. This distinction is attributed to the unique control strategy employed for CSP-MGTs.
- For both cold and warm start-ups, the first speed at which the shaft remains constant (N_1) was set at 17 [krpm], regardless of the DNI values. The second constant shaft speed (N_2) was determined to be 88% of the rated speed, with a standard deviation error of 8.4% for both warm and cold start-ups. The duration of Δt_1, which represents the time during which N_1 remains constant, was found to be over 60% of the entire start-up duration for both types of start-ups. However, there was no consistent pattern observed for Δt_2 among the various DNI values, except that it was always shorter than Δt_1 in all cases.
- In every instance, the surge margin was higher than the acceptable threshold of 15%. This indicates that additional measures, such as incorporating a bleed valve similar to those used in heavy-duty gas turbines, were unnecessary.

The optimal speed schedules obtained in this chapter will be employed to assess the performance of the CSP-MGT system on an annual basis in the next chapter.

Chapter 6

Evaluation of the CSP-MGT start-up on an annual basis

In previous chapters, the focus was solely on evaluating the start-up phase of the CSP-MGT for various DNI values. Efforts were made to optimise the start-up procedure in order to minimise the maximum required power, energy consumption, and start-up time. The optimisation procedure also considered the safety of the whole system by defining safety criteria as constraints. The optimisation was only done under the assumption that the DNI value remained constant throughout the start-up phase. However, due to the intermittent nature of solar energy, it is clear that the DNI can change rapidly even in a single second. As a result, a single speed schedule cannot be used during the start-up phase before power generation begins. This also applies during the generation phase. If the received solar energy decreases to a low DNI value, where no power can be generated, the system may need to go through the start-up process again if the next DNI value is sufficient for power generation. Furthermore, the start-up phase involves the consumption of energy and unlike the generation phase, they are considered a cost factor instead of a profit. As a result, it is necessary to conduct an annual analysis to determine the net electricity produced over the course of a year and to take into account the system's behaviour on different days with varying DNI values.

6.1 Sensitivity of the speed schedules to DNI intervals

To prevent the need to use individual speed schedules for each DNI value detected throughout the day (depending on the measurement intervals of the DNI sensor), it is necessary to establish a predetermined range of DNI values for which the same speed schedule can be applied or has only a slight variation. This can be achieved by performing a sensitivity analysis on various DNI intervals. To evaluate this, three DNI intervals have been identified for examination: 100, 50 and 20. Figure 6.1 to 6.3 show the speed schedules for each DNI interval.

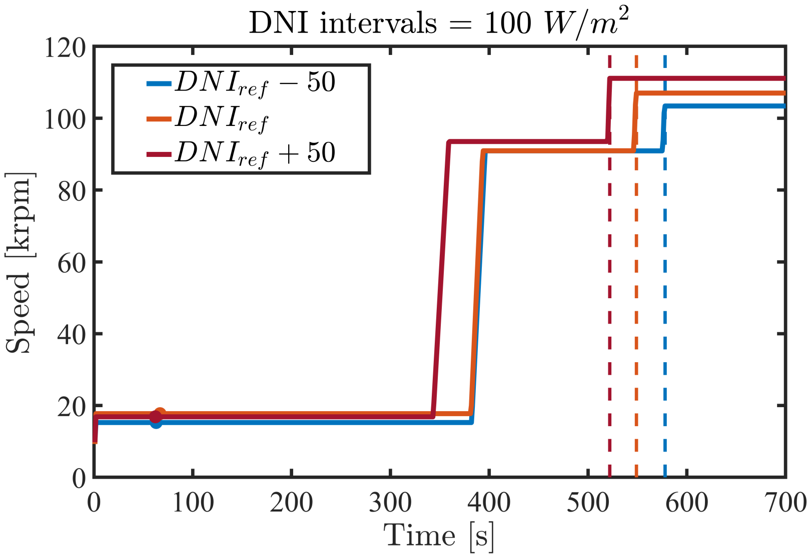

Figure 6.1: Sensitivity of the speed schedule to the DNI intervals for DNI interval of 100 [W/m^2].

As it could be seen in Figure 6.1 to 6.3, the speed schedules of interval 20 ($DNI_{ref} \pm 10$) are more alike compared to the other intervals with the least deviations from the reference speed schedule. The beginning time of generation is also the same for the three schedules associated with this interval. The highest deviation is associated with the highest DNI interval which is 100. For the DNI interval of 50, the main deviations between the schedules are happening at the end of the start-up phase close to the self-sustaining point. As it can be seen in Figure 6.2, the N_2 speed for all three schedules is the same with a maximum relative error of 2%. However, the main deviation is associated with the time when the speed starts increasing to reach the rated

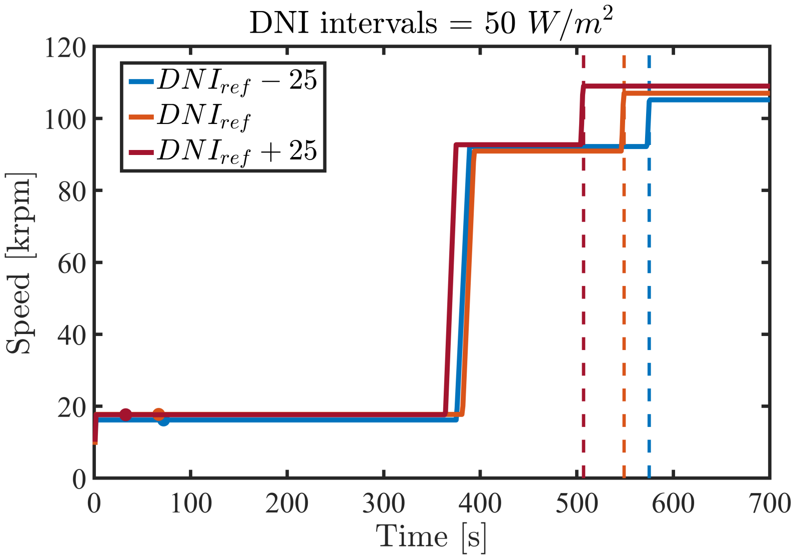

Figure 6.2: Sensitivity of the speed schedule to the DNI intervals for DNI interval of 50 [W/m^2].

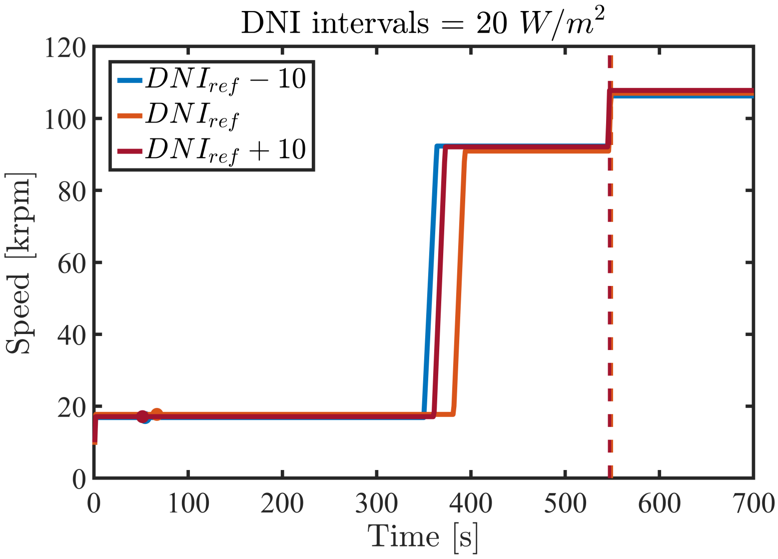

Figure 6.3: Sensitivity of the speed schedule to the DNI intervals for DNI interval of 20 [W/m^2]

speed. It is observed that the time difference is less than 100 seconds. It is important to note that if during this time difference, the DNI undergoes an increase of more than 50 W/m^2, the schedule will change to a different schedule. But in case of a DNI increase of less than 50, it is crucial to verify if the reference schedule is used for the case where the DNI is 25 [W/m^2] more than the reference DNI whose schedule has more time duration to remain constant at N_2 speed, receiver overheating occurs or not. Based on a calculation of the energy conservation, the maximum temperature increase rate of the solar receiver with a 25 $[W/m^2]$ increase in DNI is less than 0.05 °C/s for all of the DNI values which makes this DNI interval acceptable for the analysis. In order to ensure the safety of the system from other aspects as well, the start-up was simulated with the schedule of DNI_{ref} for the two cases where the DNI value was $DNI_{ref}+25$ and $DNI_{ref}-25$. All of the critical components of CSP-MGT operated with respect to their constraints for both cases.

Although the schedules of DNI intervals of 20 $[W/m^2]$ seemed the best choice for the analysis, the DNI interval of 50 was chosen. Since the safety of the system is ensured with this selection and the DNI changes during the day can be very sharp that makes the selection of 50 intervals justified. Because the start-up phase takes a longer time than the DNI changes, the schedules that are used before reaching the self-sustaining point can vary several times. Therefore there was no need for finding extra speed schedules which were required in case of choosing DNI interval of 20. This sensitivity has been also done for all of the DNI values and resulted in the same selection for DNI intervals.

6.2 Sensitivity of the speed schedules to the initial conditions

The second sensitivity analysis is done for the initial condition. In the optimisation procedure of the previous chapter, two main initial conditions were defined: warm start-up with the recuperator metal temperature of 120 °(C) and cold start-up with all materials in ambient temperature. However, there are some cases during the day when the system shuts down due to an insufficient DNI amount and it remains at a specific speed to undergo a cooling process. The system stays at this speed (N_1) which was concluded to be 17 [krpm] for a while until the DNI increases again to a value that is appropriate for generating electricity. In this case, depending on the time duration that the shaft speed has remained constant, the initial temperatures of the system components might have higher values. Therefore, it is crucial to conduct an analysis to determine whether the speed schedule should remain constant or change in response to altered initial conditions. In order to find out this, a sensitivity analysis has been done in terms of the initial conditions of the CSP-MGT system. Since there are four main metal temperatures (four state variables of temperature) in the CSP-MGT transient model that should have initial values for the simulation, there should be a strategy to choose the most important one for conducting the sensitivity analysis. Since TOT is a critical temperature in controlling the operation of the system and it is the temperature which is more likely to be measured without challenge compared with TIT, it was decided to take this temperature for conducting the sensitivity analysis. Furthermore, this temperature is strongly related to the recuperator metal temperature which is due to the fact that the turbine outlet air flows directly to the recuperator. Therefore, among all of the metal temperatures that are defined in the transient model as initial conditions, the initial temperature of the recuperator metal was chosen as the main initial condition for the sensitivity analysis. In order to have a clear understanding of the effect of the initial condition on the speed schedule it was decided to do the sensitivity analysis on three DNI values: 400, 600, and 800 to approximately cover all of the DNI values during the day. Figure 6.4 to 6.6 shows the speed schedules for seven initial conditions related to three selected DNI values. The values written as legends are the recuperator metal temperature in Kelvin.

It can be clearly observed from the three figures that by increasing the initial temperature of the recuperator metal, the amount of Δt_1 where the N_1 speed remains constant, decreases. However, it does not follow a monotonous descending trend by increasing the initial temperature. It is observed that from the temperature of 500 [K] and above, the speed schedule is somehow the same with the maximum relative error of 10 %. Therefore, it was decided to use the average speed schedule for the initial temperatures above 500 [K]. It can be seen from the figures that the focus time in the case of higher initial temperature happens just before the time when the speed begins increasing to N_2. This is due to the fact that the solar receiver and the rest of the metals are already hot and receiving thermal energy at a low speed might cause the

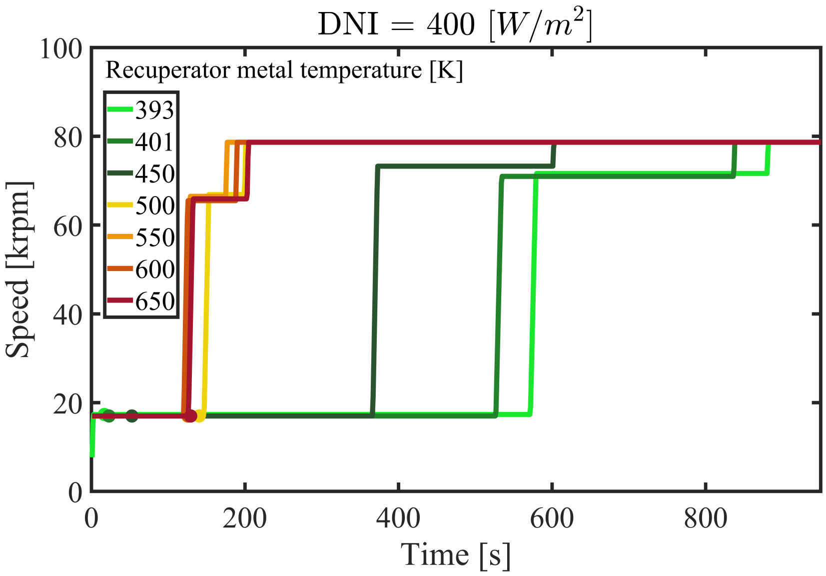

Figure 6.4: Sensitivity of the speed schedule to the initial condition in terms of recuperator metal temperature for DNI = 400 $[W/m^2]$.

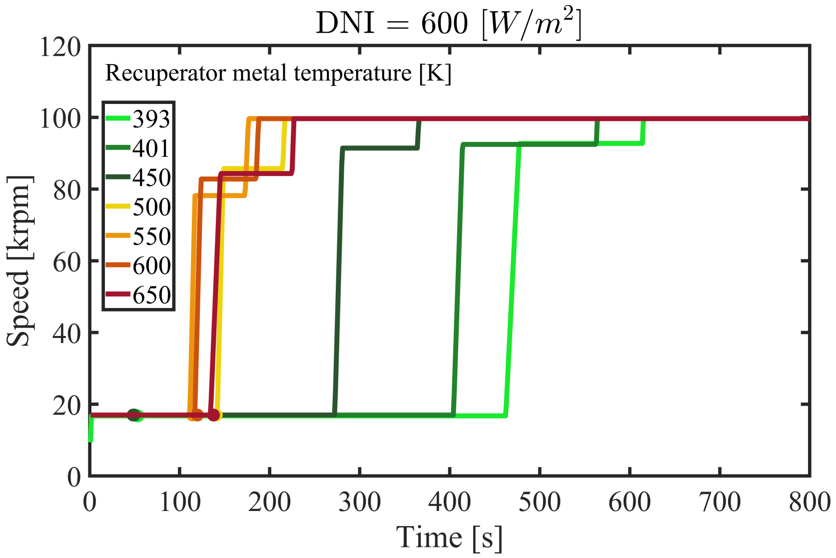

Figure 6.5: Sensitivity of the speed schedule to the initial condition in terms of recuperator metal temperature for DNI = 600 $[W/m^2]$.

critical temperatures to surpass their limits. For the initial conditions of 400 [K] and 450 [K], it is also seen that there is a similar pattern for the three DNI values. The N_2 is the same as the ones for the original speed schedules for warm start-up according to the initial condition of 393 [K]. The Δt_1 for 400 [K] and 450 [K] are 85% and 55% of the one for the initial condition

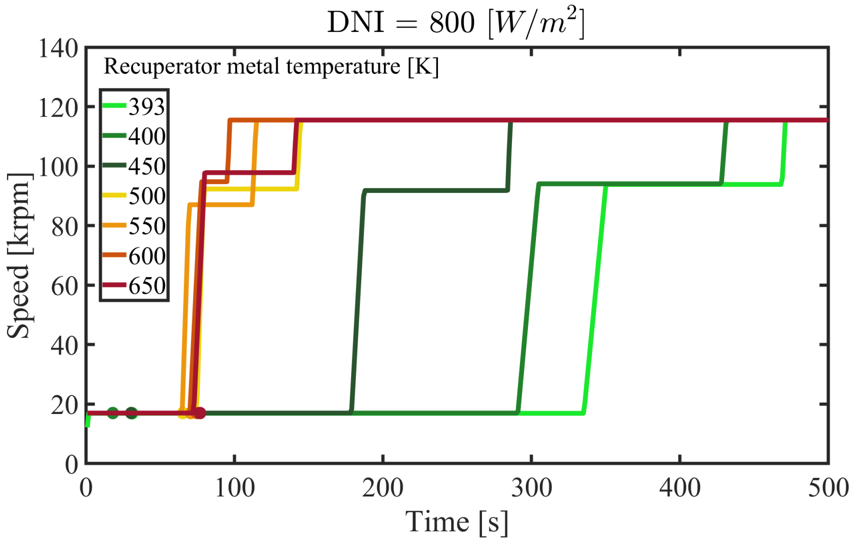

Figure 6.6: Sensitivity of the speed schedule to the initial condition in terms of recuperator metal temperature for DNI = 800 $[W/m^2]$.

of 393. When it comes to the higher values of initial conditions (higher than 500 K), it can be seen that Δt_1 is about 23% of the one for the initial condition of 393 [K]. The results of this sensitivity analysis are used in the next section for the cases where the system shuts down in the middle of the day and the component metals are still hot. This must be noted that this analysis has been done for specific values for the initial condition. Therefore, in case of having any other value of the initial condition different from the analysed ones, they will be interpolated to find out about the resting time period of N_1.

6.3 Categorisation of the DNI variation throughout a year

The DNI variability over a year was obtained from SoDa [26], belonging to Cassacia, Italy, which was the location of the demonstration plant for the OMSoP project. The data for the year 2004 was used in this study, with a resolution of 10 minutes deemed sufficient for the analysis. Although a higher resolution would be preferable for a transient model due to the rapid changes in DNI values, the current resolution is appropriate for the scale of annual evaluations. The primary objective of the analysis is to determine the net energy produced over the course of a year, which is a subtraction of consumed energy from the produced energy. To simulate a transient model for 365 days, the DNI data were categorised into three main groups in terms of the day type: sunny, cloudy and no sun days. A sunny day was defined as a day without any clouds that followed a dome-shaped DNI variation. To identify sunny days within a month, a reference day was chosen belonging to the sunniest day of that month. A sunny day is defined as any day where the maximum DNI difference compared to the reference day is less than 100. The value of 100 was determined through a trial and error process, which led to finding sunny days with similar DNI variations. Days without sun were identified by selecting days where DNI remained below 300 $[W/m^2]$ throughout the whole day. Averaging the data from a set of chosen sunny days produced a single plot that represents them. Subsequently, the simulation of the model was conducted once and the resulting data was scaled by the total number of sunny days. Conversely, the simulation for "no sun" days was conducted only once, and the outcome was scaled by the total number of such days. However, for "cloudy" days, the model had to be simulated for each day as no discernible pattern was observed in the data. Figure 6.7 shows three sample days representative of the three selected categories.

6.4 Evaluation of the CSP-MGT system for a year

After the days throughout the year have been categorised to reduce the number of simulations and after the sensitivity analyses have been done, some extra settings must be added to the model to evaluate the performance of the CSP-MGT system during a year. In the previous chapters, it was shown that the minimum DNI that power generation begins is 260 $[W/m^2]$. Therefore, during the simulation for a day, it was defined that if the DNI during the day decrease to below 260, the system enters a shutdown mode and the speed reduces to a constant speed. The constant value of the speed in this condition is called N_{rest}. The value of this speed has

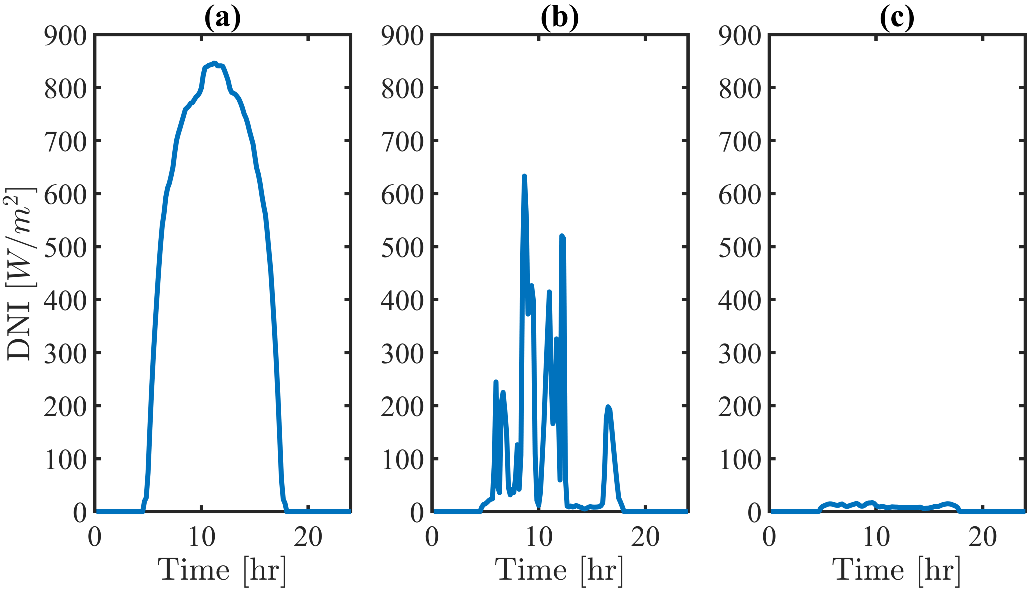

Figure 6.7: Three sample days related to the three categories. a) Sunny day, b) cloudy day, c) no sun day.

been defined in the previous chapter from the optimisation of the speed schedules. On the other hand, when the system is going to start operation, the DNI should be at least 300. In terms of the initial condition, if the recuperator metal temperature is at ambient condition, the system will undergo a cold start-up. In the case of having a temperature of between 120 °C and ambient temperature, the system follows a warm start-up schedule. If the recuperator metal temperature is higher than 120 °C, the start-up procedure will be a hot start-up. It must be noted that during the hot start-up phase, the shaft speed begins from N_{rest} and not the zero speed. In terms of shutdown, no optimisation was done in this study and the speed decreases at a constant rate that was found by doing several simulations to be sure about the safety of the system. During this phase, the shaft speed decreases to the N_{rest} and it remains at this speed until the recuperator metal temperature reduces to less than 120 °C. Then, if the DNI is not high enough for the system to start the operation, the shaft speed is reduced to zero. Apart from the start-up and shutdown phase where the shaft speed is not at the rated speed and it is changing, there are other occasions when the system is operating at the rated speed (off-design speed). Therefore, when the DNI value is measured, if the shaft speed is equal to the rated speed attributed to the measured DNI, then the shaft speed follows a function that the speed is computed based on the DNI value. This function has been computed from the off-design values of each DNI value for having an MPP operation ($N_{rated} = f(DNI)$).

Figure 6.8 shows the flowchart of the programme structure that has been implemented in the developed transient model for analysis throughout the year. This programme structure is for finding the speed schedule as an input for the control system. During the whole year, the earliest time of the day that the DNI can be 300 [W/m^2] is 4:50 A.M. Furthermore, it was seen that during the whole year, the latest time of the day that the DNI is 300 [W/m^2] is 5:50 P.M. Therefore, on all of the days of the year, the speed is increased to N_{rest} at 4:50 A.M and if the DNI is equal or more than 300 [W/m^2] the start-up goes to the next stages. In case the DNI never increases to 300 [W/m^2] during this time period (from 4:50 A.M to 5:40 P.M) that happens for the "no sun" day category, the shaft speed remains at N_{rest} the whole time. If a sunny day occurs, there are only two motoring modes during the day. One is for the early hours of the day when the whole system has been in ambient condition and the start-up is a cold start-up type. The other motoring mode is for the shutdown phase when the system remains at N_{rest} for a while to cool down. If the day is cloudy, there will be several start-ups and shutdowns during the day.

Apart from determining speed schedules, an additional requirement is to develop a schedule for focusing CSP dish during the day. The CSP dish-focusing schedule is not intended for manipulating the thermal input power to control the operation of MGT. Due to the considerable inertia of the dish and the associated high costs and maintenance requirements of the rotation mechanism, CSP dish rotation is restricted to two primary circumstances. The first pertains to initiating the focusing process when DNI levels exceed 300. The second situation is when the DNI is below 260 and the system is undergoing a shutdown phase, necessitating the dish to move out of focus. This means that the CSP dish only moves between the two modes of focus

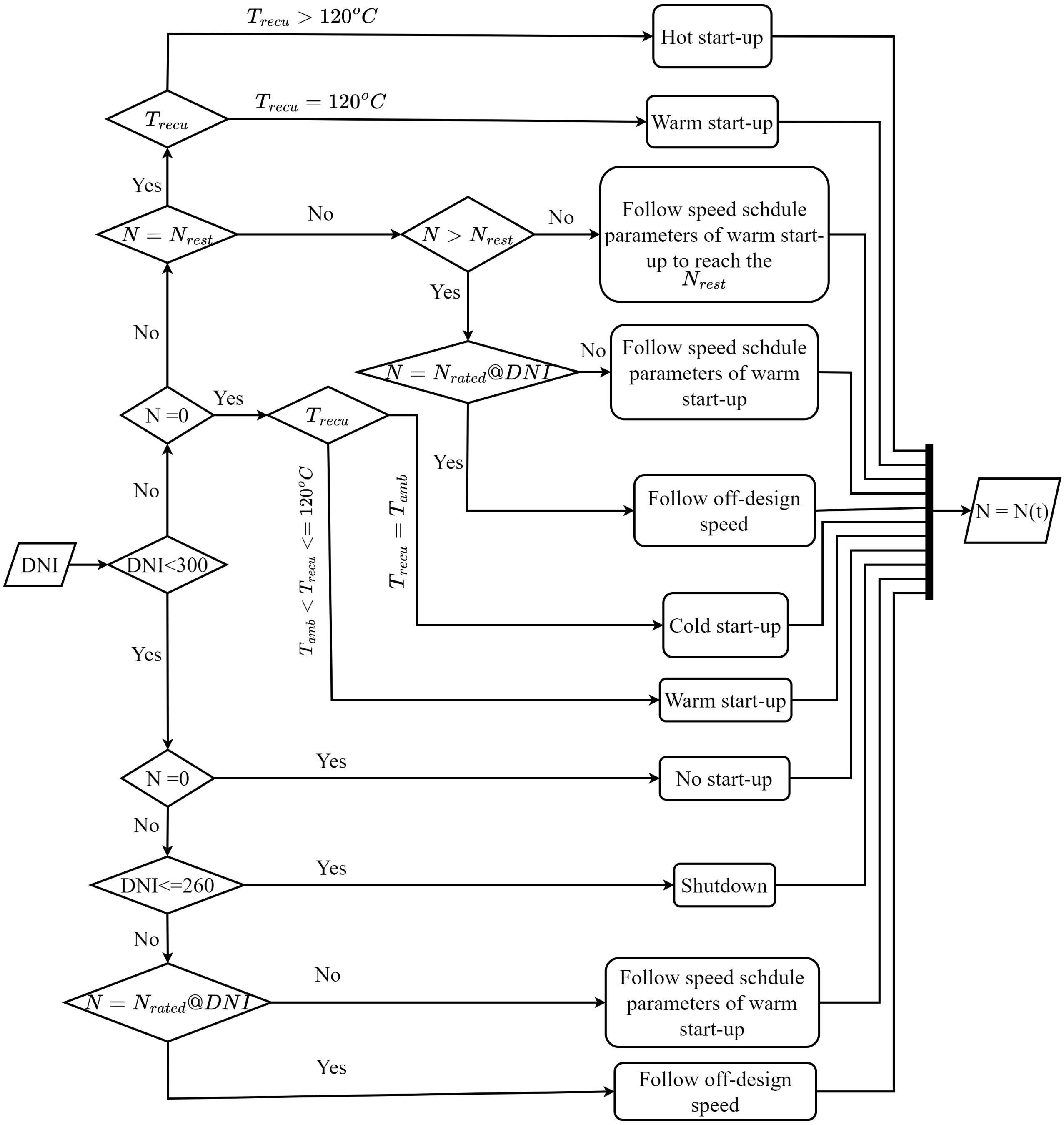

Figure 6.8: Programme structure of simulation programme for computing the speed schedule as an input for the control system.

and out of focus. The programme structure for finding the focus schedule of the CSP dish is shown in Figure 6.9.

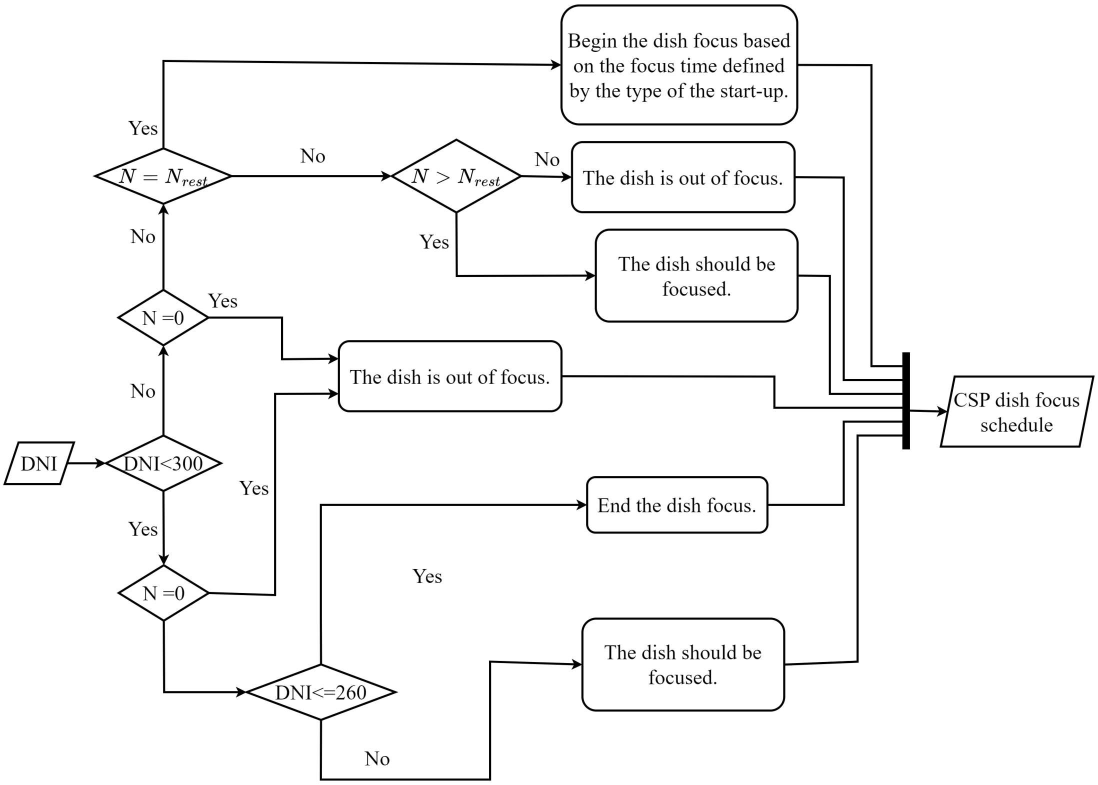

Figure 6.9: Programme structure of simulation programme for computing the CSP dish focus schedule.

The transient model has been simulated for a year by using the programme structures explained earlier. Figure 6.10 shows a DNI distribution at Casacai of Italy [26] as well as the distribution of rated generated power throughout the year. As it is depicted in this figure, the plot of DNI versus time shows that the highest number of hours (more than 2000 hours) belong to the DNI values lower than 260, where no generation can be provided.

By simulating the transient model for the year using the programme structures depicted in Figure 6.8 and 6.9, it was discovered that employing optimised speed schedules results in approximately 3.5% of the total generated energy being utilised for motoring mode, ultimately yielding a net annual energy production of 5.26 MWh. Although the net energy consumption is not considered substantial when compared to the energy generated, it can hold significance for daily analysis, particularly on cloudy days. On certain occasions, energy consumption

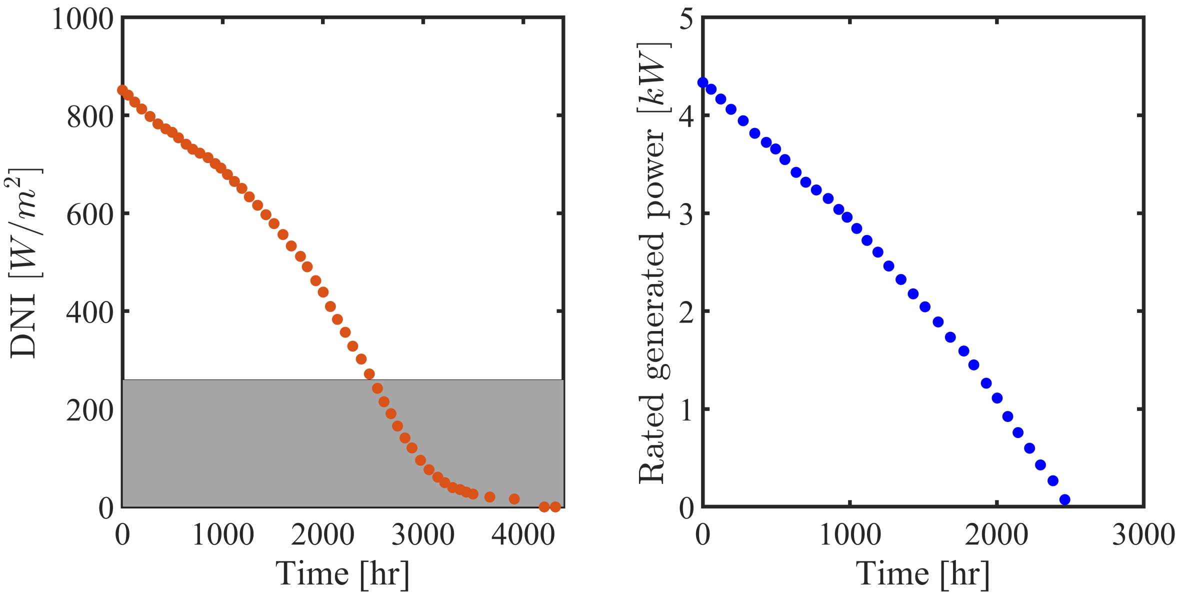

Figure 6.10: DNI duration curve for Casaccia based on average annual insolation data (left) according to the rated generated power (right).

surpasses the produced energy. This is primarily attributed to the unavailability of DNI values at any given moment, as the CSP-MGT operates according to the provided algorithm for the input schedule. In order to have a better insight into how effective the optimal speed schedules are, it is required to compare the results with a benchmark result or measurement. The only existing data for the CSP-MGT start-up belongs to the OMSoP project whose measurements have been used for model validation earlier. Therefore, the start-p schedules used in this experimental setup were used as the benchmark. It is worth mentioning that, the schedules for the start-up of this plant, were generated manually based on the real-time feedback received from the system. Due to the challenges present in the experimental facility, the rotational speed of the shaft could not surpass 80 [krpm] in any of the experimental trials. Therefore, when a particular sample test was chosen, for instances where higher DNI values required greater speeds, the speed schedule was extrapolated.

Firstly, the consumed energy during the start-up was compared for the two cases with OMSoP speed schedule and optimal speed schedules for all DNI values, Figure 6.11. It is evident from the figure that if the optimal speed schedules are used for the start-up, the energy consumption is 30% to 60% less than in the cases where the OMSoP speed schedules are used.

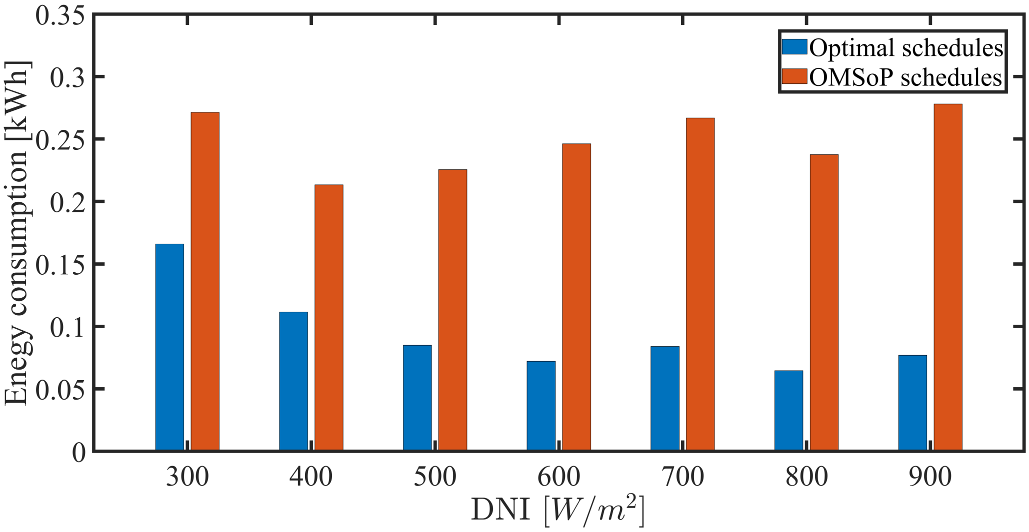

Figure 6.11: Energy consumption during start-up for the two schedules of optimal and OMSoP speed schedules

Afterwards, a simulation was carried out to compare the annual performance of CSP-MGT for the two cases. This simulation was conducted for the month of September, the time when the majority of OMSoP tests were conducted. The findings revealed that when employing OMSoP speed schedules, the energy consumption of CSP-MGT almost doubled compared to the case of using optimal schedules. Due to the longer start-up time associated with the OMSoP schedule, the produced energy was reduced, leading to a roughly 3% decrease in net energy production for the month of September. If this outcome is extrapolated to encompass an entire year, assuming the same energy production as the case with optimal schedules, the consumed energy over a year with the OMSoP schedule amounts to approximately 7% of the total produced energy. Even though the consumed energy constitutes a small fraction of the produced energy, the impact of the optimal schedules is easily discernible.

In CSP-MGTs, initial concerns were raised regarding the energy consumption being excessively high, making these systems impractical for electricity production compared to the generated energy over the course of a year. However, this study demonstrates that the consumed energy during start-ups is not highly significant. This is primarily due to the fact that most start-ups occurring midday are classified as hot start-ups, which do not require substantial energy consumption.

6.5 Conclusion

In this chapter, the main focus was on the transient analysis of the CSP-MGT on an annual basis. This has been done to achieve two main goals which were to design a programme structure to simulate the CSP-MGT and also find out about the annual net produced energy throughout the year. Firstly two sensitivity analyses have been done to investigate the effect of the intervals of DNI values and the effect of initial conditions on the speed schedules. It was found that for annual evaluation, DNI interval of 50 is appropriate which removes the need for having a specific schedule for each measured DNI. In order to see the effect of the initial condition of CSP-MGT on the speed schedule, the recuperator wall temperature was used since it was considered as the most important temperature in the system in terms of ease of measurement. It has been observed that by increasing the recuperator wall's initial temperature, the parameter of Δt_1 in the speed schedule which is the most important parameter in warming up the whole system, is affected the most among all other parameters. For temperatures higher than 500 K, this parameter is about 23% of the one for the warm start-up. For the temperature of 450 and 400, this ratio becomes 55% and 85% respectively. For temperatures higher than 500 K, the CSP dish focusing happens exactly at the time when the shaft speed starts increasing to N_2.

To develop a programme structure for simulating the CSP-MGT transient model over a year, the process involved categorising the days into three groups: sunny days, cloudy days, and days without sun. Subsequently, a programme structure was devised for both the speed schedule and CSP dish focus schedule. These schedules were implemented successfully, ensuring the system remained safe throughout the year-long simulation by using the found optimal schedules. This demonstrates the effectiveness of the programme structure and the optimal schedules. The evaluation conducted for Cassacia, Italy, the location of the OMSoP project, revealed that approximately 3.5% of the energy produced over the year is utilised for the motoring mode, resulting in a net produced energy of 5.26 MWh. To have a better insight, the energy consumption during the start-up resulting from implementing optimal schedules have been compared with the schedules used previously in experimental tests in OMSoP project. It was revealed that around 7% (twice the case of using optimal schedules) of the annual produced energy is allocated to the motoring mode in case of not optimising schedules which shows the effectiveness of the optimal speed schedules.

Chapter 7

Conclusion and recommended future work

7.1 Conclusions

The main aim of this work has been to introduce a characterised start-up schedule for CSP-MGTs. This has been achieved by finding an optimal schedule with a minimum value for the maximum required power, energy consumption and start-up time with consideration of the safe operation of the whole system. The focus of the safety consideration was mainly on the temperature limit of the solar receiver as the critical component and two other limitations attributed to the compressor surge margin and electrical system. In order to achieve this aim, four specific objectives were defined in the introduction chapter which are reproduced here:

- To validate the developed transient model of the CSP-MGT with the available experimental measurements.
- To characterise a schedule for the start-up phase of CSP-MGT.
- To develop a framework to optimise the start-up schedule with targets of minimising the power requirement, energy consumption and start-up time while the safe operation is provided.
- To investigate the transient performance of the CSP-MGT system on an annual basis with a focus on finding the net produced energy.

To reinforce these objectives, a comprehensive literature review was undertaken in Chapter

2 to highlight the required actions and considerations. The outcomes of the thesis are concluded here with respect to the objectives and related comments made in the literature review.

7.1.1 Validation of the CSP-MGT transient model

A successful development of a transient model for a CSP-MGT which is comprised of thermo-mechanical and electrical parts, has been explained in detail. The thermo-mechanical part of the model is based on the lumped volume and one-dimensional discretisation approach which is capable of simulating the transient performance of the system in response to the intermittent nature of the input thermal power. Notably, the low-speed curves of the turbomachinery components model were accurately generated, predicting compressor and turbine air mass flow rates and outlet temperatures with acceptable error. Furthermore, the incorporation of heat soakage within turbomachinery components significantly enhances the analysis of the MGT's start-up phase, resulting in 20-30% improvement in TIT and TOT temperature prediction accuracy. The model's validation through a real-world experimental measurement of the OMSoP project concerning solar receiver overheating demonstrates its potential to ensure the receiver's thermal safety. With its versatility, the developed model enables various analyses related to CSP-MGT start-up operations, facilitating optimal and flexible scheduling. These achievements present a significant advancement in CSP-MGT technology, providing a valuable tool for understanding transient behaviour of the system in terms of thermo-mechanical and electrical parameters and optimising the performance of CSP-MGT systems in the realm of renewable energy research and applications.

7.1.2 Characterising the CSP-MGT start-up schedule

As it was demonstrated in the literature review (Chapter 2) almost all of the studies on the start-up phase were for fuelled gas turbine systems either heavy-duty or low power ratings. In these systems, the input thermal power comes from the fuel mass flow rate as a controllable parameter. However, in CSP-MGTs, since there is no controllable input thermal power, the start-up schedule is different which has not been studied in any research in the literature to the best of the author's knowledge. In this study, the start-up schedule of the CSP-MGT that operates solely with solar energy was characterised for the first time (Chapter 4). Firstly the thermal inertia of the turbomachinery components was reduced by 75% due to having a more realistic value for further study. This was due to adopting a machining process for manufacturing the casings rather than casting for preparing the MGT for the demonstration plant. Secondly, the different types of start-up phases have been classified based on the initial conditions of the system in terms of the metal temperatures. In this regard, a new method for classifying the start-up type specifically for a CSP-MGT system was introduced. Instead of focusing on the duration in which the system has remained shut down, the study suggests using a specific temperature of the system, particularly the mean-wall temperature of the recuperator, as a determining factor for distinguishing between warm and cold start-up types. The reason for this choice is that the CSP-MGT system does not experience shutdowns from the same operating condition each time, unlike heavy-duty fuelled gas turbines.

CSP-MGTs operate differently from fuelled MGTs in terms of control. Instead of using a reference input of fuel mass flow rate, they are controlled based on a reference speed which comes from the controllability feature of the shaft speed in MGTs due to benefiting from power electronics. It has been shown in Chapter 4 that using a schedule for speed reference, rather than a fixed reference speed value, is essential which is confirmed in Chapter 5 as well. This necessity stems from the limitations imposed by the electric current. Current research has shown that utilising a sequential method when formulating the speed schedule, with separate intervals for speed, is more beneficial compared to using a smooth and uninterrupted speed schedule. The reason for favouring this approach is its capacity to provide increased adaptability, especially when accurately identifying the different stages of the start-up procedure. Consequently, the speed schedule comprises individual phases, each marked by a parameter assigned within a defined range. The limits of these parameter ranges are established in Chapter 4 by considering the safety requirements of the entire system. Essential safety factors, such as electric current, electric power, and critical components' temperatures, play a crucial role in setting the boundaries for each parameter.

7.1.3 Optimisation of the start-up phase

The previous experimental study on CSP-MGT system emphasised that the main safety concern in CSP-MGT systems lies in the temperature of the solar receiver wall, as demonstrated in the literature review. Furthermore, minimising start-up costs poses safety challenges, with the temperature of critical components, specifically the solar receiver, being an important factor. The literature review in Chapter 2 further demonstrated the need to identify optimal start-up schedules in similar scenarios with fluctuating loads and multiple system start-ups, striking a balance between safety and cost considerations. Consequently, Chapter 5 focused on optimising the start-up schedule, considering the frequent start-ups experienced by CSP-MGTs due to the fluctuating DNI. The chapter aimed to develop a framework for optimising the CSP-MGT system's start-up schedule and identifying the optimal schedule that minimises energy consumption, maximum required power, and start-up time while ensuring overall system safety. The study revealed a direct correlation between DNI and the maximum power needed for start-ups, with cold start-ups requiring more power than warm start-ups. Thus, optimising cold start-ups aimed to minimise the maximum required power and energy consumption, determining the starter's capacity (in this case, the battery). The optimised capacity was approximately 42% of the DC power generated in the case of nominal power generated by PMSM (6 kW_e), representing the point with the highest value of power on the Pareto front.

Additionally, by employing optimisation techniques, speed schedules were developed with the objective of minimising both energy consumption and start-up time. The analysis revealed a clear connection between lower DNI values and increased energy consumption. For instance, at DNI = 300, the consumption nearly doubles compared to DNI = 900 due to the slower rise in metal temperature. Conversely, higher DNI values lead to shorter start-up times. Warm start-ups at DNI = 300 take approximately four times longer (1600 [s]) to reach power generation compared to DNI = 900 (400 [s]). This demonstrates that 30 minutes are required to achieve power generation at a constant DNI of 300, necessitating at least an equal amount of time to compensate for the energy consumption during start-up. This highlights the significance of managing energy consumption during the start-up phase. The optimisation outcomes demonstrated for different DNI values and both warm and cold start-ups indicated that the solutions on the frontier achieved approximately a 60% decrease in energy consumption and a similar reduction in start-up time compared to the other potential solutions.

The optimised speed schedules for the CSP-MGT system suggest that a minimum of three stages for the speed schedule is required. Although a two-step schedule was an option, the results emphasise the significance of including at least three stages in the speed schedule. At the beginning of the start-up process, regardless of whether it is a cold or warm start-up, the parabolic dish focuses immediately after the shaft speed reaches N_1. For both cold and warm start-ups, the initial constant shaft speed (N_1) was set at 17 krpm, irrespective of the DNI values. The second constant shaft speed (N_2) was determined to be 88% of the rated speed, with a standard deviation error of 8.4% for both types of start-ups. The duration of Δt_1, which represents the period during which N_1 remains constant, accounted for over 60% of the entire start-up duration for both types. However, there was no consistent pattern observed for Δt_2 among the different DNI values, except that it was always shorter than Δt_1 in all cases.

7.1.4 Annual evaluation of the CSP-MGT

To date, the analysis of the CSP-MGT on an annual basis, particularly focusing on transient behaviour, has not been explored in the existing literature. Therefore, the primary objective of chapter 6 was to fill this research gap. The chapter successfully accomplished two main goals: designing a programme structure to simulate the CSP-MGT and determining the annual net produced energy throughout the year.

The investigation included two sensitivity analyses to examine the impact of DNI value intervals and initial conditions on the speed schedules. The results indicated that an appropriate DNI interval of 50 could be used for annual evaluation, eliminating the need for specific schedules corresponding to each measured DNI. Additionally, the initial condition of the CSP-MGT, represented by the recuperator wall temperature, was found to significantly affect the Δt_1 parameter in the speed schedule. Notably, temperatures above 500 K resulted in this parameter accounting for approximately 23% of the warm start-up value. For temperatures of 450 K and 400 K, this ratio increased to 55% and 85%, respectively. Furthermore, it was observed that CSP dish focusing coincided with the shaft speed starting to increase to N_2 for initial temperatures above 500 K.

The development of a programme structure for simulating the CSP-MGT transient model over a year involved categorising the days into three groups based on weather conditions. Subsequently, the successful implementation of the speed schedule and CSP dish focus schedule ensured the system's safety throughout the year-long simulation, employing the optimal schedules derived from the study. These outcomes clearly demonstrate the effectiveness of the programme structure and optimal schedules.

Furthermore, the evaluation conducted for the site of OMSoP project in Cassacia, Italy, revealed that approximately 3.5% of the energy produced over the year was consumed for the motoring mode, resulting in a net produced energy of 5.26 MWh. For a deeper understanding, a comparison has been conducted between the energy consumption during startup when employing optimal schedules and the schedules utilised in prior experimental tests within the OMSoP project. This analysis demonstrated that approximately 7% (which is double the proportion when optimal schedules are utilised) of the yearly generated energy is dedicated to the motoring mode when schedules are not optimised. This outcome underscores the significant impact of employing optimal speed schedules.

7.2 Recommendations for future work

Although the objectives of the current thesis have been successfully delivered, several improvements and recommendations for further work can be made.

7.2.1 Improvements in the system configuration

The focus of this study revolves around CSP-MGTs operating solely on solar energy, with no backup provided. As thoroughly discussed in this thesis, the system encounters challenges due to the significant fluctuations in solar DNI values, leading to multiple start-ups throughout the day. Unfortunately, these frequent start-ups result in low performance, which is far from desirable performance. However, a notable enhancement can be achieved by incorporating thermal energy storage. In this thesis, an extensive mathematical transient model has been developed, which allows for the incorporation of any new component into the energy system. This addition allows for evaluating the transient performance of the system during the start-up with a new configuration. Furthermore, the inclusion of thermal energy storage leads to a reduction in the number of start-ups during the day, consequently altering the start-up schedules for the system which can be further studied.

7.2.2 Improvements in the optimisation framework

In this study, an optimisation framework was developed to find the optimised start-up schedules to be used in the transient model. It has been seen that the speed schedules are found passively and they are fed to the system by getting feedback from DNI value, shaft speed and TOT. This means that based on the requirements of the system operation, the optimal schedules that have been found previously, are used during the operation. However, there can be another improved methodology for operating the system during all of the operating modes which is generating the optimal start-up schedule at the same time the system is operating (actively). This strategy is more advanced and reduces any likelihood of unsafe operation due to finding the optimal schedules based on getting real-time feedback from a larger number of variables. However, for this methodology, it might be required to use more advanced control schemes such as model predictive controller (MPC).

Bibliography

[1] NOAA, “Global climate report for March 2022.” available online: https://www.climate.gov/news-features/understanding-climate/global-climate-report-march-2022. [Accessed 08-Apr-2023].

[2] J. Rogelj, O. Geden, A. Cowie, and A. Reisinger, “Three ways to improve net-zero emissions targets,” *Nature*, vol. 591, no. 7850, pp. 365–368, 2021.

[3] H. Ritchie, M. Roser, and P. Rosado, “Energy,” *Our World in Data*, 2022. https://ourworldindata.org/energy.

[4] S. Küfeoğlu in *Emerging Technologies: Value Creation for Sustainable Development*, pp. 305–330, Springer, 2022.

[5] H. Zsiborács, N. H. Baranyai, A. Vincze, L. Zentkó, Z. Birkner, K. Máté, and G. Pintér, “Intermittent renewable energy sources: The role of energy storage in the european power system of 2040,” *Electronics*, vol. 8, no. 7, p. 729, 2019.

[6] U. Davis, “Solar power.” available online: https://www.ucdavis.edu/climate/definitions/how-is-solar-power-generated. [Accessed Mar-2023].

[7] K. Nwaigwe, P. Mutabilwa, and E. Dintwa, “An overview of solar power (pv systems) integration into electricity grids,” *Materials Science for Energy Technologies*, vol. 2, no. 3, pp. 629–633, 2019.

[8] M. Ghavami, *Cycle analysis and optimisation of micro gas turbines for concentrated solar power*. PhD thesis, City, University of London, 2017.

[9] K. Lovegrove and W. S. Csiro, “Introduction to concentrating solar power (csp) technology,” in *Concentrating Solar Power Technology*, pp. 3–15, Elsevier, 2012.

[10] W. Fuqiang, C. Ziming, T. Jianyu, Y. Yuan, S. Yong, and L. Linhua, "Progress in concentrated solar power technology with parabolic trough collector system: A comprehensive review," *Renewable and Sustainable Energy Reviews*, vol. 79, pp. 1314–1328, 2017.

[11] E. J. Sheu, A. Mitsos, A. A. Eter, E. M. Mokheimer, M. A. Habib, and A. Al-Qutub, "A review of hybrid solar–fossil fuel power generation systems and performance metrics," *Journal of Solar Energy Engineering*, vol. 134, no. 4, p. 041006, 2012.

[12] P. Breeze, "Parabolic trough and fresnel reflector solar power plants," *Solar Power Generation*, pp. 25–34, 2016.

[13] M. I. Roldán Serrano and M. I. Roldán Serrano, *Concentrating solar thermal technologies*. Springer, 2017.

[14] E. Bellos, "Progress in the design and the applications of linear fresnel reflectors–a critical review," *Thermal Science and Engineering Progress*, vol. 10, pp. 112–137, 2019.

[15] S. Colombo, *Experimental selection of optimal chemical looping conditions using iron oxides for applications in CSP systems*. PhD thesis, Politecnico di Torino, 2021.

[16] W. Schiel and T. Keck, "Parabolic dish concentrating solar power (csp) systems," in *Concentrating solar power technology*, pp. 284–322, Elsevier, 2012.

[17] D. P. L. T. R. Magedara, "Market potential analysis of a solar hybrid dish-brayton system," Master's thesis, Universitat Politècnica de Catalunya, 2021.

[18] S. E. T. Office, "Dish/engine system concentrating solar-thermal power basics." available online: https://www.energy.gov/eere/solar/dishengine-system-concentrating-solar-thermal-power-basics. [Accessed Mar-2023].

[19] A. Madhlopa, "Chapter 1 - introduction to concentrating solar power," in *Solar Receivers for Thermal Power Generation* (A. Madhlopa, ed.), pp. 1–45, Academic Press, 2022.

[20] M. Romero and J. González-Aguilar, "Solar thermal csp technology," *Wiley Interdisciplinary Reviews: Energy and Environment*, vol. 3, no. 1, pp. 42–59, 2014.

[21] H. Hachem, R. Gheith, F. Aloui, and S. B. Nasrallah, “Technological challenges and optimization efforts of the stirling machine: A review,” *Energy conversion and management*, vol. 171, pp. 1365–1387, 2018.

[22] P. Pilavachi, “Mini-and micro-gas turbines for combined heat and power,” *Applied thermal engineering*, vol. 22, no. 18, pp. 2003–2014, 2002.

[23] S. Alshahrani and A. Engeda, “Performance analysis of a solar–biogas hybrid micro gas turbine for power generation,” *Journal of Solar Energy Engineering*, vol. 143, no. 2, 2021.

[24] M. Mokhtari, G. Gharehpetian, and S. M. Mousavi Agah, “Chapter 1 - distributed energy resources,” in *Distributed Generation Systems* (G. Gharehpetian and S. M. Mousavi Agah, eds.), pp. 1–19, Butterworth-Heinemann, 2017.

[25] H. N. Somehsaraei, M. M. Majoumerd, P. Breuhaus, and M. Assadi, “Performance analysis of a biogas-fueled micro gas turbine using a validated thermodynamic model,” *Applied Thermal Engineering*, vol. 66, no. 1-2, pp. 181–190, 2014.

[26] SoDa, “Soda: Solar energy services for professionals.[online].” available online: https://www.soda-pro.com/. [Accessed Mar-2023].

[27] J. H. Kim and T. S. Kim, “Development of a program to simulate the dynamic behavior of heavy-duty gas turbines during the entire start-up operation including very early part,” *Journal of Mechanical Science and Technology*, vol. 33, no. 9, pp. 4495–4510, 2019.

[28] J. Kim, T. Song, T. Kim, and S. Ro, “Dynamic simulation of full startup procedure of heavy-duty gas turbines,” *J. Eng. Gas Turbines Power*, vol. 124, no. 3, pp. 510–516, 2002.

[29] OMSoP, “Final report summary-omsop (optimised microturbine solar power system),” tech. rep., FP7-ENERGY, 2013.

[30] J. Spelling, B. Laumert, and T. Fransson, "Optimal gas-turbine design for hybrid solar power plant operation," *Journal of engineering for gas turbines and power*, vol. 134, no. 9, 2012.

[31] H. M. Cameron, L. A. Mueller, and D. Namkoong, "Preliminary design of a solar heat receiver for a brayton cycle space power system," tech. rep., 1972.

[32] R. E. English, "Technology for brayton-cycle space powerplants using solar and nuclear energy," tech. rep., NASA Lewis Research Center, Cleveland, OH (United States), 1986.

[33] C. F. Peruchena, M. Blanco, and A. Bernardos, "Generation of series of high frequency dni years consistent with annual and monthly long-term averages using measured dni data," *Energy Procedia*, vol. 49, pp. 2321–2329, 2014.

[34] L. Aichmayer, J. Spelling, and B. Laumert, "Thermoeconomic analysis of a solar dish micro gas-turbine combined-cycle power plant," *Energy procedia*, vol. 69, pp. 1089–1099, 2015.

[35] SOLGATE, "Solgate: solar hybrid gas turbine electric power system, final publishable report," *Brussels: EU Commission*, 2005.

[36] M. Quero, R. Korzynietz, M. Ebert, A. Jiménez, A. Del Río, and J. Brioso, "Solugas–operation experience of the first solar hybrid gas turbine system at mw scale," *Energy Procedia*, vol. 49, pp. 1820–1830, 2014.

[37] P. Heller, M. Pfänder, T. Denk, F. Tellez, A. Valverde, J. Fernandez, and A. Ring, "Test and evaluation of a solar powered gas turbine system," *Solar energy*, vol. 80, no. 10, pp. 1225–1230, 2006.

[38] J. Sinai, C. Sugarmen, and U. Fisher, "Adaptation and modification of gas turbines for solar energy applications," in *Turbo Expo: Power for Land, Sea, and Air*, vol. 47284, pp. 87–94, 2005.

[39] A. Ring, C. Sugarmen, J. Sinai, R. Buck, P. Schwarzbözl, P. Heller, T. Denk, J. Fer-nandez Reche, and F. Tellez-Sufrategui, “Solar powered gas turbine prototype-technology development and test results,” in *Proc., Power Gen Europe*, 2004.

[40] M. Lanchi, J. Al-Zaili, V. Russo, M. Falchetta, M. Montecchi, and L. Aichmayer, “A quasi-steady state model of a solar parabolic dish micro gas turbine demonstration plant,” *Energies*, vol. 15, no. 3, p. 1059, 2022.

[41] M. B. Hashmi, M. Mansouri, and M. Assadi, “Dynamic performance and control strategies of micro gas turbines: State-of-the-art review, methods, and technologies,” *Energy Conversion and Management: X*, p. 100376, 2023.

[42] S. Bracco and F. Delfino, “A mathematical model for the dynamic simulation of low size cogeneration gas turbines within smart microgrids,” *Energy*, vol. 119, pp. 710–723, 2017.

[43] J. Duan, S. Fan, Q. An, L. Sun, and G. Wang, “A comparison of micro gas turbine operation modes for optimal efficiency based on a nonlinear model,” *Energy*, vol. 134, pp. 400–411, 2017.

[44] W. Wang, R. Cai, and N. Zhang, “General characteristics of single shaft microturbine set at variable speed operation and its optimization,” *Applied thermal engineering*, vol. 24, no. 13, pp. 1851–1863, 2004.

[45] E. Tsoutsanis and N. Meskin, “Dynamic performance simulation and control of gas turbines used for hybrid gas/wind energy applications,” *Applied Thermal Engineering*, vol. 147, pp. 122–142, 2019.

[46] C. Felsmann, U. Gampe, and M. Freimark, “Dynamic behavior of a solar hybrid gas turbine system,” in *Turbo Expo: Power for Land, Sea, and Air*, vol. 56673, p. V003T06A010, American Society of Mechanical Engineers, 2015.

[47] D. Kathirgamanathan and L.-U. Axelsson, “Rotor over-speed analysis of a hybrid solar gas turbine,” in *Turbo Expo: Power for Land, Sea, and Air*, vol. 51043, p. V003T06A012, American Society of Mechanical Engineers, 2018.

[48] A. Traverso, S. Barberis, D. Lima, and A. F. Massardo, “Dynamic analysis of concentrated solar hybridised gas turbine,” in *Turbo Expo: Power for Land, Sea, and Air*, vol. 45653, p. V03AT07A005, American Society of Mechanical Engineers, 2014.

[49] J. Chen, G. Xiao, M. L. Ferrari, T. Yang, M. Ni, and K. Cen, “Dynamic simulation of a solar-hybrid microturbine system with experimental validation of main parts,” *Renewable Energy*, vol. 154, pp. 187–200, 2020.

[50] J. Yang, G. Xiao, M. Ghavami, J. Al-Zaili, T. Yang, A. Sayma, and D. Ni, “Thermodynamic modelling and real-time control strategies of solar micro gas turbine system with thermochemical energy storage,” *Journal of Cleaner Production*, vol. 304, p. 127010, 2021.

[51] M. Amelio, M. S. Pèrez, V. Ferraro, F. Rovense, and S. Bova, “Dynamic simulation of the temperature inlet turbine control system for an unfired micro gas turbine in a concentrating solar tower.,” *Energy Procedia*, vol. 148, pp. 712–719, 2018.

[52] J. Guan, X. Lv, C. Spataru, and Y. Weng, “Experimental and numerical study on self-sustaining performance of a 30-kw micro gas turbine generator system during startup process,” *Energy*, vol. 236, p. 121468, 2021.

[53] B. Ssebabi, F. Dinter, J. van der Spuy, and M. Schatz, “Predicting the performance of a micro gas turbine under solar-hybrid operation,” *Energy*, vol. 177, pp. 121–135, 2019.

[54] J. Zanger, A. Widenhorn, and M. Aigner, “Experimental investigations of pressure losses on the performance of a micro gas turbine system,” in *Turbo Expo: Power for Land, Sea, and Air*, vol. 43987, pp. 437–448, 2010.

[55] J. Seo, H.-S. Lim, J. Park, M. R. Park, and B. S. Choi, “Development and experimental investigation of a 500-w class ultra-micro gas turbine power generator,” *Energy*, vol. 124, pp. 9–18, 2017.

[56] M. Ghavami, J. Alzaili, and A. Sayma, “A comparative study of the control strategies for pure concentrated solar power micro gas turbines,” in *Turbo Expo: Power for Land, Sea, and Air*, vol. 50831, p. V003T06A016, American Society of Mechanical Engineers, 2017.

[57] W. Wang, A. Malmquist, L. Aichmayer, and B. Laumert, “Transient performance of an impinging receiver: an indoor experimental study,” *Energy Conversion and Management*, vol. 158, pp. 193–200, 2018.

[58] D. A. Cantoni, “A parametric study of motor starting for a 2-to 10-kilowatt brayton power system,” tech. rep., 1971.

[59] H. Liu, Z. Chi, and S. Zang, “Transient behaviour and optimal start-up procedure of closed brayton cycle with high thermal inertia,” *Applied Thermal Engineering*, vol. 199, p. 117587, 2021.

[60] A. Nannarone and S. A. Klein, “Start-up optimization of a ccgt power station using model-based gas turbine control,” *Journal of Engineering for Gas Turbines and Power*, vol. 141, no. 4, p. 041018, 2019.

[61] S. Jafari, S. A. Miran Fashandi, and T. Nikolaidis, “Modeling and control of the starter motor and start-up phase for gas turbines,” *Electronics*, vol. 8, no. 3, p. 363, 2019.

[62] F. Alobaid, R. Starkloff, S. Pfeiffer, K. Karner, B. Epple, and H.-G. Kim, “A comparative study of different dynamic process simulation codes for combined cycle power plants–part b: start-up procedure,” *Fuel*, vol. 153, pp. 707–716, 2015.

[63] I. Rossi, A. Sorce, and A. Traverso, “Gas turbine combined cycle start-up and stress evaluation: A simplified dynamic approach,” *Applied Energy*, vol. 190, pp. 880–890, 2017.

[64] F. Alobaid, N. Mertens, R. Starkloff, T. Lanz, C. Heinze, and B. Epple, “Progress in dynamic simulation of thermal power plants,” *Progress in energy and combustion science*, vol. 59, pp. 79–162, 2017.

[65] A. Fawke and H. I. Saravanamuttoo, “Digital computer methods for prediction of gas turbine dynamic response,” *SAE Transactions*, pp. 1805–1813, 1971.

[66] J. F. Sellers and C. J. Daniele, *DYNGEN: A program for calculating steady-state and transient performance of turbojet and turbofan engines*, vol. 7901. National Aeronautics and Space Administration, 1975.

[67] J. Kim, T. Kim, and S. Ro, “Analysis of the dynamic behaviour of regenerative gas turbines,” *Proceedings of the Institution of Mechanical Engineers, Part A: Journal of Power and Energy*, vol. 215, no. 3, pp. 339–346, 2001.

[68] A. Traverso, “Transeo code for the dynamic performance simulation of micro gas turbine cycles,” in *Turbo Expo: Power for Land, Sea, and Air*, vol. 47284, pp. 45–54, 2005.

[69] C. R. Davison and A. Birk, “Steady state and transient modeling of a micro-turbine with comparison to operating engine,” in *Turbo Expo: Power for Land, Sea, and Air*, vol. 41715, pp. 27–35, 2004.

[70] C. R. Davison and A. Birk, “Comparison of transient modeling techniques for a micro turbine engine,” in *Turbo Expo: Power for Land, Sea, and Air*, vol. 42401, pp. 449–458, 2006.

[71] M. B. Hashmi, T. A. Lemma, S. Ahsan, and S. Rahman, “Transient behavior in variable geometry industrial gas turbines: a comprehensive overview of pertinent modeling techniques,” *Entropy*, vol. 23, no. 2, p. 250, 2021.

[72] S. Camporeale, B. Fortunato, and M. Mastrovito, “A modular code for real time dynamic simulation of gas turbines in simulink,” 2006.

[73] P. Lin, X. Du, Y. Shi, and X.-M. Sun, “Modeling and controller design of a micro gas turbine for power generation,” *ISA transactions*, 2020.

[74] A. Traverso, *TRANSEO: a new simulation tool for transient analysis of innovative energy systems: ph. d. thesis*. PhD thesis, 2004.

[75] P. P. Walsh and P. Fletcher, *Gas turbine performance*. John Wiley & Sons, 2004.

[76] J. Howard, "Sub-idle modelling of gas turbines: Altitude relight and windmilling," 2007.

[77] P. K. Zachos, I. Aslanidou, V. Pachidis, and R. Singh, "A sub-idle compressor characteristic generation method with enhanced physical background," *Journal of engineering for gas turbines and power*, vol. 133, no. 8, 2011.

[78] C. Janke, D. Bestle, and B. Becker, "Compressor map computation based on 3d cfd analysis," *CEAS Aeronautical Journal*, vol. 6, no. 4, pp. 515–527, 2015.

[79] E. Tsoutsanis, N. Meskin, M. Benammar, and K. Khorasani, "A component map tuning method for performance prediction and diagnostics of gas turbine compressors," *Applied Energy*, vol. 135, pp. 572–585, 2014.

[80] J. H. Kim and T. S. Kim, "A new approach to generate turbine map data in the sub-idle operation regime of gas turbines," *Energy*, vol. 173, pp. 772–784, 2019.

[81] E. Andersson, "Development of a dynamic model for start-up optimization of coal-red power plants," 2013.

[82] D. Faille and F. Davelaar, "Model based start-up optimization of a combined cycle power plant," *IFAC Proceedings Volumes*, vol. 42, no. 9, pp. 197–202, 2009.

[83] A. Tica, *Design, optimization and validation of start-up sequences of energy production systems*. PhD thesis, Supélec, 2012.

[84] F. Alobaid, R. Postler, J. Ströhle, B. Epple, and H.-G. Kim, "Modeling and investigation start-up procedures of a combined cycle power plant," *Applied energy*, vol. 85, no. 12, pp. 1173–1189, 2008.

[85] F. Tetsuya, "An optimum start up algorithm for combined cycle," *Transactions of the Japan Society of Mechanical Engineers*, vol. 67, no. 660, pp. 2129–2134, 2001.

[86] G. Nowak, A. Rusin, H. Łukowicz, and M. Tomala, "Improving the power unit operation flexibility by the turbine start-up optimization," *Energy*, vol. 198, p. 117303, 2020.

[87] Y. Yoshida, T. Yoshida, Y. Enomoto, N. Osaki, Y. Nagahama, and Y. Tsuge, "Start-up optimization of combined cycle power plants: A field test in a commercial power plant," *Journal of Engineering for Gas Turbines and Power*, vol. 141, no. 3, 2019.

[88] J. Kim, T. Song, T. Kim, and S. Ro, "Model development and simulation of transient behavior of heavy duty gas turbines," *J. Eng. Gas Turbines Power*, vol. 123, no. 3, pp. 589–594, 2001.

[89] M. Khader, *Development of a micro gas turbine for concentrated solar power applications*. PhD thesis, City, University of London, 2017.

[90] B. J. McBride, *Coefficients for calculating thermodynamic and transport properties of individual species*, vol. 4513. National Aeronautics and Space Administration, Office of Management Scientific and Technical Information Program, 1993.

[91] F. P. Incropera, D. P. DeWitt, T. L. Bergman, A. S. Lavine, *et al.*, *Fundamentals of heat and mass transfer*, vol. 6. Wiley New York, 1996.

[92] D. Laria, *Techno-economic assessment of a solar dish micro gas turbne system*. PhD thesis, City, University of London, 2020.

[93] C. F. McDonald, "Recuperator considerations for future higher efficiency microturbines," *Applied Thermal Engineering*, vol. 23, no. 12, pp. 1463–1487, 2003.

[94] H. Lee, *Thermal design: heat sinks, thermoelectrics, heat pipes, compact heat exchangers, and solar cells*. John Wiley & Sons, 2022.

[95] R. M. Manglik and A. E. Bergles, "Heat transfer and pressure drop correlations for the rectangular offset strip fin compact heat exchanger," *Experimental Thermal and Fluid Science*, vol. 10, no. 2, pp. 171–180, 1995.

[96] W. Wang, H. Xu, B. Laumert, and T. Strand, “An inverse design method for a cavity receiver used in solar dish brayton system,” *Solar energy*, vol. 110, pp. 745–755, 2014.

[97] H. Strumpf, D. Kotchick, and M. Coombs, “High-temperature ceramic heat exchanger element for a solar thermal receiver,” 1982.

[98] W. Wang, B. Wang, L. Li, B. Laumert, and T. Strand, “The effect of the cooling nozzle arrangement to the thermal performance of a solar impinging receiver,” *Solar Energy*, vol. 131, pp. 222–234, 2016.

[99] W. Wang, B. Laumert, H. Xu, and T. Strand, “Conjugate heat transfer analysis of an impinging receiver design for a dish-brayton system,” *Solar Energy*, vol. 119, pp. 298–309, 2015.

[100] S.-Y. Wu, F.-H. Guo, and L. Xiao, “Numerical investigation on combined natural convection and radiation heat losses in one side open cylindrical cavity with constant heat flux,” *International Journal of Heat and Mass Transfer*, vol. 71, pp. 573–584, 2014.

[101] H. M. Hofmann, M. Kind, and H. Martin, “Measurements on steady state heat transfer and flow structure and new correlations for heat and mass transfer in submerged impinging jets,” *International Journal of Heat and Mass Transfer*, vol. 50, no. 19-20, pp. 3957–3965, 2007.

[102] L. Zsolt Pap, “Model predictive control of electric drives-design, simulation and implementation of pmsm torque control,” 2018.

[103] C. Huynh, L. Zheng, and D. Acharya, “Losses in high speed permanent magnet machines used in microturbine applications,” 2009.

[104] J. Guo, *Modeling and design of inverters using novel power loss calculation and dc-link current/voltage ripple estimation methods and bus bar analysis*. PhD thesis, 2017.

[105] G. Dušan and P. Marco, “Igbt power losses calculation using the data-sheet parameters,” tech. rep., infineon, 2009.

[106] ST, “Igbt datasheet - production data of stgw20h60df, stgwt20h60df,” tech. rep., 2013.

[107] M. H. Bierhoff and F. W. Fuchs, “Semiconductor losses in voltage source and current source igbt converters based on analytical derivation,” in *2004 IEEE 35th Annual Power Electronics Specialists Conference (IEEE Cat. No. 04CH37551)*, vol. 4, pp. 2836–2842, IEEE, 2004.

[108] M. Hohloch, J. Zanger, A. Widenhorn, and M. Aigner, “Experimental characterization of a micro gas turbine test rig,” in *Turbo Expo: Power for Land, Sea, and Air*, vol. 43987, pp. 671–681, 2010.

[109] W. M. Kays and A. L. London, “Compact heat exchangers,” 1984.

[110] D. Iaria, H. Nipkey, J. Al Zaili, A. I. Sayma, and M. Assadi, “Development and validation of a thermo-economic model for design optimisation and off-design performance evaluation of a pure solar microturbine,” *Energies*, vol. 11, no. 11, p. 3199, 2018.

[111] e+a, “Motor datasheet- motor type mspw 5.4/4-2-d1,” tech. rep., 2015.

[112] W. De Paepe, S. Abraham, P. Tsirikoglou, F. Contino, A. Parente, and G. Ghorbaniasl, “Operational optimization of a typical micro gas turbine,” *Energy Procedia*, vol. 142, pp. 1653–1660, 2017.

[113] N. Cumpsty, *Compressor Aerodynamics*. No. v. 10 in Compressor aerodynamics, Krieger Pub., 2004.

[114] G. B. Leyland, “Multi-objective optimisation applied to industrial energy problems,” tech. rep., EPFL, 2002.

[115] I. Bertini, M. D. Felice, F. Moretti, and S. Pizzuti, “Start-up optimisation of a combined cycle power plant with multiobjective evolutionary algorithms,” in *European Conference on the Applications of Evolutionary Computation*, pp. 151–160, Springer, 2010.

Appendices

Appendix A

The methodology for the generation of low-speed curves of compressor and turbine

Generally, the compressor performance maps which are publicly available do not include the data for low rotational speeds. Usually, the available data are for speeds above approximately 50% of the design speed. In order to generate the speed curves at very low rotational speeds of the compressor that are required for the start-up phase, a zero-speed curve was introduced to the performance map. Then the performance curves for the low-speed region of the compressor map were interpolated between the zero-speed curve and the lowest provided one. The interpolation was done by using polynomial β-lines which are defined in Smooth C software. Figure A.1 shows the generated zero-speed curve shown in red color. By using this curve and β lines, the rest of the speed curves are also generated. The final compressor performance map is shown in Figure A.2.

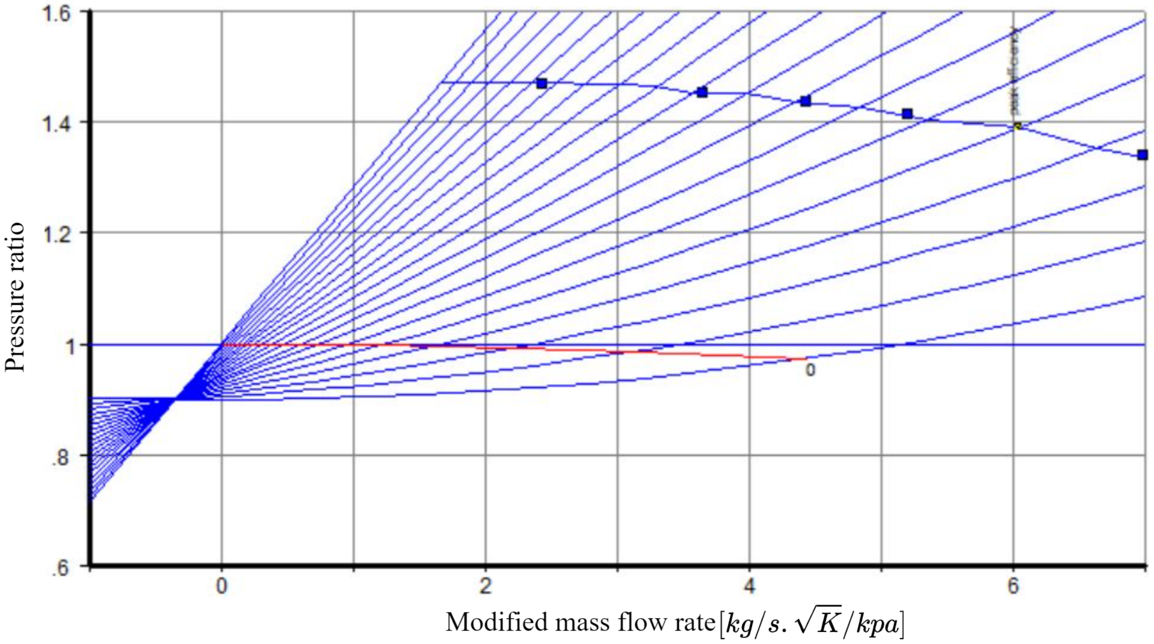

Figure A.1: zero-speed curve on the compressor performance map for generating low-speed curves.

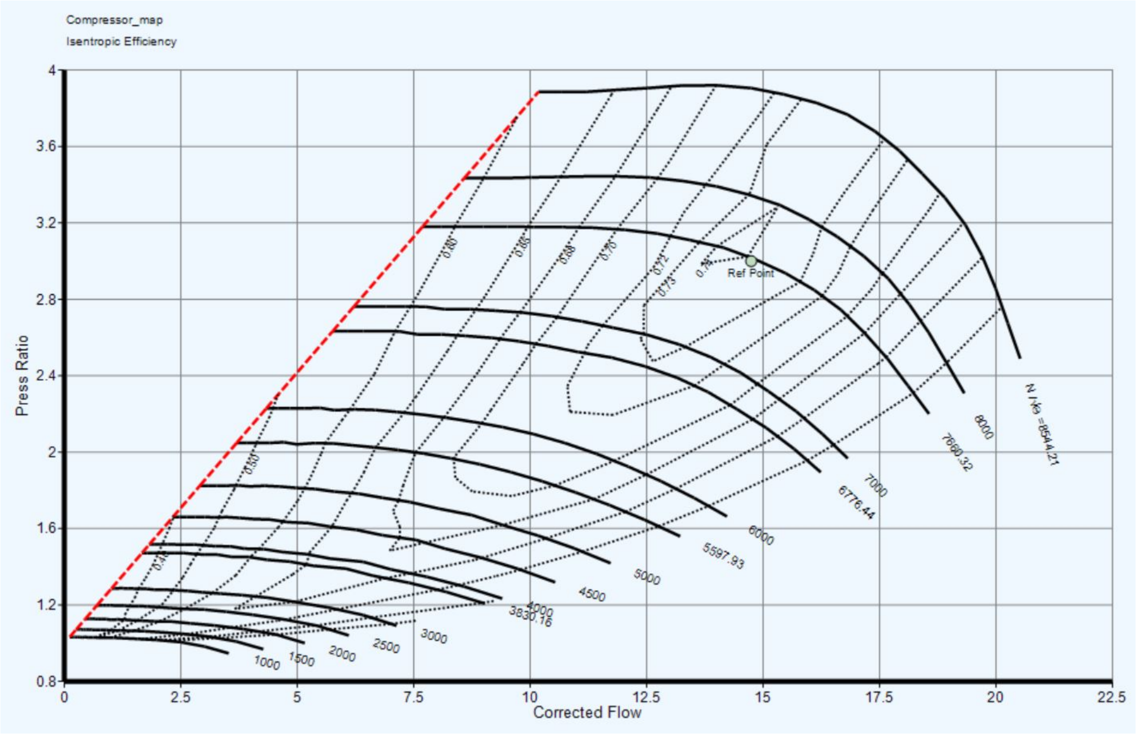

Figure A.2: The generated compressor performance map for low-speed curves in Smooth C software.

Appendix B

The interpolation methodology of the compressor and turbine map

To find the according point for a specific pressure ratio and modified speed, an interpolation of the operating points on turbomachinery components' maps is required. This is due to the reason that number of speed curves of the turbomachinery components is not many and if an operating point has a modified speed different than the existing curves, the related parameters should be interpolated. The interpolation in this thesis follows a linear methodology. There are two main steps for the interpolation which are explained here. In the first step, the aimed speed curve is interpolated by using the operating points on the lower and upper existing speed curves of (N_{i-1} and N_{i+1}), Figure B.1. B.1.

In the second step, the modified mass flow rate of the operating point with the known pressure ratio is found by interpolating between the two points on the speed curve with knowing π_j and with the help of two surrounding points(π_{j-1} and π_{j+1}), Figure B.2.

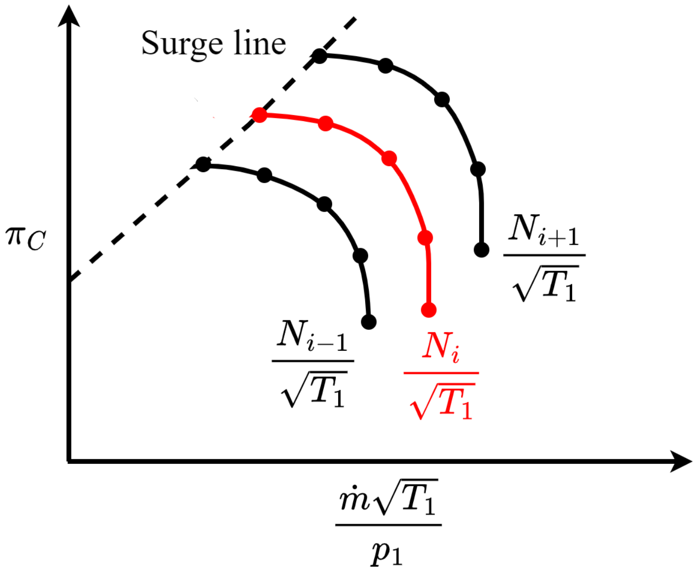

Figure B.1: Interpolation of compressor characteristic curve for finding the aimed speed curve.

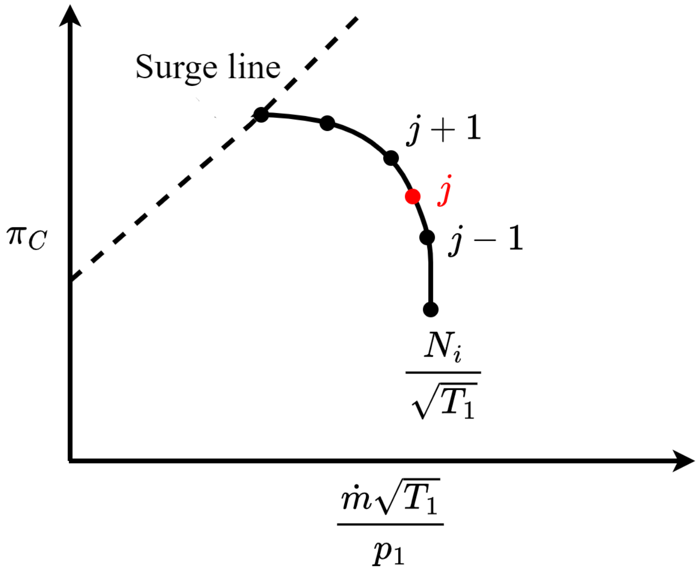

Figure B.2: Interpolation of compressor characteristic curve for finding the aimed modified mass flow rate.

Appendix C

Electrical model specifications

C.1 PMSM/PMSG

The PMSM that was used in this study has a nominal power of 6 kW_e. The datasheet of this motor was provided by City, University of London. The one-phase equivalent circuit diagram of the three-phase PMSM is shown in Figure C.1 and the main specifications that were required for the calculations of this study are shown in Table C.1 accordingly.

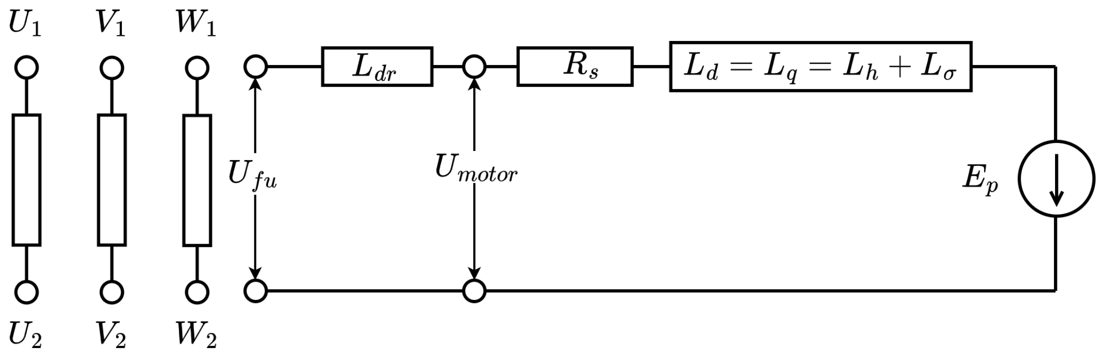

Figure C.1: Equivalent diagram of one phase of the PMSM.

As depicted in the diagram, the circuit presented is designed for a single phase, but it has the potential for expansion to accommodate the two remaining phases. The voltage denoted as U_{motor} refers to the phase voltage, applicable to one of the phases. However, when the motor operates in three phases, the primary voltage used for calculations is the phase-to-phase voltage, commonly known as the line voltage. The correlation between phase and line voltage is shown below.

Characteristic	Symbol	Value
Rated power [kW_e]	P_N	6
Motor voltage [V]	U_{motor}	170
Rated current [A]	I_N	13
Inverter output voltage [V]	U_{fu}	170
Phase stator resistance [Ω]	R_s	0.159
Magnet wheel voltage [V]	E_p	157
Maximum inverter output voltage [V]	$U_{fu,max}$	360
Motor main field inductance [mH]	L_h	0.243
Motor rated speed [rpm]	N_N	130000
Motor rated frequency [Hz]	f_N	2167
Motor rated phase-phase voltage [V]	V	295

Table C.1: Motor data [111]

$$V_{Ph} = \frac{V_L}{\sqrt{3}} \tag{C.1}$$

represent phase and line voltage, respectively. In the motor being investigated, the specified voltage is 295 [V], which corresponds to the line voltage and can be determined from U_{motor}. During the motoring mode, this is the voltage that the inverter or IGBT converter needs to supply, with a maximum capability of 360 [V]. The PMSM voltage without losses is called magnet wheel voltage (E_p) and it is calculated in the following manner.

$$E_p = U_{motor} - I.\sqrt{R_s^2 + (L\omega_e)^2} \tag{C.2}$$

where I, R_s, L and *omega* are electric current, phase stator resistance, field inductance and electromagnetic speed of the motor.

Appendix D

IGBT converter

The IGBT converter which is a bi-directional converter, is used in both motoring and generation mode. Based on the common topologies that are used for three-phase currents, six IGBTs are used, Figure D.1.

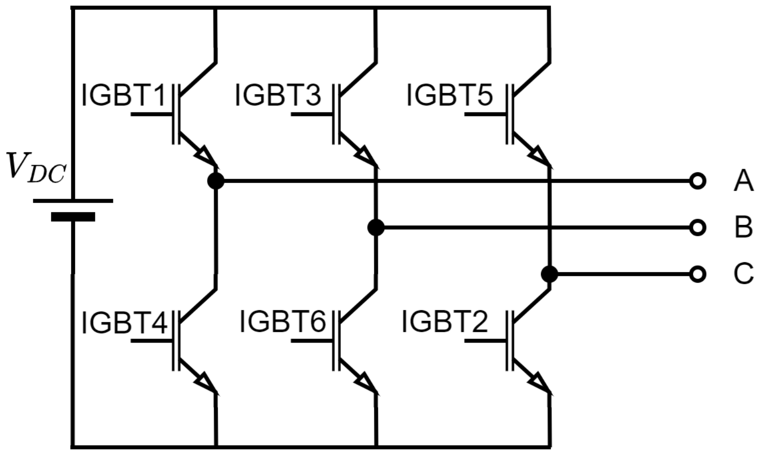

Figure D.1: Three-phase IGBT converter with DC source (motoring mode).

The specifications that were used for this study have been chosen from an IGBT with similar operating conditions. The chosen IGBT is for high-speed operations with a maximum voltage and current of 600 [V] and 20 [A]. The characteristic curve of this component is shown in D.2. The resistance of the IGBT during on-state conditions where the current is not zero is calculated by the below equation based on the information extracted from Figure D.2.

$$R_I = \frac{\Delta V_{CE}}{\Delta I_{CE}} \tag{D.1}$$

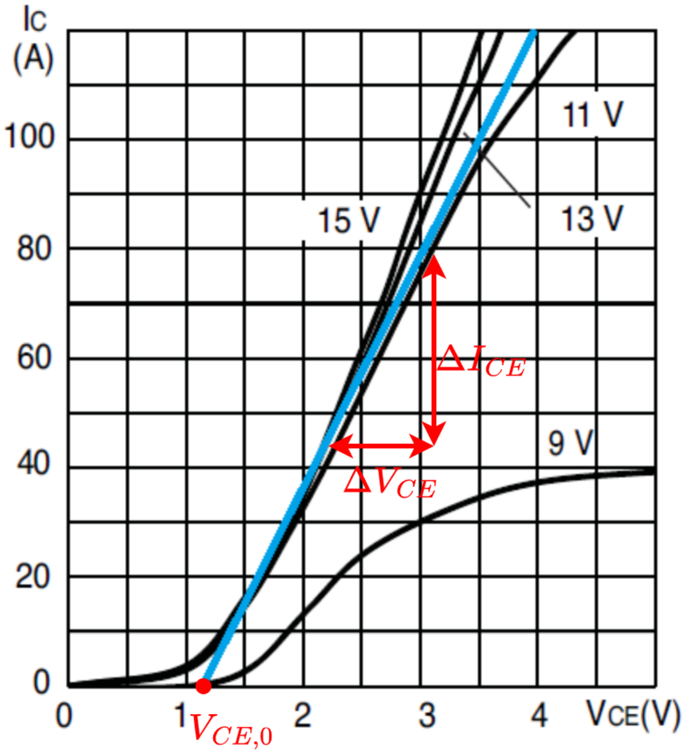

Figure D.2: Characteristic curve of the IGBT and demonstration of on-state resistance and off-state voltage [105].

The two specifications that have been found from the characteristic curve are used in calculating conduction power loss explained in Chapter 3. Additionally, the information for calculating the switching losses of the IGBT is shown in Table D.1. The information provided in the table for energy consumption during switching on and off are provided for the IGBT in test conditions (reference conditions).

Symbol	Parameter	Test conditions	Value
E_{on} $[\mu J]$	Turn-on switching losses	V_{CE} = 400 [V]	209
E_{off} $[\mu J]$	Turn-off switching losses	I_C = 20 [A]	261

Table D.1: Switching energy loss in one IGBT [106].